# TIMING OF EVENTS, RESET MECHANISM, AND ALLOSTERY INNATE TO THE GTP HYDROLYSIS CYCLE OF ATLASTIN

A Dissertation

Presented to the Faculty of the Graduate School

of Cornell University

in Partial Fulfillment of the Requirements for the Degree of

Doctor of Philosophy

by

John Paul O'Donnell

December 2017

# TIMING OF EVENTS, RESET MECHANISM, AND ALLOSTERY INNATE TO THE GTP HYDROLYSIS CYCLE OF ATLASTIN

John Paul O'Donnell, Ph. D.

Cornell University 2017

Homotypic membrane fusion of the smooth endoplasmic reticulum (ER) is catalyzed by atlastin (ATL), a member of the dynamin superfamily. Maintaining proper membrane architecture and dynamics in this highly compartmentalized organelle is accomplished in part through ATL-mediated fusion of ER tubules to form a highly interconnected reticular system of three-way junctions. Mechanistically, ATL couples the energy from GTP hydrolysis to a series of conformational changes and homodimerization events that result in membrane fusion. Higher eukaryotes express three ATL isoforms. Two of these isoforms, human ATL1 and ATL3 have been implicated in neurological disorders, namely Hereditary Spastic Paraplegia (HSP) and Hereditary Sensory Neuropathy (HSN) where axon function is impaired. Disease causing mutations in *atl1* and *atl3* are dominant-negative and cause the exchange of reticular ER for long unbranched membrane tubules. The underlying mechanistic differences between human isoforms and disease-associated mutations are poorly understood.

Here we identify and give order to discrete temporal steps in the catalytic cycle for ATL1 and ATL3. A comparative study demonstrates that isoforms sample the same series of events but do so at different timescales. We also establish a conserved mechanism for the displacement of the catalytic magnesium ion post GTP hydrolysis. Investigation into mechanisms

of disease pathogenesis yields structural and functional defects of an atypical HSP variant. This HSP mutant, ATL1-$F^{151}S$, is impaired in its GTP hydrolysis cycle but is capable of sampling the high affinity homodimer when bound to a transition state analog. These findings along with additional structural information from mutant proteins define a mechanism for allosteric coupling where $F^{151}$ is the central residue in a hydrophobic interaction network connecting the active-site to an inter-domain interface responsible for nucleotide loading.

## BIOGRAPHICAL SKETCH

John O'Donnell was born on the meteorological holiday of Groundhogs Day in 1988 and spent his childhood living in rural Pennsylvania with a loving family. The author was recognized as a McKelvey Scholar in late high school which enabled him to attend Juniata College where he was awarded a Bachelor of Science in molecular biology and art history. He matriculated *magna cum laude* with honors. During his time at Juniata College, John worked in the laboratory of Dr. Jill B. Keeney and established that the integration frequency of the yeast retrotransposon, Ty1, depends on the synthesis and availability of deoxyribonucleotides. This work was the subject of his undergraduate thesis, his first publication, and the beginning of his lifelong interest in scientific inquiry. Wanting to learn more about how enzyme mechanisms govern biology, John enrolled in a PhD program at Cornell University where he met his future mentor Dr. Holger Sondermann. In 2011, John graciously accepted a position in Dr. Holger Sondermann's research group where he has been pursuing his doctoral dissertation since. During these formative years, John elucidated the mechanistic framework for atlastin mediated membrane fusion. Outside of the laboratory, John acts as though he is an aspiring chef, enjoys obscure music, travels, perpetually hosts his closest friends, and adores the company of his loving wife.

For L. John O’Donnell

“I did not start with a written credo or manifesto. Nor was there a program to be followed. It all came about very slowly.

School days exposed me to the hows more than to the whys or the whats. Encounters with the work of others were stimulants to broader vistas. Childhood memories, mostly happy ones, persisted. Natures as an influence, always strong. Companionship, love and family, a measure of fulfillment. Social contact and hours of solitude, all ingredients in the process of one's growth.

Enthusiastic beginnings and recognition of failures marking a long quest to seek and sometimes find a form, a structure, a sound or a way. A find that would tend to make me feel what I am or one that would cause a change in me, would simply deepen the mystery. Facing a problem, yes. Solving it, more often than not, would prove evanescent.

The acceptance of the reality of the dream as a stimulant and propellant toward achieving the other reality generated an atmosphere of involvement rather than passivity. Immersion into the vast recesses of the mind leading to the realization that this inner world is as immense as the cosmos outside ...

At this eternal moment, I have a gut feeling that awareness of the miracle of life is the purpose of life. I might never know ...“

-Harry Bertoia

## ACKNOWLEDGEMENTS

I wish that I could fully articulate my gratitude for Holger Sondermann in words. Holger's intelligence, scientific intuition, and drive are all attributes that define him as a scientist and I am luckily to have trained with such a steadfast mentor during graduate career. He has given me freedom to explore my own scientific interests and assisted me in taking ownership of the projects that we have developed through the years. Beyond science as a common denominator, I am especially grateful for my friendship with Holger. He has proved to be one of the most compassionate and encouraging friends that I've made during graduate school and I am forever thankful.

I would like to show appreciation to all of the members of the Sondermann laboratory that I have interacted with over the years. Especially, I would like to thank Shih Lin "Lynda" Goh and Laura Byrnes for training me early in my graduate career and with Krista Giglio, provided a wonderful work environment. In the later years, I was lucky to overlap with Richard B. Cooley while he was a post-doc in the lab. Rick was a very influential mentor and a great friend. His intelligence and attention to detail were bar none and I thank him for technical expertise, endless scientific conversations over beers, and most of all, his support. I have to thank the new generation of lab members, Carolyn Kelly and Justin Lormand for filling the shoes of past members in respect to their intelligence and spirit seamlessly; I've had a wonderful time working with you both and I wish you the best in your future careers (and restraining Holger in my absence!).

Another mentor that I am deeply grateful for is Carolyn Sevier. Despite me being a 'rotation turncoat', Carolyn has shown unconditional support toward me and my

development as a scientist. I've always enjoyed our in depth conversations about projects pertaining to both work in Holger's lab and a story we've built from data collected during my rotation in her lab. With a manuscript currently being prepared, I am excited that my PhD has been bookended with work out of Carolyn's lab.

I would like to thank our collaborators Olaf S. Andersen and Radda Rusinova at Weill Cornell for technical and intellectual support during my trips to New York City. A large part of our most recent publication was enabled by their contributions, insight, and flexibility.

I would like to thank Richard Cerione for conversations about my work over the years, access to reagents, and training from his lab members, specifically, Marc Antonyak. Other faculty that I have enjoyed interacting with are Warren Zipfel and his endless knowledge of anything photon oriented, Hening Lin for fruitful conversations about my work as a committee member and head of the CBI training grant, and Maurine Linder for recognizing my application early on. I would like to extend my appreciation to everyone in the department who I have not named, but who have provide a constructive community to facilitate my growth as a scientist. In addition, I'd like to recognize the people behind the scene who keep the department running who include Greg Mitchell, Debbie Crane, Cindy Westmiller, and Robin Beebe.

Prior to Cornell, I was very lucky to have Jill B. Keeney as a research mentor. Jill introduced me to scientific research and gave me total independence from the first day in her laboratory. She treated me as a colleague more than a student and I cannot thank her enough for inspiring me.

I owe a great deal to the support of my friends, both from Ithaca and elsewhere. I need to thank Daniel D'Orazio for a decade of friendship and support. Years of scientific/philosophical dialogs, contemplative conversations, and uncountable experiences have proven to be invaluable. Adam Bisogni, a close friend and fellow graduate student, has been a friend since I moved to Ithaca. Our overlapping interests fostered an initial connection that developed into a beautiful friendship that I could not replace in a lifetime. Through Adam, I was lucky to meet Ben Gilmour, a kindred accomplice, who has expressed his unwavering support for me through the years as well as having a keen eye for proper wine to supply dinner parties with.

The most influential friends that I am indebted to are my parents, sister, brother-in-law, and wife: John, Donna, Linsey, Eric, and Haley. As far back as I can remember, they have all wholeheartedly encouraged and enabled my every milestone in life. I must recognize the untimely loss of my father during early graduate school, but more importantly, I must recognize the strength that my family has exhibited in keeping our family's legacy of wholehearted encouragement and love alive. I would also like to give my wife a special thanks for her unconditional love and support. She has truly been my foundation and closest friend for over a decade. Regardless of life's ebb and flow she stands next to me as the one constant I need when navigating forward. For that, I am forever grateful.

## TABLE OF CONTENTS

## LIST OF FIGURES

## LIST OF TABLES

# CHAPTER 1

# INTRODUCTION

*Membrane dynamics are architectural requirements of organelles.*

Biology relies on compartmentalization of specialized biochemical reactions. To achieve this, evolution has selected for sub-cellular compartments bound by lipid bilayers that are characteristic to eukaryotes; these structures are called organelles (Bogorad, 1975; Gabaldón and Pittis, 2015). The architectural requirements of organelles are quite diverse. On one hand, you need the lipid bilayer to confer structure and stability to preserve the unique environments for specialized biochemistry and function. However, these structures must remain amenable to membrane remodeling which enables cell division, organelle maintenance, membrane trafficking, and inter-organelle communication (Martens and McMahon, 2008; McNew et al., 2013).

Systems that regulate membrane dynamics are tunable, thus the balance between static and dynamic states can be maintained. Largely, these systems consist of merging two separate membranes or dividing a continuous membrane into two separate entities, these processes are termed fusion and fission respectively (**Figure 1.1**) (Kozlov et al., 2010). Membrane fusion begins when two separate membranes come increasingly proximal to each other (**Figure 1.1A**) until fusion is initiated when the outer-leaflets of the membranes interact, mix, and form a structure known as the hemifusion stalk intermediate (**Figure 1.1B; white**). As the stalk thins, a nonbilayer intermediate forms enabling inner-leaflet mixing and content from the two original sources to coalesce (**Figure 1.1C**) (Chernomordik et al., 1987; Kozlov and Markin, 1983).

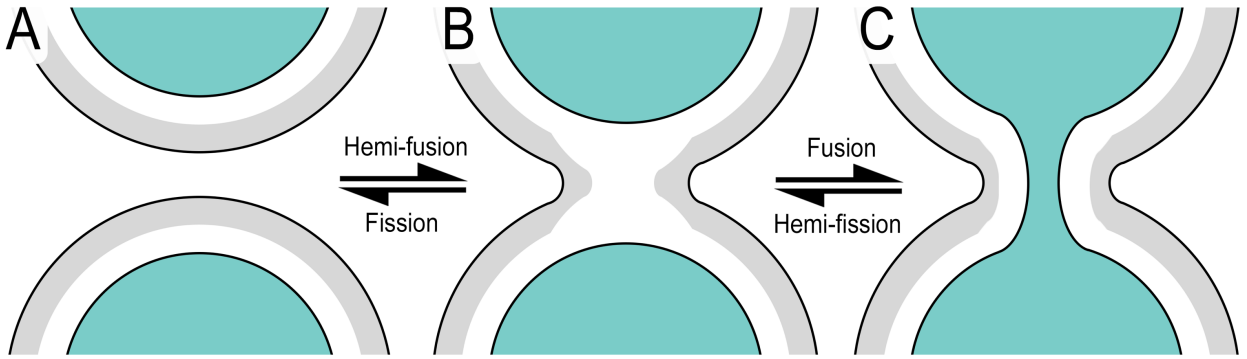


**Figure 1.1. Membrane Remodeling.** Membrane fusion initiates when two biological membranes become proximal to each other **(A)** and the outer-leaflets (*gray*) interact and mix. This results in a hemifusion stalk intermediate (*white*) **(B)**. As the stalk narrows, a nonbilayer intermediate enables inner-leaflet mixing, and the previously separate contents of the membranes coalesce (*teal*) **(C)**. Membrane fission samples the same fundamental intermediates but progresses in the opposite direction (C to A).

Conversely, membrane fission is enabled by constriction of a membrane neck (**Figure 1.1C**), and merging of the inner monolayer of the constricted neck generates a fission stalk, a structure synonymous to the fusion stalk (**Figure 1.1B; white**). After merging the outer-leaflet, two independent membranes are formed and fission is complete (Kozlov et al., 2010; Mattila et al., 2015) The aforementioned reactions are driven by forces required to minimize the exposure of the hydrophobic core of the lipid bilayer (Siegel, 1993).

Membrane fusion and fission are not spontaneous events and come at very high energetic costs. Thus, it is not surprising that protein catalysts have evolved to convert chemical energy into forces essential for remodeling biological membranes (Martens and McMahon, 2008). One major class of these enzymes is the dynamin-related proteins (DRPs), a family of large GTPases identified to regulate membrane remodeling and biological processes such as vesicle budding, division of organelles, cytokinesis,

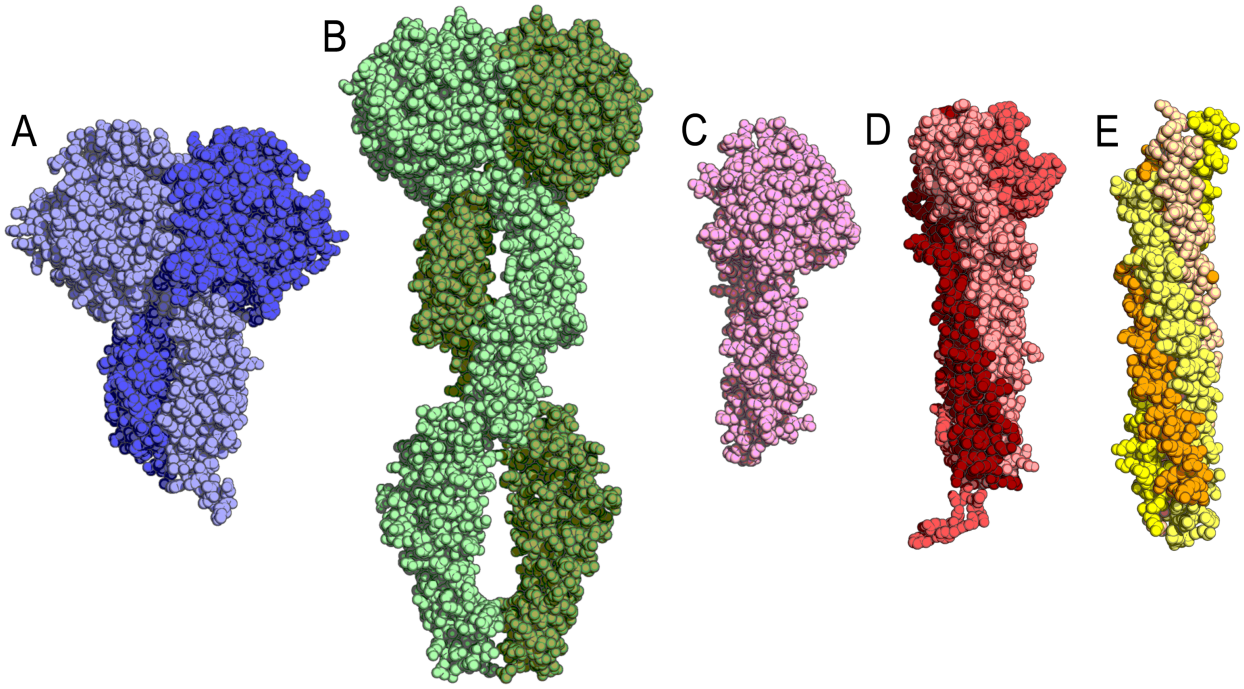


**Figure 1.2. Examples of membrane fusion machinery. (A)** human atlastin (*PDB: 4IDO; blue*) (Byrnes et al., 2013), **(B)** yeast Sey1p (*PDB: 5CA9; green*) (Yan et al., 2015), **(C)** human mitofusin (*PDB: 5GNU; pink*) (Qi et al., *to be published*), **(D)** influenza hemagglutinin (*PDB: 1QU1; red*) (J. Chen et al., 1999), **(E)** SNARE complex (*PDB: 1SFC; yellow*) (Sutton et al., 1998).

and pathogen resistance (Praefcke and McMahon, 2004). The most thoroughly studied member of this family is dynamin, a protein responsible for membrane fission. However, our primary focus will be understanding the fusion machinery required for maintaining proper endoplasmic reticulum (ER) morphology which is catalyzed by atlastin (ATL) (**Figure 1.2A**). ATLs transfer the chemical energy of guanosine triphosphate (GTP) hydrolysis to drive fusion (Orso et al., 2009). Theoretical models for energy requirements of membrane fusion range from 12-200 kT (Kuzmin et al., 2001; Lee and

Schick, 2008). The cleavage of a phosphoanhydride bond releases ~12 kT of energy placing the hydrolysis of GTP on par with the lowest theoretical energy requirement for fusion (Lipmann, 1941). However, DRPs are known to oligomerize which may increase the energetic contributions by investing a net-transfer of numerous hydrolysis energies into a fusion event (Byrnes and Sondermann, 2011; Cao et al., 2017; Hu and Rapoport, 2016).

Unfortunately, protein structures and mechanisms used in fusion are quite different. Fusion machineries can operate through many dissimilar means such as folding energies, homo- or heterotypic interactions, various initiation stimuli (pH, oligomerization, chemical energy), tethering-complexes, and conformational changes; many systems use one or more of the aforementioned schemes to achieve fusion (Weber et al., 1998; Ban et al., 2017; O'Donnell et al., 2017; Wu and Wilson, 2017). This diversity limits the amount of information that can be extrapolated between systems (**Figure 1.2**). This is even evident when comparing the structure of ATL (**Figure 1.2A**) to other DRP fusion proteins such as Sey1p (**Figure 1.2B**) and mitofusin (**Figure 1.2C**), proteins known to fuse the yeast ER and human outer-mitochondrial membrane respectively (Hu et al., 2009; Santel and Fuller, 2001). One of the earliest fusion machineries reported was influenza hemagglutinin protein, which uses membrane fusion as a means for viral entry. Mechanistically, virus-host fusion relies on a hydrophobic peptide that tethers the virus to endosomal membranes where a pH change induces a conformation change that deforms membranes to initiate outer-leaflet mixing (**Figure 1.2D**) (Wu and Wilson, 2017). Next is the prototypical example of cellular fusion which is executed by SNARE proteins. SNAREs predominantly fuse vesicles to

their target membranes through heterotypic oligomerization of v- and t-SNARES (**Figure 1.2E**) (Weber et al., 1998). With viral and SNARE mechanisms using folding energy to drive membrane fusion and DRP based fusion mechanisms relying on nucleotide hydrolysis energies, it is evident that mechanistic and structural requirements for fusion are diverse. These differences warrant a closer investigation of the lesser understood mechanisms of the DRP superfamily and how they function.

*Distinct and common features of dynamin related GTPases.*

The functional theme that permeates DRP members is their role in membrane remodeling. With that said, specific function and sites of action are distinct to the individual DRP (**Figure 1.3**) (Ferguson and De Camilli, 2012). Examples range from dynamin-mediated endocytosis, dynamin-based actin reorganization, DRP1-mediated fission of mitochondrial membrane, mitofusin/OPA1-mediated fusion of the outer/inner mitochondrial membranes, and fusion of the endoplasmic reticulum (ER) via ATLs (Detmer and Chan, 2007; Henley et al., 1998; Hu et al., 2009; Koenig and Ikeda, 1989; Krueger et al., 2003; Orso et al., 2009; van der Bliek and Meyerowitz, 1991). Two cytoplasmic DRPs responsible for innate immunity are outliers from this theme and include guanylate-binding protein (GBP) and MxA/B proteins that are both induced by interferons and up-regulated during times of infection (Cheng et al., 1983; Haller et al., 2010; Prakash et al., 2000a; Staeheli et al., 1986).

Despite differences in cellular localization and specific function, DRPs share common features. Most prominently, DRPs contain a large GTPase (G) domain responsible for hydrolyzing GTP which is structurally related to small G-proteins of the

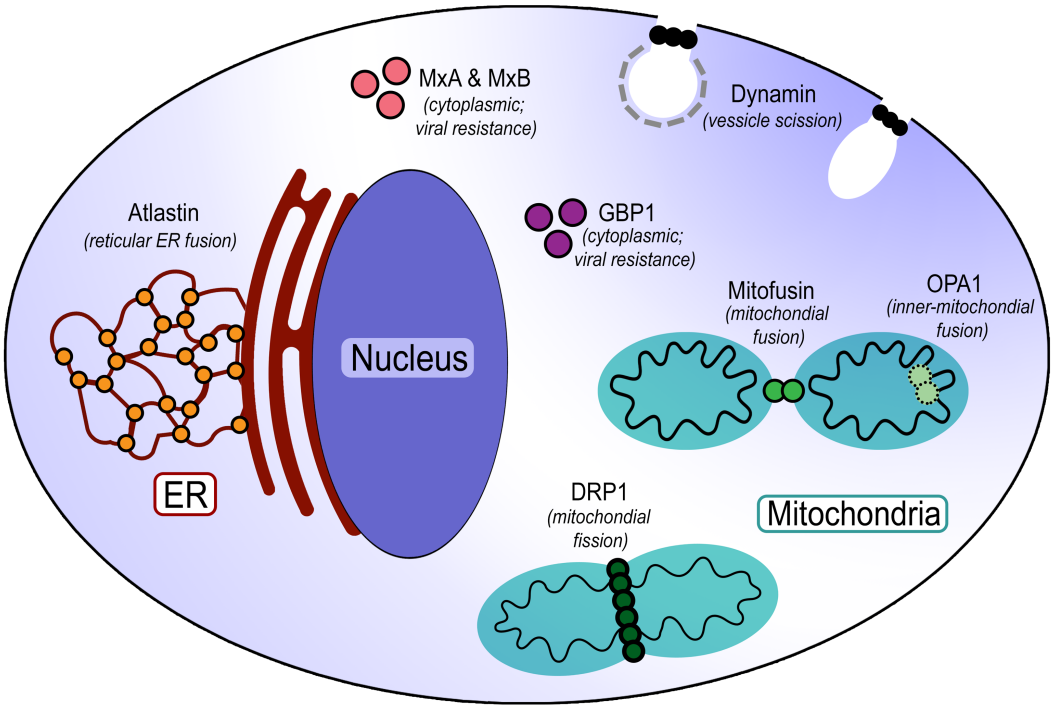


**Figure 1.3 Sites of action of dynamin and DRPs in a mammalian cell.** Dynamin is localized to many sites within the cell. The prototypical DRP, dynamin, is located at sites of endocytosis at both clathrin-coated pits and caveolae. MxA, MxB, and GBPs are largely soluble, reside in the cytoplasm, and confer viral resistance. Similar to dynamin, DRP1 catalyzes membrane fission, but DRP1 is unique to the mitochondria. Mitochondrial membrane fusion machinery is comprised of mitofusin and OPA1 which fuse the outer- and inner-mitochondrial membranes respectively. Atlastin is the sole fusogen of the endoplasmic reticulum and localizes to predominantly to membrane tubules of the smooth endoplasmic reticulum.

Ras superfamily. However, the G domains of the dynamin family are significantly larger (300 vs. 180 amino acids) and have a lower affinity for nucleotide. Despite the numerous genetic insertions resulting in an enlarged G domain, a comparison to the minimal Ras G domain depicts that the canonical GTP-binding motifs (G1-G4) are highly conserved with the exception of a hydrophobic residue replacing the catalytic glutamine residue following G3 (Daumke and Praefcke, 2016; Wittinghofer and Vetter,

2011). Regardless of similar switch regions, the small GTPases require heterotypic interactions with both GTPase activating proteins and guanine nucleotide exchange factors to toggle between catalytically competent states, and some DRPs utilize homodimerization for this purpose (Gasper et al., 2009). The process of homodimerization is also intimately tied to regulating the activities of GBP and dynamin (Chappie et al., 2010; Prakash et al., 2000a). Beyond the G domain, members often contain helical middle domains that can exhibit innate allosteric properties and serve to link the G domain to the membrane association motifs. Membrane anchoring can be mediated by pleckstrin homology domains, transmembrane helices, and lipid modifications (Britzen-Laurent et al., 2010; Byrnes et al., 2013; Praefcke and McMahon, 2004; Zhu et al., 2003). Some family members such as the prototypical dynamins, MxA, MxB, and GBP contain a GTPase effector domain (GED), which is inserted between the middle and membrane binding domains and mediates nucleotide-independent assembly (Haller et al., 2010; Hinshaw and Schmid, 1995; Prakash et al., 2000a; 2000b; Tuma and Collins, 1994; Warnock et al., 1996).

*Atlastins are distinct DRPs that catalyze fusion of the ER.*

ATLs are a subfamily of DRPs that catalyze the fusion of membrane tubules found in the smooth ER and form a distinct clade within the DRP superfamily as their sequence, domain topology, and mechanisms indicate (**Figure 1.4A; gray**) (Praefcke and McMahon, 2004; Rismanchi et al., 2008). ATL's domain architecture consists of cytoplasmic G and middle domains that are followed by an ER-specific transmembrane segment and a cytosolic amphipathic C-terminal helix required for fusion (**Figure 1.4B**)

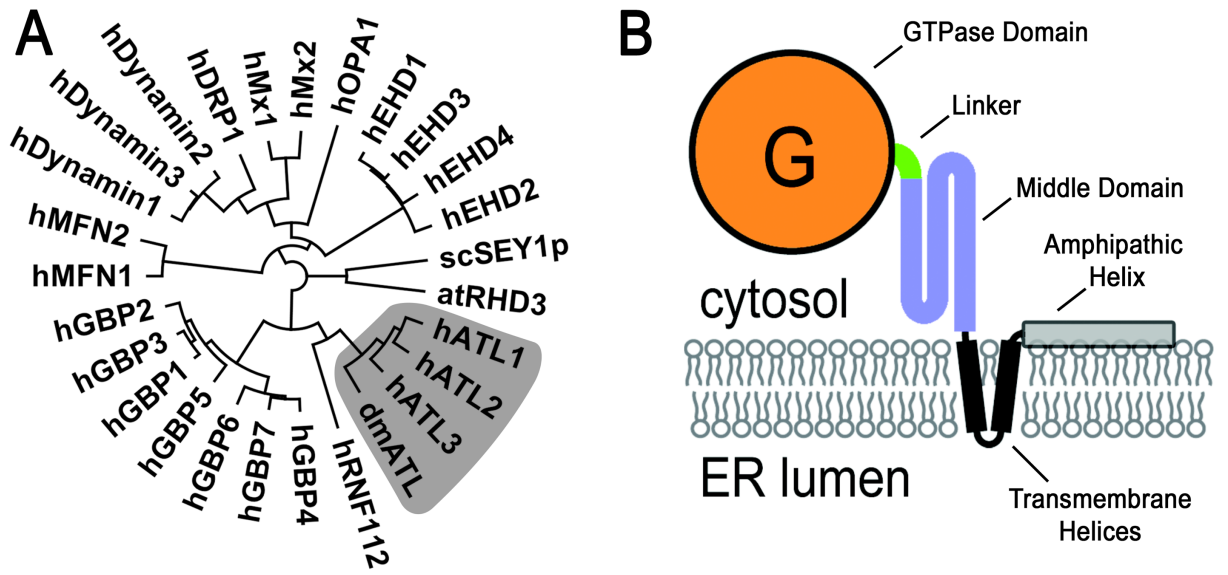


**Figure 1.4. ATLs and the DRP superfamily. (A)** The DRP superfamily tree is based on a multiple identity sequence alignment. ATLs are a distinct sub-family (ATLs, gray clade). **(B)** ATL membrane topology with G domain, linker, middle domain, and C-terminal amphipathic helix facing the cytosol.

(Faust et al., 2015; Hu et al., 2009; Liu et al., 2012). Strikingly, ATLs lack a GED, which is consistent with an apparent absence of higher order membrane assembly and oligomerization-based concerted conformational changes, a hallmark of canonical DRPs (Gasper et al., 2009; Ghosh et al., 2006; Warnock et al., 1996).

ATL was discovered as a mutated genetic locus that was a causative link to autosomal dominant Hereditary Spastic Paraplegia (HSP), a neurological disorder that manifests as progressive spastic weakness in distal-extremities (Fink, 2006; X. Zhao et al., 2001). Around the same time, a study determined that formation of a reticular ER network *in vitro* could be generated from a minimal input of liposomes derived from *Xenopus laevis* eggs, cytosol from the highest molecular weight fraction, and nucleotide-triphosphates (Dreier and Rapoport, 2000). Authors initially thought that

SNAREs were a likely explanation for ER formation, but their hypothesis was never substantiated, and the fusion machinery responsible remained elusive (Dreier and Rapoport, 2000). The first biochemical characterization of ATL established that the *SPG3A* gene product was membrane associated, formed oligomers, and hydrolyzed GTP to GDP and inorganic phosphate (Zhu et al., 2003). ATL function and ER morphology was not correlated until a comparative study defined the ATL family of GTPases and established that humans express three ATL isoforms with varying tissue expression (**Figure 1.4A**) (Rismanchi et al., 2008). Implication of ATL in ER three-way junction formation was evident from experiments where ATL levels were depleted with cellular siRNA treatments or cellular expression of known *SPG3A* dominant-negative mutations, which caused a prominent inhibition of ER reticularization (Rismanchi et al., 2008). A similar study determined that ATLs interact with tubule-shaping proteins, and ATLs are required for proper ER network formation both *in vivo* and *in vitro* (Hu et al., 2009). However, the direct connection between ATL and fusion of the ER was not discovered until a group investigated ATL function of the sole expressed isoform in *Drosophila melanogaster* (dmATL). This work corroborated evidence that loss of dmATL causes disruption of ER fragmentation in vivo, but more importantly, authors were able to reconstitute GTP-dependent fusion using only liposomes, dmATL, and GTP (Orso et al., 2009). The collective evidence that perturbing ATL levels or expression of dominant-negative alleles causes disruption of the reticular ER network in combination with dmATL mediating GTP-dependent fusion clearly defines ATL as the fusion machinery of the ER (Rismanchi et al., 2008; Hu et al., 2009; Orso et al., 2009). Coming full circle, the group responsible for initial reconstitution of *Xenopus* derived ER *in vitro* (Dreier and

Rapoport, 2000) has since reconstituted either dmATL or the yeast ATL ortholog (Sey1p) into pure lipid vesicles to achieve proper reticular ER formation, though Sey1p required the addition of curvature promoting proteins (Yop1p, Rtn1p, or REEP5) (Powers et al., 2017). This work defined the minimal units needed for ER network formation *in vitro*.

Biological relevance of ATLs.

*Axonopathies:* Human ATL1 was initially discovered through it's causal association with HSP. ATL1 mutations cause 10% of autosomal dominant HSP cases and are the most common in the early onset form of the disease (Fink, 2006). Early onset disease progression is insidious but tracks with development, leading to the assumption that ATL1 mutations are somehow linked to the spacial requirements of motor neurons and elongation (Blackstone et al., 2011; Zhu et al., 2006). In addition to HSP, both ATL1 and ATL3 have been implicated in pathogenesis of Hereditary Sensory Neuropath (HSN), an analogous disease to HSP that affects motor and sensory neurons (Fischer et al., 2014; Guelly et al., 2011; Kornak et al., 2014; Leonardis et al., 2012). Recently, common themes are emerging between the aforementioned axonopathies and how ER organization is disrupted (Renvoisé and Blackstone, 2010). One central role in this connection are mutations in membrane curvature promoting proteins that use hydrophobic wedges inserted into the lipid bilayer to induce curvature, which include the reticulons, REEPs, ARL6IP1, FAM134B, spastin, protrudin, and more (Chang et al., 2013; Hashimoto et al., 2014; Hubner and Kurth, 2014). Not surprisingly, ATL1 has been shown to make direct interactions with reticulons, REEPs, spastin, and

protrudin, which indicates a conserved functional role for these proteins in controlling proper ER shape and dynamics (Evans, 2006; Hu et al., 2009; Park et al., 2010). In addition to the axonopathy related proteins, a novel interaction between ATL and lunapark indicates that a proper expression of ATL, lunapark, and reticulons is required for ER formation and proper morphology in cells, though the molecular basis for these events remain unclear (S. Chen et al., 2014; 2012; Wang et al., 2016).

*Lipid Droplets:* Lipid droplets (LDs) are organelles that specialize in fat storage in higher eukaryotes and structurally consist of a neutral lipid core of triglycerides and sterol esters which are surrounded by a phospholipid monolayer (Walther and Farese, 2012). Lipid synthesis predominantly occurs in the smooth ER, which is known to interface with LDs to facilitate lipid transfer for subsequent storage (Q. Gao and Goodman, 2015; Markgraf et al., 2014). Control of lipid droplet size is largely unknown, but a study describes that ATL-mediated ER fusion is required for proper LD size regulation in *C. elegans*, *D melanogster*, and mammalian tissue culture (Klemm et al., 2013). Mutations in spastin or the removal of REEP1 in mice, both previously mentioned HSP-associated proteins known to interact with ATL, have been shown to effect LD targeting and induce abnormal LD morphologies (Papadopoulos et al., 2015; Renvoisé et al., 2016). Lipid biosynthesis proteins have also been shown to be mutated in various forms of HSP (Blackstone, 2012). These observations beg further investigation into the possibility that disruption of ER-assisted LD maintenance may have converging themes regarding HSP disease pathogenesis.

*Cancer and downstream cell signaling:* A proteomic analysis of glioblastoma membrane fractions indicates that ATL3 has a ~3 fold increase in expression and can

be corroborated via *Oncomine*, a cancer transciptome database (Polisetty et al., 2012; Rhodes et al., 2007). Another interesting observation from the *Oncomine* database is that ATL1 is often down regulated when ATL3 is enriched in cancers (*accessed: August 23, 2017*). Though speculation, these findings can be linked to cancer signaling pathways via ATL1-mediated regulation of bone morphogenic protein (BMP) signaling. In cell culture and zebrafish systems, defective ATL1 has been shown to enhance BMP receptor (BMPR) II and BMPRI trafficking respectively, which subsequently increases the activity of BMP signaling (Fassier et al., 2010; J. Zhao and Hedera, 2012). Though connections to ATL need to be determined, BMP signaling has been shown to be essential for axonal maintenance, tissue architecture, and decreasing tumorigenicity (Bayat et al., 2011; Bleuming et al., 2007; Q. Gao and Goodman, 2015; Matsuura et al., 2008).

*Novel implications for ATL function:* Recently, there have been numerous accounts of ATLs being involved with various biological processes. First, store-operated calcium entry (SOCE) is affected when ATL1 levels are modulated or dominant-negative ATL1 mutations are introduced. These changes result in a decreased number of STIM1 puncta at the plasma membrane during calcium depletion of the ER (Li et al., 2017). A direct interaction of SOCE machinery or STIM1 remains to be determined. Interestingly, the HSP-associated protein, RTN4, has been shown to effect STIM1-Orai1 coupling and SOCE; mechanistically RTN4-depleted cells exhibit a loss of proper STIM1 localization (Jozsef et al., 2014).

Second, it has been found that continuous GTP-hydrolysis of ATL is required for proper targeting of proteins to the inner nuclear membrane (Pawar et al., 2017).

Proteins destined to localize to the inner nuclear membrane rely on the continuity with the ER membrane but have the added hurdle of passing through the nuclear pore complex (NPC). Findings show that ATL-depletion results in loss of ability to diffuse between ER and inner nuclear membrane, NPC mislocalization, and untimely exiting of secretory cargo from the ER (Pawar et al., 2017).

Lastly, *Legionella pneumophila* replicates in a distinct ER-associated compartment where either ATL3 or Sey1p have been found to localize and enable host-pathogen interactions (Steiner et al., 2017). Once again, maintaining proper ER morphology and dynamics is established as a common theme amongst ATL-pertinent biological process; here, authors implicate this overarching theme in the maturation of *L. pneumophila* in their host.

*Mechanistic differences between dynamin and atlastin.*

Here it is important to dissect the GTP-dependent mechanisms employed by dynamin and ATL. Though a great deal of knowledge has been generated by extrapolating ATL function from dynamin, there are key differences that are important to highlight because they are points of contention in the field and mechanistic differences that we experimentally address in Chapter 2 (Byrnes et al., 2013; Liu et al., 2015; McNew et al., 2013; O'Donnell et al., 2017; Winsor et al., 2017).

*Dynamin:* As previously mentioned, dynamin is the best characterized DRP in context of its GTP-dependent membrane remodeling mechanisms and the structural rearrangements that enable its function (Antonny et al., 2016; Mettlen et al., 2009). Specifically, the helical middle domain and GED form a quaternary structure that leads

to oligomerization-dependent stimulation of GTP-hydrolysis (Chappie et al., 2011; Kenniston and Lemmon, 2010; Zhang and Hinshaw, 2001). A crystal structure of a minimal G domain-GED fusion protein revealed dimeric G domains in a catalytically competent transition state plays a role in the disassembly of dynamin coats from membrane tubes preceding the fission event (Bashkirov et al., 2008; Chappie et al., 2010). Membrane-mediated, higher-order oligomerization of dynamin stimulates its basal GTPase activity by two orders of magnitude (Tuma and Collins, 1994; Warnock et al., 1996), triggering a conformational change of the polymeric protein assembly, contributing to the fission event (Chappie et al., 2011; Faelber et al., 2011; Ford et al., 2011; Reubold et al., 2015). A similar model has been proposed for MxA, a dynamin-like protein involved in innate immunity (S. Gao et al., 2010). In summary, dynamins polymerize through higher-order oligomers on membranes, use GTP binding to dimerize through their G domains, stimulated GTP-hydrolysis leads to membrane constriction, and release of the monomers is concurrent with the fission event (**Figure 1.5A**).

*Atlastins:* The mechanistic foundation for ATL-mediated fusion can be attributed to three distinct crystallographic snapshots of the catalytic core fragment (G and middle domains) bound to GDP, non-hydrolyzable GTP, or transition state analogs (Byrnes et al., 2013; Byrnes and Sondermann, 2011) (**Figure 1.5B; crystal forms 1-3**). Structural analyses revealed two main conformational states, distinguished by the positions of the middle domain relative to their G domain. In one state (crystal form 2), the G and middle domains are engaged enabling the enzyme to bind GTP (Byrnes et al., 2013). In the other state (crystal forms 1 and 3), the middle domain is dislodged from the G domain and create homotypic interactions with the middle domain of an adjacent molecule in

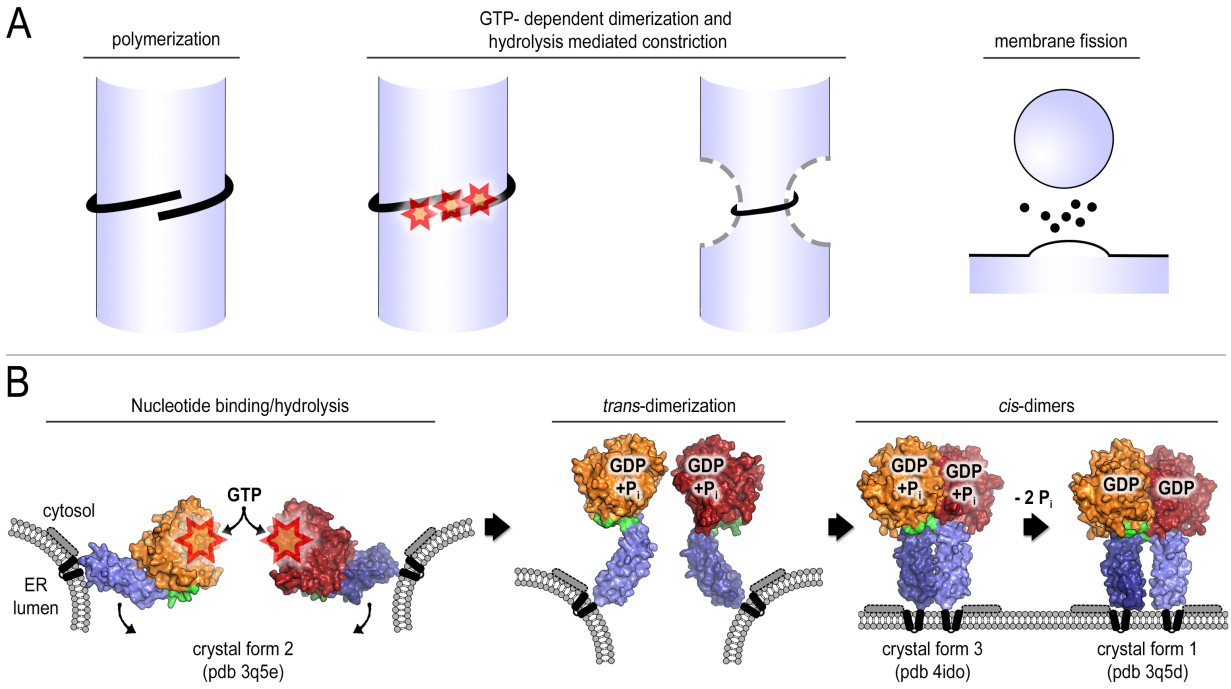


**Figure 1.5 Comparison of dynamin and atlastin mechanisms. (A)** Overview of dynamin fission event where protomers polymerize on a membrane surface, GTP-binding mediates G domain dimerization, hydrolysis is stimulated in the higher-order oligomeric state enabling membrane deformation. Dynamin release coincides with the fission event (dynamin, black ring and spheres). *Figure inspired by (Ferguson and De Camilli, 2012.* **(B)** Overview of atlastin fusion where GTP-binding and hydrolysis is initiated in the monomeric protomer. Release of the G and middle domains is followed by rapid homodimerization bringing membranes within close proximity to one anther enabling fusion (G domain, orange/red; middle domains, slate/dark blue).

the crystal lattice. The ATL core fragment dimerizes upon incubation with non-hydrolyzable GTP and transition state analogs, but not in the presence of GDP or in its apo-state (Byrnes and Sondermann, 2011). Pre-steady state kinetic measurements indicates that nucleotide hydrolysis drives fast dimerization (in the order of seconds), whereas with non-hydrolyzable analogs protein dimerization requires longer (non-physiological) equilibration times (in the order of minutes) (Byrnes et al., 2013).

Because non-hydrolyzable analogs are not able to produce fast kinetics of dimerization, we prefer a model where the G domain binds GTP and either hydrolysis or the transition-state promotes the rapid dimerization of both G and middle domain on the same time scale (**Figure 1.5B**). This step allows ATL's G and middle domains to form a tight tether between opposing membranes *in trans* and result in a fusion event. Alternative models proposed by others favor G domain dimerization that is dependent on GTP binding but not hydrolysis as the step to establish the enzymatically competent state of ATL, in analogy to other DRPs (Liu et al., 2015; Morin-Leisk et al., 2011; Saini et al., 2014; Ulengin et al., 2015; Winsor et al., 2017). However, these studies allow for alternative interpretations, in part due to the omission of crucial controls and the fact that they were conducted under different, arguably not directly comparable conditions. To clarify ATL's mechanism, we must establish the precise timing of events in ATL's functional cycle, elucidate transient intermediates, determine when hydrolysis occurs, and investigate if activity is stimulated by ATL oligomerization. These questions are the subject of Chapter 2, and this study's outcome helps to unify our understanding of ATL-mediated membrane fusion. The tools developed and conclusions made in Chapter 2 become the foundation for investigating how an atypical HSP mutation effects ATL function which leads us to a novel mechanism for inter-domain allosteric coupling of ATLs (Chapter 3).

## REFERENCES


Antonny, B., Burd, C., De Camilli, P., Chen, E., Daumke, O., Faelber, K., Ford, M., Frolov, V.A., Frost, A., Hinshaw, J.E., Kirchhausen, T., Kozlov, M.M., Lenz, M., Low, H.H., McMahon, H., Merrifield, C., Pollard, T.D., Robinson, P.J., Roux, A., Schmid, S., 2016. Membrane fission by dynamin: what we know and what we need to know. EMBO J. 35, 2270–2284. doi:10.15252/embj.201694613

Bashkirov, P.V., Akimov, S.A., Evseev, A.I., Schmid, S.L., Zimmerberg, J., Frolov, V.A., 2008. GTPase cycle of dynamin is coupled to membrane squeeze and release, leading to spontaneous fission. Cell 135, 1276–1286. doi:10.1016/j.cell.2008.11.028

Ban, T., Ishihara, T., Kohno, H., Saita, S., Ichimura, A., Maenaka, K., Oka, T., Mihara, K., Ishihara, N., 2017. Molecular basis of selective mitochondrial fusion by heterotypic action between OPA1 and cardiolipin. Nat. Cell Biol. 505, 335–14. doi:10.1038/ncb3560

Bayat, V., Jaiswal, M., Bellen, H.J., 2011. The BMP signaling pathway at the Drosophila neuromuscular junction and its links to neurodegenerative diseases. Current Opinion in Neurobiology 21, 182–188. doi:10.1016/j.conb.2010.08.014

Blackstone, C., 2012. Cellular pathways of hereditary spastic paraplegia. Annu. Rev. Neurosci. 35, 25–47. doi:10.1146/annurev-neuro-062111-150400

Blackstone, C., O'Kane, C.J., Reid, E., 2011. Hereditary spastic paraplegias: membrane traffic and the motor pathway. Nat. Rev. Neurosci. 12, 31–42. doi:10.1038/nrn2946

Bleuming, S.A., He, X.C., Kodach, L.L., Hardwick, J.C., Koopman, F.A., Kate, Ten, F.J., van Deventer, S.J.H., Hommes, D.W., Peppelenbosch, M.P., Offerhaus, G.J., Li, L., van den Brink, G.R., 2007. Bone morphogenetic protein signaling suppresses tumorigenesis at gastric epithelial transition zones in mice. Cancer Res. 67, 8149–8155. doi:10.1158/0008-5472.CAN-06-4659

Bogorad, L., 1975. Evolution of organelles and eukaryotic genomes. Science 188, 891–898. doi:10.2307/1740819

Britzen-Laurent, N., Bauer, M., Berton, V., Fischer, N., Syguda, A., Reipschläger, S., Naschberger, E., Herrmann, C., Stürzl, M., 2010. Intracellular trafficking of

guanylate-binding proteins is regulated by heterodimerization in a hierarchical manner. PLoS ONE 5, e14246–11. doi:10.1371/journal.pone.0014246

Byrnes, L.J., Singh, A., Szeto, K., Benvin, N.M., O'Donnell, J.P., Zipfel, W.R., Sondermann, H., 2013. Structural basis for conformational switching and GTP loading of the large G protein atlastin. EMBO J. 32, 369–384. doi:10.1038/emboj.2012.353

Byrnes, L.J., Sondermann, H., 2011. Structural basis for the nucleotide-dependent dimerization of the large G protein atlastin-1/SPG3A. Proc. Natl. Acad. Sci. U.S.A. 108, 2216–2221. doi:10.1073/pnas.1012792108

Cao, Y.-L., Meng, S., Chen, Y., Feng, J.-X., Gu, D.-D., Yu, B., Li, Y.-J., Yang, J.-Y., Liao, S., Chan, D.C., Gao, S., 2017. MFN1 structures reveal nucleotide-triggered dimerization critical for mitochondrial fusion. Nature 1–5. doi:10.1038/nature21077

Chang, J., Lee, S., Blackstone, C., 2013. Protrudin binds atlastins and endoplasmic reticulum-shaping proteins and regulates network formation. Proc. Natl. Acad. Sci. U.S.A. 110, 14954–14959. doi:10.1073/pnas.1307391110

Chappie, J., Mears, J., Fang, S., Leonard, M., Schmid, S., Milligan, R., Hinshaw, J., Dyda, F., 2011. A Pseudoatomic Model of the Dynamin Polymer Identifies a Hydrolysis-Dependent Powerstroke. Cell 147, 14–222. doi:10.1016/j.cell.2011.09.003

Chappie, J.S., Acharya, S., Leonard, M., Schmid, S.L., Dyda, F., 2010. G domain dimerization controls dynamin's assembly-stimulated GTPase activity. Nature 465, 435–440. doi:10.1038/nature09032

Chen, J., Skehel, J.J., Wiley, D.C., 1999. N- and C-terminal residues combine in the fusion-pH influenza hemagglutinin HA2 subunit to form an N cap that terminates the triple-stranded coiled coil. Proc Natl Acad Sci USA 96, 8967–8972. doi:10.1073/pnas.96.16.8967

Chen, S., Desai, T., McNew, J.A., Gerard, P., Novick, P.J., Ferro-Novick, S., 2014. Lunapark stabilizes nascent three-way junctions in the endoplasmic reticulum. Proc. Natl. Acad. Sci. U.S.A. 201423026. doi:10.1073/pnas.1423026112

Chen, S., Novick, P., Ferro-Novick, S., 2012. ER network formation requires a balance of the dynamin-like GTPase Sey1p and the Lunapark family member Lnp1p. Nat. Cell Biol. 14, 707–716. doi:10.1038/ncb2523

Cheng, Y.S., Colonno, R.J., Yin, F.H., 1983. Interferon induction of fibroblast proteins with guanylate binding activity. J. Biol. Chem. 258, 7746–7750.

Chernomordik, L.V., Melikyan, G.B., Chizmadzhev, Y.A., 1987. Biomembrane fusion: a new concept derived from model studies using two interacting planar lipid bilayers. Biochimica et Biophysica Acta (BBA) - Reviews on Biomembranes 906, 309–352. doi:10.1016/0304-4157(87)90016-5

Daumke, O., Praefcke, G.J.K., 2016. Invited review: Mechanisms of GTP hydrolysis and conformational transitions in the dynamin superfamily. Biopolymers 105, 580–593. doi:10.1002/bip.22855

Detmer, S.A., Chan, D.C., 2007. Functions and dysfunctions of mitochondrial dynamics. Nat Rev Mol Cell Biol 8, 870–879. doi:10.1038/nrm2275

Dreier, L., Rapoport, T.A., 2000. In vitro formation of the endoplasmic reticulum occurs independently of microtubules by a controlled fusion reaction. The Journal of Cell Biology 148, 883–898.

Evans, K., 2006. Interaction of two hereditary spastic paraplegia gene products, spastin and atlastin, suggests a common pathway for axonal maintenance. Proc. Natl. Acad. Sci. U.S.A. 103, 10666–10671. doi:10.1073/pnas.0510863103

Faelber, K., Posor, Y., Gao, S., Held, M., Roske, Y., Schulze, D., Haucke, V., Noé, F., Daumke, O., 2011. Crystal structure of nucleotide-free dynamin. Nature 477, 556–560. doi:10.1038/nature10369

Fassier, C., Hutt, J.A., Scholpp, S., Lumsden, A., Giros, B., Nothias, F., Schneider-Maunoury, S., Houart, C., Hazan, J., 2010. Zebrafish atlastin controls motility and spinal motor axon architecture via inhibition of the BMP pathway. Nat Neurosci 13, 1380–1387. doi:10.1038/nn.2662

Faust, J.E., Desai, T., Verma, A., Ulengin, I., Sun, T.-L., Moss, T.J., Betancourt-Solis, M.A., Huang, H.W., Lee, T., McNew, J.A., 2015. The Atlastin C-terminal Tail Is an

Amphipathic Helix That Perturbs the Bilayer Structure during Endoplasmic Reticulum Homotypic Fusion. J. Biol. Chem. 290, 4772–4783. doi:10.1074/jbc.M114.601823

Ferguson, S.M., De Camilli, P., 2012. Dynamin, a membrane-remodelling GTPase. Nat Rev Mol Cell Biol 13, 75–88. doi:10.1038/nrm3266

Fink, J.K., 2006. Hereditary spastic paraplegia. Curr Neurol Neurosci Rep 6, 65–76.

Fischer, D., Schabhuttl, M., Wieland, T., Windhager, R., Strom, T.M., Auer-Grumbach, M., 2014. A novel missense mutation confirms ATL3 as a gene for hereditary sensory neuropathy type 1. Brain 137, e286–e286. doi:10.1093/brain/awu091

Ford, M.G.J., Jenni, S., Nunnari, J., 2011. The crystal structure of dynamin. Nature 477, 561–566. doi:10.1038/nature10441

Gabaldón, T., Pittis, A.A., 2015. Origin and evolution of metabolic sub-cellular compartmentalization in eukaryotes. Biochimie 119, 262–268. doi:10.1016/j.biochi.2015.03.021

Gao, Q., Goodman, J.M., 2015. The lipid droplet—a well-connected organelle. Front. Cell Dev. Biol. 3, 367–12. doi:10.3389/fcell.2015.00049

Gao, S., Malsburg, von der, A., Paeschke, S., Behlke, J., Haller, O., Kochs, G., Daumke, O., 2010. Structural basis of oligomerization in the stalk region of dynamin-like MxA. Nature Publishing Group 465, 502–506. doi:10.1038/nature08972

Gasper, R., Meyer, S., Gotthardt, K., Sirajuddin, M., Wittinghofer, A., 2009. It takes two to tango: regulation of G proteins by dimerization. Nat Rev Mol Cell Biol 10, 423–429. doi:10.1038/nrm2689

Ghosh, A., Praefcke, G.J.K., Renault, L., Wittinghofer, A., Herrmann, C., 2006. How guanylate-binding proteins achieve assembly-stimulated processive cleavage of GTP to GMP. Nature 440, 101–104. doi:10.1038/nature04510

Guelly, C., Zhu, P.-P., Leonardis, L., Papić, L., Zidar, J., Schabhüttl, M., Strohmaier, H., Weis, J., Strom, T.M., Baets, J., Willems, J., De Jonghe, P., Reilly, M.M., Fröhlich, E., Hatz, M., Trajanoski, S., Pieber, T.R., Janecke, A.R., Blackstone, C., Auer-

Grumbach, M., 2011. Targeted high-throughput sequencing identifies mutations in atlastin-1 as a cause of hereditary sensory neuropathy type I. Am. J. Hum. Genet. 88, 99–105. doi:10.1016/j.ajhg.2010.12.003

Haller, O., Gao, S., Malsburg, von der, A., Daumke, O., Kochs, G., 2010. Dynamin-like MxA GTPase: Structural Insights into Oligomerization and Implications for Antiviral Activity. Journal of Biological Chemistry 285, 28419–28424. doi:10.1074/jbc.R110.145839

Hashimoto, Y., Shirane, M., Matsuzaki, F., Saita, S., Ohnishi, T., Nakayama, K.I., 2014. Protrudin Regulates Endoplasmic Reticulum Morphology and Function Associated with the Pathogenesis of Hereditary Spastic Paraplegia. Journal of Biological Chemistry. doi:10.1074/jbc.M113.528687

Henley, J.R., Krueger, E.W.A., Oswald, B.J., McNiven, M.A., 1998. Dynamin-mediated Internalization of Caveolae. The Journal of Cell Biology 141, 85–99. doi:10.1083/jcb.141.1.85

Hinshaw, J.E., Schmid, S.L., 1995. Dynamin self-assembles into rings suggesting a mechanism for coated vesicle budding. Nature 374, 190–192. doi:10.1038/374190a0

Hu, J., Rapoport, T.A., 2016. Fusion of the endoplasmic reticulum by membrane-bound GTPases. Semin. Cell Dev. Biol. 1–7. doi:10.1016/j.semcdb.2016.06.001

Hu, J., Shibata, Y., Zhu, P.-P., Voss, C., Rismanchi, N., Prinz, W.A., Rapoport, T.A., Blackstone, C., 2009. A Class of Dynamin-like GTPases Involved in the Generation of the Tubular ER Network. Cell 138, 549–561. doi:10.1016/j.cell.2009.05.025

Hubner, C.A., Kurth, I., 2014. Membrane-shaping disorders: a common pathway in axon degeneration. Brain 137, 3109–3121. doi:10.1093/brain/awu287

Jozsef, L., Tashiro, K., Kuo, A., Park, E.J., Skoura, A., Albinsson, S., Rivera-Molina, F., Harrison, K.D., Iwakiri, Y., Toomre, D., Sessa, W.C., 2014. Reticulon 4 is necessary for endoplasmic reticulum tubulation, STIM1-Orai1 coupling, and store-operated calcium entry. Journal of Biological Chemistry 289, 9380–9395. doi:10.1074/jbc.M114.548602

Kenniston, J.A., Lemmon, M.A., 2010. Dynamin GTPase regulation is altered by PH domain mutations found in centronuclear myopathy patients. EMBO J. 29, 3054–3067. doi:10.1038/emboj.2010.187

Klemm, R.W., Norton, J.P., Cole, R.A., Li, C.S., Park, S.H., Crane, M.M., Li, L., Jin, D., Boye-Doe, A., Liu, T.Y., Shibata, Y., Lu, H., Rapoport, T.A., Farese, R.V., Blackstone, C., Guo, Y., Mak, H.Y., 2013. A Conserved Role for Atlastin GTPases in Regulating Lipid Droplet Size. Cell Rep 3, 1465–1475. doi:10.1016/j.celrep.2013.04.015

Koenig, J.H., Ikeda, K., 1989. Disappearance and reformation of synaptic vesicle membrane upon transmitter release observed under reversible blockage of membrane retrieval. Journal of Neuroscience 9, 3844–3860.

Kornak, U., Mademan, I., Schinke, M., Voigt, M., Krawitz, P., Hecht, J., Barvencik, F., Schinke, T., Giesselmann, S., Beil, F.T., Pou-Serradell, A., Vilchez, J.J., Beetz, C., Deconinck, T., Timmerman, V., Kaether, C., De Jonghe, P., Hubner, C.A., Gal, A., Amling, M., Mundlos, S., Baets, J., Kurth, I., 2014. Sensory neuropathy with bone destruction due to a mutation in the membrane-shaping atlastin GTPase 3. Brain. doi:10.1093/brain/awt357

Kozlov, M.M., Markin, V.S., 1983. Possible mechanism of membrane fusion. Biofizika 28, 242–247.

Kozlov, M.M., McMahon, H.T., Chernomordik, L.V., 2010. Protein-driven membrane stresses in fusion and fission. Trends in Biochemical Sciences 35, 699–706. doi: 10.1016/j.tibs.2010.06.003

Krueger, E.W., Orth, J.D., Cao, H., McNiven, M.A., 2003. A dynamin-cortactin-Arp2/3 complex mediates actin reorganization in growth factor-stimulated cells. Molecular Biology of the Cell 14, 1085–1096. doi:10.1091/mbc.E02-08-0466

Kuzmin, P.I., Zimmerberg, J., Chizmadzhev, Y.A., Cohen, F.S., 2001. A quantitative model for membrane fusion based on low-energy intermediates. Proc Natl Acad Sci USA 98, 7235–7240. doi:10.1073/pnas.121191898

Lee, J.Y., Schick, M., 2008. Calculation of Free Energy Barriers to the Fusion of Small Vesicles. Biophys. J. 94, 1699–1706. doi:10.1529/biophysj.107.119511

Leonardis, L., Auer-Grumbach, M., Papić, L., Zidar, J., 2012. The N355K atlastin 1 mutation is associated with hereditary sensory neuropathy and pyramidal tract features. Eur. J. Neurol. 19, 992–998. doi:10.1111/j.1468-1331.2012.03665.x

Li, J., Yan, B., Si, H., Peng, X., Zhang, S.L., Hu, J., 2017. Atlastin regulates store-operated calcium entry for nerve growth factor-induced neurite outgrowth. Sci Rep 7, 43490. doi:10.1038/srep43490

Lipmann, F., 1941. Metabolic generation and utilization of phosphate bond energy. Adv Enzymol 1, 99–162.

Liu, T.Y., Bian, X., Romano, F.B., Shemesh, T., Rapoport, T.A., Hu, J., 2015. Cis and trans interactions between atlastin molecules during membrane fusion. Proc. Natl. Acad. Sci. U.S.A. 112, E1851–60. doi:10.1073/pnas.1504368112

Liu, T.Y., Bian, X., Sun, S., Hu, X., Klemm, R.W., Prinz, W.A., Rapoport, T.A., Hu, J., 2012. Lipid interaction of the C terminus and association of the transmembrane segments facilitate atlastin-mediated homotypic endoplasmic reticulum fusion. Proc. Natl. Acad. Sci. U.S.A. 109, E2146–54. doi:10.1073/pnas.1208385109

Markgraf, D.F., Klemm, R.W., Junker, M., Hannibal-Bach, H.K., Ejsing, C.S., Rapoport, T.A., 2014. An ER Protein Functionally Couples Neutral Lipid Metabolism on Lipid Droplets to Membrane Lipid Synthesis in the ER. Cell Rep 6, 44–55. doi:10.1016/j.celrep.2013.11.046

Martens, S., McMahon, H.T., 2008. Mechanisms of membrane fusion: disparate players and common principles. Nat Rev Mol Cell Biol 9, 543–556. doi:10.1038/nrm2417

Matsuura, I., Taniguchi, J., Hata, K., Saeki, N., Yamashita, T., 2008. BMP inhibition enhances axonal growth and functional recovery after spinal cord injury. J. Neurochem. 105, 1471–1479. doi:10.1111/j.1471-4159.2008.05251.x

Mattila, J.-P., Shnyrova, A.V., Sundborger, A.C., Hortelano, E.R., Fuhrmans, M., Neumann, S., Müller, M., Hinshaw, J.E., Schmid, S.L., Frolov, V.A., 2015. A hemi-fission intermediate links two mechanistically distinct stages of membrane fission. Nature Publishing Group 524, 109–113. doi:10.1038/nature14509

McNew, J.A., Sondermann, H., Lee, T., Stern, M., Brandizzi, F., 2013. GTP-Dependent Membrane Fusion. Annu. Rev. Cell Dev. Biol. 29, 529–550. doi:10.1146/annurev-cellbio-101512-122328

Mettlen, M., Pucadyil, T., Ramachandran, R., Schmid, S.L., 2009. Dissecting dynamin's role in clathrin-mediated endocytosis. Biochem. Soc. Trans 37, 1022–1026. doi: 10.1042/BST0371022

Morin-Leisk, J., Saini, S.G., Meng, X., Makhov, A.M., Zhang, P., Lee, T.H., 2011. An intramolecular salt bridge drives the soluble domain of GTP-bound atlastin into the postfusion conformation. The Journal of Cell Biology 195, 605–615. doi:10.1083/jcb. 201105006

O'Donnell, J.P., Cooley, R.B., Kelly, C.M., Miller, K., Andersen, O.S., Rusinova, R., Sondermann, H., 2017. Timing and Reset Mechanism of GTP Hydrolysis- Driven Conformational Changes of Atlastin. Structure 1–29. doi:10.1016/j.str.2017.05.007

Orso, G., Pendin, D., Liu, S., Tosetto, J., Moss, T.J., Faust, J.E., Micaroni, M., Egorova, A., Martinuzzi, A., McNew, J.A., Daga, A., 2009. Homotypic fusion of ER membranes requires the dynamin-like GTPase atlastin. Nature 460, 978–983. doi: 10.1038/nature08280

Papadopoulos, C., Orso, G., Mancuso, G., Herholz, M., Gumeni, S., Tadepalle, N., Jüngst, C., Tzschichholz, A., Schauss, A., Höning, S., Trifunovic, A., Daga, A., Rugarli, E.I., 2015. Spastin Binds to Lipid Droplets and Affects Lipid Metabolism. PLoS Genet. 11, e1005149–27. doi:10.1371/journal.pgen.1005149

Park, S.H., Zhu, P.-P., Parker, R.L., Blackstone, C., 2010. Hereditary spastic paraplegia proteins REEP1, spastin, and atlastin-1 coordinate microtubule interactions with the tubular ER network. J. Clin. Invest. 120, 1097–1110. doi:10.1172/JCI40979DS1

Pawar, S., Ungricht, R., Tiefenboeck, P., Leroux, J.-C., Kutay, U., 2017. Efficient protein targeting to the inner nuclear membrane requires atlastin-dependent maintenance of ER topology. eLife 6. doi:eLife 2017;6:e28202 / 10.7554/eLife.28202

Polisetty, R.V., Gautam, P., Sharma, R., Harsha, H.C., Nair, S.C., Gupta, M.K., Uppin, M.S., Challa, S., Puligopu, A.K., Ankathi, P., Purohit, A.K., Chandak, G.R., Pandey, A., Sirdeshmukh, R., 2012. LC-MS/MS Analysis of Differentially Expressed

Glioblastoma Membrane Proteome Reveals Altered Calcium Signaling and Other Protein Groups of Regulatory Functions 11, M111.013565–M111.013565. doi: 10.1074/mcp.M111.013565

Powers, R.E., Wang, S., Liu, T.Y., Rapoport, T.A., 2017. Reconstitution of the tubular endoplasmic reticulum network with purified components. Nature. doi:10.1038/nature21387

Praefcke, G.J.K., McMahon, H.T., 2004. The dynamin superfamily: universal membrane tubulation and fission molecules? Nat Rev Mol Cell Biol 5, 133–147. doi:10.1038/nrm1313

Prakash, B., Praefcke, G.J., Renault, L., Wittinghofer, A., Herrmann, C., 2000a. Structure of human guanylate-binding protein 1 representing a unique class of GTP-binding proteins. Nature 403, 567–571. doi:10.1038/35000617

Prakash, B., Renault, L., Praefcke, G.J.K., Herrmann, C., Wittinghofer, A., 2000b. Triphosphate structure of guanylate-binding protein 1 and implications for nucleotide binding and GTPase mechanism. EMBO J. 19, 4555–4564. doi:10.1093/emboj/19.17.4555

Renvoisé, B., Blackstone, C., 2010. Emerging themes of ER organization in the development and maintenance of axons. Current Opinion in Neurobiology 20, 531–537. doi:10.1016/j.conb.2010.07.001

Renvoisé, B., Malone, B., Falgairolle, M., Munasinghe, J., Stadler, J., Sibilla, C., Park, S.H., Blackstone, C., 2016. Reep1null mice reveal a converging role for hereditary spastic paraplegia proteins in lipid droplet regulation. Human Molecular Genetics ddw315–15. doi:10.1093/hmg/ddw315

Reubold, T.F., Faelber, K., Plattner, N., Posor, Y., Ketel, K., Curth, U., Schlegel, J., Anand, R., Manstein, D.J., Noé, F., Haucke, V., Daumke, O., Eschenburg, S., 2015. Crystal structure of the dynamin tetramer. Nature 1–23. doi:10.1038/nature14880

Rhodes, D.R., Kalyana-Sundaram, S., Mahavisno, V., Varambally, R., Yu, J., Briggs, B.B., Barrette, T.R., Anstet, M.J., Kincead-Beal, C., Kulkarni, P., Varambally, S., Ghosh, D., Chinnaiyan, A.M., 2007. Oncomine 3.0: genes, pathways, and networks in a collection of 18,000 cancer gene expression profiles. Neoplasia 9, 166–180.

Rismanchi, N., Soderblom, C., Stadler, J., Zhu, P.P., Blackstone, C., 2008. Atlastin GTPases are required for Golgi apparatus and ER morphogenesis. Human Molecular Genetics 17, 1591–1604. doi:10.1093/hmg/ddn046

Saini, S.G., Liu, C., Lee, T.H., 2014. Membrane tethering by the atlastin GTPase depends on GTP hydrolysis but not on forming the cross-over configuration. Molecular Biology of the Cell 25, 3942–3953. doi:10.1091/mbc.E14-08-1284

Santel, A., Fuller, M.T., 2001. Control of mitochondrial morphology by a human mitofusin. J. Cell. Sci. 114, 867–874. doi:10.1006/jmbi.1990.9999

Siegel, D.P., 1993. Energetics of intermediates in membrane fusion: comparison of stalk and inverted micellar intermediate mechanisms. Biophys. J. 65, 2124–2140. doi: 10.1016/S0006-3495(93)81256-6

Staeheli, P., Haller, O., Boll, W., Lindenmann, J., Weissmann, C., 1986. Mx protein: constitutive expression in 3T3 cells transformed with cloned Mx cDNA confers selective resistance to influenza virus. Cell 44, 147–158.

Steiner, B., Swart, A.L., Welin, A., Weber, S., Personnic, N., Kaech, A., Freyre, C., Ziegler, U., Klemm, R.W., Hilbi, H., 2017. ER remodeling by the large GTPase atlastin promotes vacuolar growth of Legionella pneumophila. EMBO Rep. 1–20. doi:10.15252/embr.201743903

Sutton, R.B., Fasshauer, D., Jahn, R., Brunger, A.T., 1998. Crystal structure of a SNARE complex involved in synaptic exocytosis at 2.4 angstrom resolution - ProQuest. Nature.

Tuma, P.L., Collins, C.A., 1994. Activation of dynamin GTPase is a result of positive cooperativity. J. Biol. Chem. 269, 30842–30847.

Ulengin, I., Park, J.J., Lee, T.H., 2015. ER network formation and membrane fusion by atlastin1/SPG3A disease variants. Molecular Biology of the Cell 26, 1616–1628. doi: 10.1091/mbc.E14-10-1447

van der Bliek, A.M., Meyerowitz, E.M., 1991. Dynamin-like protein encoded by the Drosophila shibire gene associated with vesicular traffic. Nature 351, 411–414. doi: 10.1038/351411a0

Walther, T.C., Farese, R.V., Jr, 2012. Lipid Droplets and Cellular Lipid Metabolism. http://dx.doi.org.proxy.library.cornell.edu/10.1146/annurev-biochem-061009-102430. doi: 10.1146/annurev-biochem-061009-102430

Wang, S., Tukachinsky, H., Romano, F.B., Rapoport, T.A., 2016. Cooperation of the ER-shaping proteins atlastin, lunapark, and reticulons to generate a tubular membrane network. eLife 5, 209. doi:10.7554/eLife.18605

Warnock, D.E., Hinshaw, J.E., Schmid, S.L., 1996. Dynamin self-assembly stimulates its GTPase activity. J. Biol. Chem. 271, 22310–22314.

Weber, T., Zemelman, B.V., McNew, J.A., Westermann, B., Gmachl, M., Parlati, F., Söllner, T.H., Rothman, J.E., 1998. SNAREpins: Minimal Machinery for Membrane Fusion. Cell 92, 759–772. doi:10.1016/S0092-8674(00)81404-X

Winsor, J., Hackney, D.D., Lee, T.H., 2017. The crossover conformational shift of the GTPase atlastin provides the energy driving ER fusion. The Journal of Cell Biology jcb.201609071. doi:10.1083/jcb.201609071

Wittinghofer, A., Vetter, I.R., 2011. Structure-function relationships of the G domain, a canonical switch motif. Annu. Rev. Biochem. 80, 943–971. doi:10.1146/annurev-biochem-062708-134043

Wu, N.C., Wilson, I.A., 2017. A Perspective on the Structural and Functional Constraints for Immune Evasion: Insights from Influenza Virus. Journal of Molecular Biology 429, 2694–2709. doi:10.1016/j.jmb.2017.06.015

Yan, L., Sun, S., Wang, W., Shi, J., Hu, X., Wang, S., Su, D., Rao, Z., Hu, J., Lou, Z., 2015. Structures of the yeast dynamin-like GTPase Sey1p provide insight into homotypic ER fusion. The Journal of Cell Biology 210, 961–972. doi:10.1083/jcb.201502078

Zhang, P., Hinshaw, J.E., 2001. Three-dimensional reconstruction of dynamin in the constricted state. Nat. Cell Biol. 3, 922–926. doi:10.1038/ncb1001-922

Zhao, J., Hedera, P., 2012. Hereditary spastic paraplegia-causing mutations in atlastin-1 interfere with BMPRII trafficking. Mol. Cell. Neurosci. doi:10.1016/j.mcn.2012.10.005

Zhao, X., Alvarado, D., Rainier, S., Lemons, R., Hedera, P., Weber, C.H., Tukel, T., Apak, M., Heiman-Patterson, T., Ming, L., Bui, M., Fink, J.K., 2001. Mutations in a newly identified GTPase gene cause autosomal dominant hereditary spastic paraplegia. Nat. Genet. 29, 326–331. doi:10.1038/ng758

Zhu, P.-P., Patterson, A., Lavoie, B., Stadler, J., Shoeb, M., Patel, R., Blackstone, C., 2003. Cellular localization, oligomerization, and membrane association of the hereditary spastic paraplegia 3A (SPG3A) protein atlastin. J. Biol. Chem. 278, 49063–49071. doi:10.1074/jbc.M306702200

Zhu, P.-P., Soderblom, C., Tao-Cheng, J.-H., Stadler, J., Blackstone, C., 2006. SPG3A protein atlastin-1 is enriched in growth cones and promotes axon elongation during neuronal development. Human Molecular Genetics 15, 1343–1353. doi:10.1093/hmg/ddl054

# CHAPTER 2

# TIMING AND RESET MECHANISM OF GTP HYDROLYSIS-DRIVEN CONFORMATIONAL CHANGES OF ATLASTIN‡

## ABSTRACT

The endoplasmic reticulum (ER) forms a branched, dynamic membrane tubule network that is vital for cellular function. Branching arises from membrane fusion facilitated by the GTPase atlastin (ATL). Many metazoan genomes encode for three ATL isoforms that appear to fulfill partially redundant function despite differences in their intrinsic GTPase activity and localization within the ER; however, the underlying mechanistic differences between the isoforms are poorly understood. Here, we identify discrete temporal steps in the catalytic cycle for the two most dissimilar isoforms, ATL1 and ATL3, revealing an overall conserved progression of molecular events from nucleotide binding and hydrolysis, to ATL dimerization and phosphate release. A crystal structure of ATL3 suggests a mechanism for the displacement of the catalytic $Mg^{2+}$ ion following GTP hydrolysis. Together, the data extend the mechanistic framework for how GTP hydrolysis drives conformational changes in ATL and how the cycle is reset for subsequent rounds of catalysis.

---

‡ The following sections are reproduced from O'Donnell, J.P., Cooley, R.B., Kelly, C.M., Miller, K., Andersen, O.S., Rusinova, R., Sondermann, H., 2017. Timing and Reset Mechanism of GTP Hydrolysis-Driven Conformational Changes of Atlastin. Structure 1–29. doi:10.1016/j.str.2017.05.007.

## INTRODUCTION

Atlastins (ATLs) are dynamin-related proteins (DRPs), which harness the energy of GTP hydrolysis for a wide range of cellular functions including vesicle scission, fusion and fission of organelles, cytokinesis, and antiviral activity **(Figure 2.1A and 2.2B)** (Rismanchi et al., 2008; Praefcke and McMahon, 2004). Common features of DRPs include a catalytic core comprising a conserved N-terminal large GTPase (or G) domain and a less conserved, helical stalk-like structural module **(Figure 2.1B)**. Beyond this core, DRPs can be distinguished by the presence of Pleckstrin homology or transmembrane domains for membrane association, and GTPase effector domains (GED). GEDs are part of the helical stalk that mediated DRP assembly and also contribute to the bundle signaling element that mediates nucleotide-dependent conformational changes. In the case of ATLs, the domain architecture includes a cytoplasmic G and stalk-like middle domains that are followed by an ER-specific transmembrane segment and a cytosolic, amphipathic C-terminal helix required for fusion (Hu et al., 2009; Liu et al., 2012; Faust et al., 2015; Praefcke and McMahon, 2004). However, ATLs lack a GED, which is consistent with an apparent absence of higher order membrane assembly and oligomerization-based concerted conformational changes, a hallmark of canonical DRPs (Gasper et al., 2009; Ghosh et al., 2006; Warnock et al., 1996).

Even within the ATL branch of the DRP superfamily, ATL isoforms have distinct features that warrant a closer mechanistic analysis. While fly genomes encode a single ATL protein (e.g. *Drosophila melanogaster* or dmATL), genomes of higher eukaryotes usually contain three ATL isoforms (ATL1-3), which in humans are 63-66% identical in

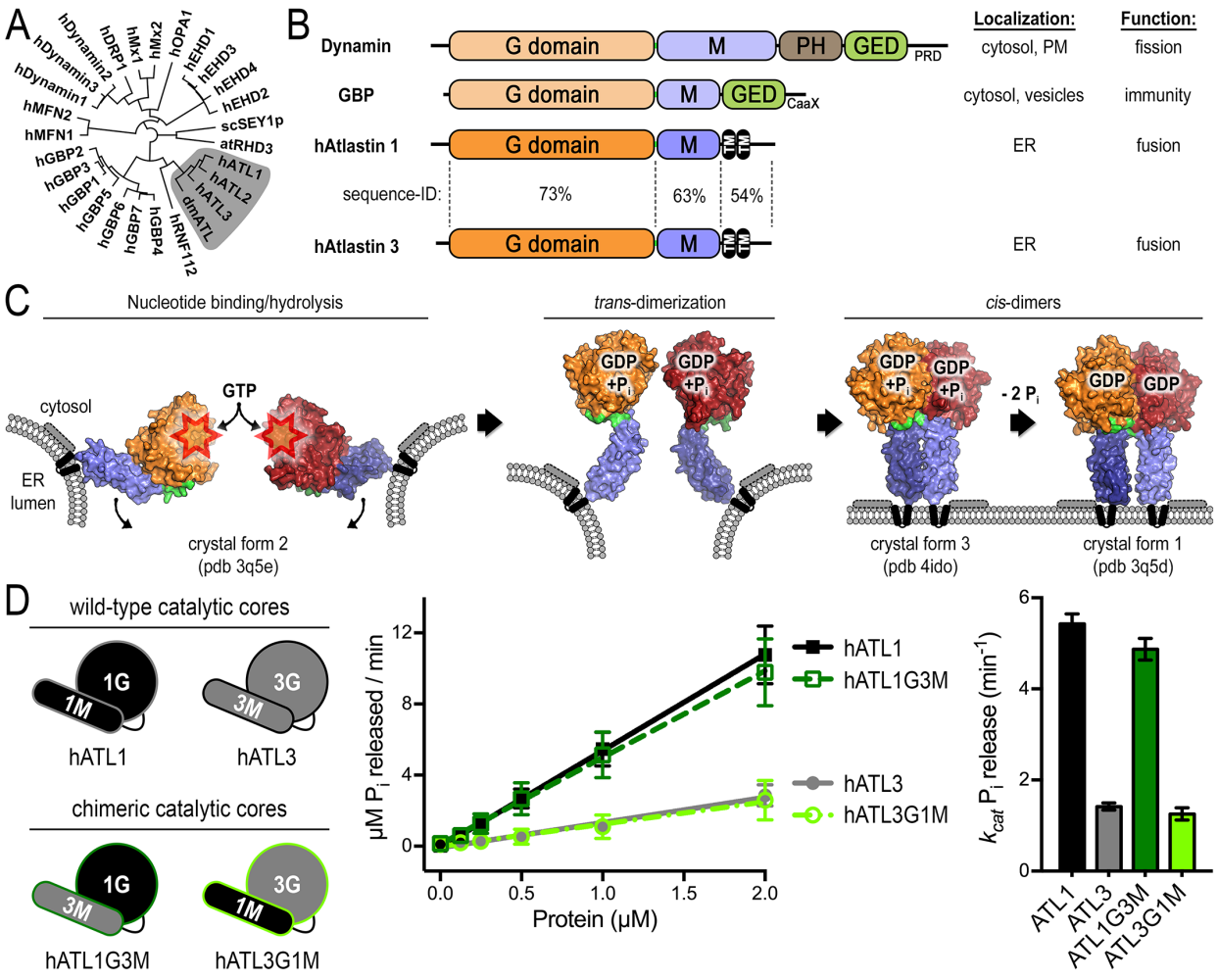


**Figure 2.1. ATL isoform-specific activities are encoded in their G domain. (A)** Phylogenetic tree of the DRP superfamily. **(B)** Domain architecture, localization, and function of prototypical DRP members and ATL isoforms. Sequence identity between ATL's functional domains is indicated. **(C)** Working model for ATL function. GTP binding and hydrolysis in monomeric ATL precedes homodimerization. The transmembrane and C-terminal helices are required for membrane fusion. Phosphate release appears to trigger a relaxation event within a dimer. Protein domains are color-coded (G domain: orange/red; middle domains: slate/dark blue). **(D)** Phosphate release kinetics and enzymatic turnover numbers ($k_{cat}$) of hATL1, hATL3, and chimeric proteins. Graphs showing means and standard error of the mean (SEM) are plotted from two biological replicates with three technical repeats each.

protein sequence. Tissues and cell lines typically express more than one isoform and vary in their relative expression pattern, with hATL1 being enriched in the brain and hATL2 and hATL3 exhibiting a broader tissue distribution (Rismanchi et al., 2008). Like other DRPs (Ferguson and De Camilli, 2012), ATLs have a unique sub-cellular localization and function. ATLs are resident to the tubular ER, where they catalyze membrane fusion to maintain ER morphology; proper control of this process is essential for axonal development, integrity, and signaling (Hu et al., 2009; Muriel et al., 2009; Orso et al., 2009; Rao et al., 2016; Renvoisé and Blackstone, 2010; Rismanchi et al., 2008; Yan et al., 2015; Li et al., 2017). Whereas hATL1 and hATL2 appear to be distributed throughout the tubular ER, hATL3 has a tendency to form puncta at tubule three-way junctions (Wang et al., 2016; Yan et al., 2015). hATL1 and hATL3 also localize to peripheral ER sheets and large sheet-like three-way junctions, and recently, super resolution microscopy techniques revealed that these structures are areas of dense tubular matrices (Nixon-Abell et al., 2016).

Integrity of the tubular ER requires ATL function because expression of dominant-negative ATL alleles, gene knockouts, and siRNA knock-downs disrupt the characteristic reticular ER morphology in exchange for unbranched and fragmented ER tubules (Hu et al., 2009; Rismanchi et al., 2008; Wang et al., 2016; Zhao et al., 2016). Functional redundancy has been shown for hATL1 and hATL2 due to their ability to restore a branched ER morphology when expressed in COS-7 cells devoid of all ATLs. However, hATL3 fails to fully rescue the branched ER phenotype suggesting that not all isoforms are mechanistically equivalent (Hu et al., 2015; Yan et al., 2015). Isoform differences have been shown biochemically through phosphate release kinetics, where hATL1 and

hATL3 have the highest and lowest catalytic rates (Hu et al., 2015). hATL1 and hATL3 are implicated in neurological disorders that are characterized by axonal degeneration, *i.e.* Hereditary Spastic Paraplegia and Hereditary Sensory Neuropathy (Fink, 2013; Fischer et al., 2014; Guelly et al., 2011; Hubner and Kurth, 2014). Additionally, hATL3 has been implicated in cancer due to its enrichment in the glioblastoma membrane proteome (Polisetty et al., 2012); its specific role in this context remains poorly characterized. Taken together, cellular and biochemical differences, as well as unique roles in disease pathogenesis, establish hATL1 and hATL3 as distinct isoforms, potentially fulfilling different cellular tasks. Yet, the molecular mechanisms underlying these cellular differences remain ill-defined.

Structural and biochemical studies have provided mechanistic insights into ATL-mediated membrane fusion, but the resulting models remain controversial due to ambiguities in the ordering of key steps through ATL's reaction cycle (Byrnes et al., 2013; Liu et al., 2015; McNew et al., 2013; Saini et al., 2014). Much of the controversy relating to the mechanism stems from the use of non-hydrolyzable GTP and transition state analogs, which for the basis of kinetic arguments elicit artificially slow transitions, which imposes limitations for interrogating physiologically relevant enzymatic reactions (Byrnes et al., 2013; Liu et al., 2015; Moss et al., 2011; Orso et al., 2009).

In the current study, we apply rapid, pre-steady state kinetic analyses of the GTP hydrolysis-driven reactions to: 1. evaluate the order of events in ATL's functional cycle and elucidate transient intermediates; and 2. compare hATL1 and hATL3 to determine mechanistic differences. These experiments bolster our previous model that involves an ATL protomer binding and hydrolyzing GTP, which enables subsequent

homodimerization of the G and middle domains *in trans* forming a tight tether between opposing membranes (Byrnes et al., 2013) **(Figure 2.1C)**. Here we rely on ATL's catalytic core fragment consisting of the G and middle domain, a module comprising 80% of the full-length protein that lacks the short transmembrane region and C-terminal amphipathic helix. Notably, the core fragment is an effective GTPase-dependent inhibitor of liposome fusion and ER formation in reconstituted *Xenopus* egg extracts (Moss et al., 2011; Wang et al., 2013; Wang et al., 2016), which argues that this core fragment is able to dimerize with full-length ATL during the latter's native reaction cycle. The catalytic core also has comparable GTPase activity to the full-length protein and is sufficient for nucleotide-dependent vesicle tethering when immobilized to $Ni^{2+}$-nitrilotriacetic acid (NTA) lipids via a C-terminal hexa-histidine tag (Liu et al., 2015; Moss et al., 2011; Wu et al. 2015). Hence, the catalytic core has proven to be a valuable proxy for understanding the full-length protein in regard to GTPase-driven steps of the reaction cycle.

We propose a novel mechanism for the recycling of the post-hydrolysis form of ATL with insight from a hATL3 crystal structure. Structural and biochemical data suggest a GDP•$Mg^{2+}$ release mechanism through the displacement of the nucleotide-coordinating $Mg^{2+}$ aided by the guanidinium moiety of an intramolecular arginine residue in the active site. Together, our comparative dissection of human ATL isoforms unveils both conserved and divergent characteristics governing ATL's fundamental molecular mechanism.

## RESULTS

*hATL1 and hATL3 have different catalytic efficiencies.*

Previously, catalytic activities were shown to be qualitatively different for human ATL isoforms (Hu et al., 2015), an observation we confirm and expand on here. First, we determined apparent turnover numbers ($k_{cat}$) for the catalytic core fragments of human ATL1 and ATL3, the most dissimilar isoforms in higher eukaryotes, by quantifying catalytic rates of phosphate release over a range of protein concentrations **(Figure 2.1D)**. By this analysis, hATL1 is approximately 4-fold faster than hATL3 ($k_{cat}$ values of 5.4 $min^{-1}$ and 1.3 $min^{-1}$ for hATL1 and hATL3, respectively) **(Figure 2.1D)**.

To identify the source of catalytic differences, we constructed chimeric proteins with swapped G domains, namely, a chimera comprised of hATI1's G and hATL3's middle domain (hATL1G3M) and vice versa (hATL3G1M) **(Figure 2.1D)**. Steady state phosphate release kinetics of these chimeras compared to the parent constructs, *i.e.* hATL1 and hATL3, indicated the protein's G domain as the sole determinant of catalytic rate ($k_{cat}$ values of 4.9 $min^{-1}$ and 1.3 $min^{-1}$ for hATL1G3M and hATL3G1M, respectively) **(Figure 2.1D)**. However, steady state phosphate release analysis fails to reveal the step(s) within the catalytic cycle that differ between the isoforms.

*hATL1 and hATL3 sample the same oligomeric states at equilibrium.*

The ability of ATL molecules to sample nucleotide-induced oligomeric states is crucial for their GTP hydrolysis-dependent membrane fusion activity (Bian et al., 2011; Byrnes et al., 2013; Liu et al., 2015; Orso et al., 2009; Wang et al., 2016). Static multi-angle light scattering (MALS) analysis depicts both isoforms to be monomeric in the

**Figure 2.2. Conserved nucleotide-dependent oligomerization of hATL1 and hATL3. (A)** SEC-MALS. Absolute molecular weights (colored data points across elution peaks) of hATL1 and hATL3 catalytic core fragments (injection: 2 mg/ml ± 1 mM nucleotide) were determined using SEC-MALS (90º-light scattering, black solid; refractive index signal, grey dotted; theoretical monomer and dimer molecular weights, grey dashed lines). **(B)** Equilibrium and steady state G domain dimerization. hATL1 and hATL3 were each labeled site-specifically with donor and acceptor fluorophores enabling FRET measurements in the absence and presence of the indicated nucleotides. Proteins (1 $\mu$M) and nucleotides (500 $\mu$M) were incubated until equilibrium or steady state was reached (duration was determined via a FRET time-course; see. **(C)** Equilibrium and steady state middle domain dimerization. Analogous FRET measurements were conducted with hATL1 and hATL3 labeled site-specifically at their middle domains. Relative FRET efficiencies were calculated as described in the Materials and Methods (****, p-values ≤ 0.0001; p-values ≥ 0.05, are defined as not significant [ns]). Graphs showing means and standard error of the mean are plotted from two biological replicates with three technical repeats each.

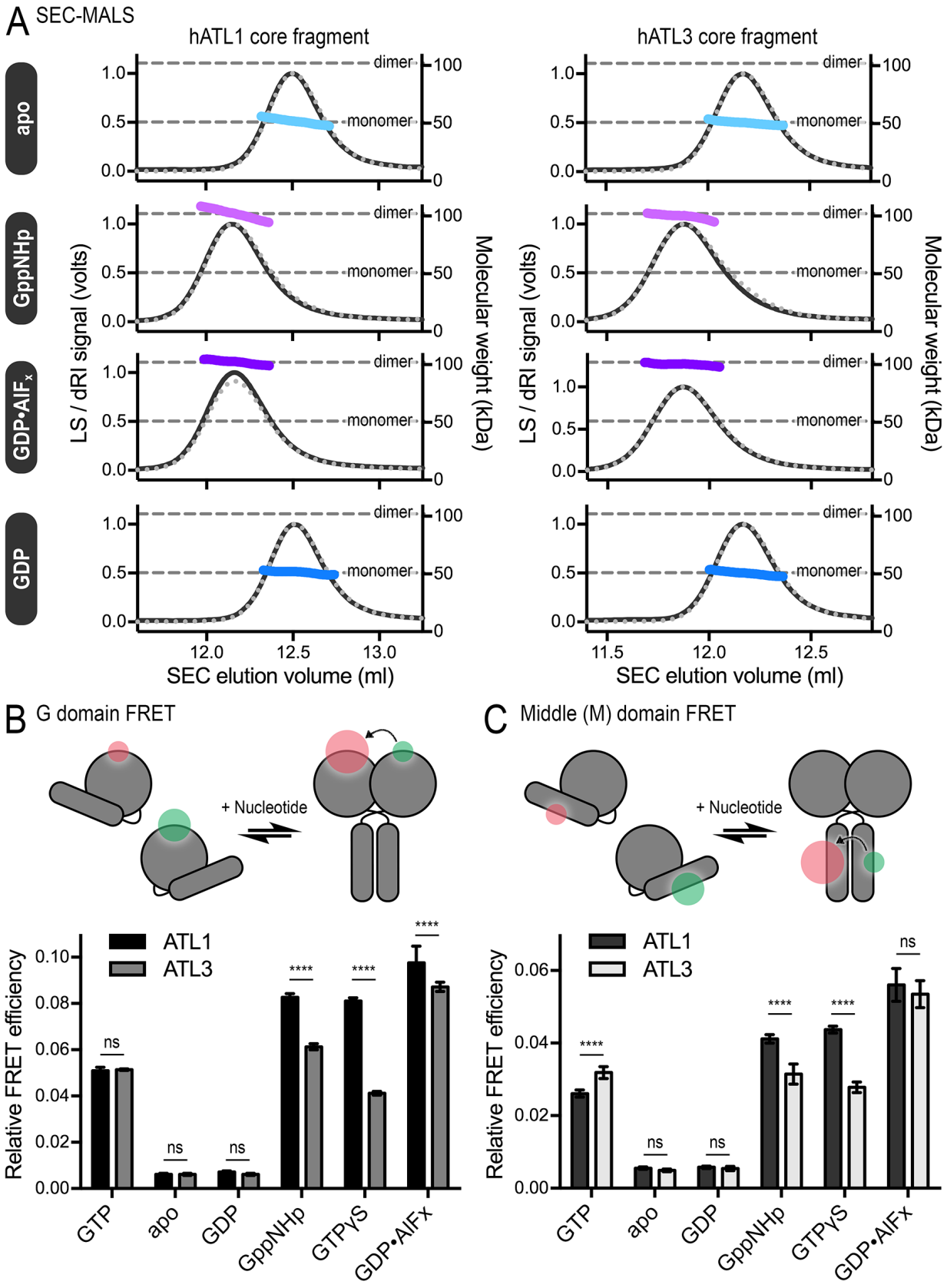
A SEC-MALS
hATL1 core fragment
hATL3 core fragment
apo
GppNHp
GDP•AlF$_x$
GDP
dimer
monomer
LS / dRI signal (volts)
Molecular weight (kDa)
SEC elution volume (ml)
B G domain FRET
C Middle (M) domain FRET
+ Nucleotide
Relative FRET efficiency
ATL1
ATL3
ns
****
GTP
apo
GDP
GppNHp
GTPγS
GDP•AlFx

nucleotide-free and GDP-bound states, whereas dimeric ATLs are found when bound to GppNHp and GDP•$AlF_x$, a non-hydrolyzable GTP analog and transition state analog, respectively **(Figure 2.2A)** (Byrnes et al., 2013).

MALS data yield absolute molecular weights for the atlastin oligomeric species in solution, but do not allow us to distinguish between the relative orientations of the two domains comprising the catalytic core fragment in these dimeric assemblies. To assess specific conformations at equilibrium or while actively hydrolyzing GTP we utilized a Förster Resonance Energy Transfer (FRET) strategy established previously for hATL1's catalytic core fragment (Byrnes et al., 2013) **(Figures 2.2B and 2.2C).** For this assay, we mutated surface-exposed cysteine residues in hATL1 and hATL3 to alanine, and introduced a single, surface-exposed cysteine residue in either the G or middle domain; all mutant proteins retained phosphate release activity comparable wild-type proteins **(Figure 2.3)**. Engineered cysteine residues were labeled with small organic fluorophores that serve as FRET-donor and -acceptor **(Figure 2.2B and 2.2C)**.

An initial time-course was performed to establish that equilibrium was reached at 60 minutes for non-hydrolyzable and transition state analogs. Dimerization that depends on GTP hydrolysis began to decrease at 10 minutes due to substrate consumption; thus, measurements were taken seconds after GTP addition (*data not shown*). Comparing the relative FRET efficiencies in a GTP-hydrolyzing system, both hATL1 and hATL3 sample the same distribution of G domain FRET states, but hATL3 middle domains exhibit more efficient fluorescence transfer compared to hATL1 **(Figures 2.2B and 2.2C)**. This indicates that both hATL1 and hATL3 adopt similar dimeric states in a GTPase-cycling system.

A

| | Intra-molecular FRET (iFRET) | G domain FRET (gFRET) | Middle domain FRET (mFRET) |
|---|---|---|---|
| hATL1 | **K$^{295}$C**/C$^{375}$A/**K$^{400}$C** | **K$^{295}$C**/C$^{375}$A | C$^{375}$A/**K$^{400}$C** |
| hATL3 | C$^{156}$A/**E$^{291}$C**/C$^{371}$A/ C$^{388}$A/**D$^{396}$C**/C$^{429}$A | C$^{156}$A/**E$^{291}$C**/C$^{371}$A/ C$^{388}$A/C$^{429}$A | C$^{156}$A/C$^{371}$A/C$^{388}$A/ **D$^{396}$C**/C$^{429}$A |

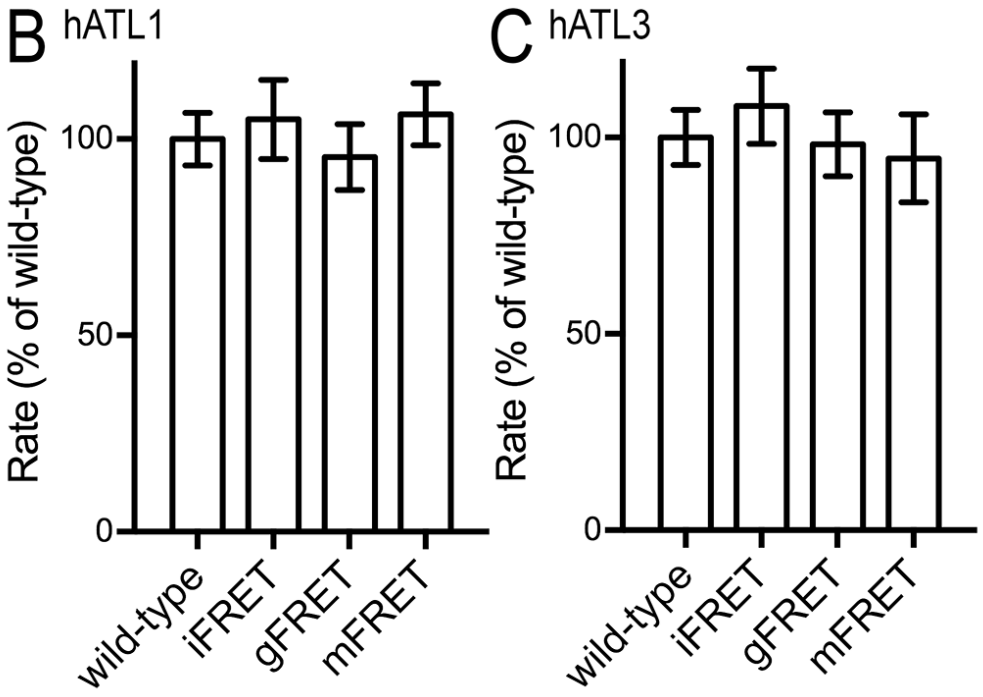


**Figure 2.3. hATL variants used as FRET reporters maintain wild-type-like enzyme activities. (A)** Table of the specific mutants introduced into the catalytic core fragment of hATL1 and hATL3 to ensure specific, single-site labeling. **(B)** Enzyme kinetics based on phosphate release for mutant proteins listed in (A). Graphs showing means and standard error of the mean (SEM) are plotted from a minimum of two biological replicates with three technical repeats each.

The relative equilibrium FRET efficiency for G domains was less for hATL3 in the presence of non-hydrolyzable GTP analogs, GppNHp and GTPγS, compared to hATL1. Though the difference observed with the transition state analog GDP•$AlF_x$ was statistically significant, the effect was less pronounced when compared to corresponding measurements with non-hydrolyzable nucleotides **(Figure 2.2B)**. The same trend was observed comparing middle domain FRET with the non-hydrolyzable

GTP analogs, while the values obtained with the transition state analog were not statistically different **(Figure 2.2C)**. For both isoforms, GDP•$AlF_x$ had a larger relative FRET efficiency than non-hydrolyzable GTP analogs, similar to earlier reports for dmATL **(Figures 2.2B and 2.2C)** (Liu et al., 2015). In summary, we conclude that at equilibrium and in an actively cycling system, hATL1 and hATL3 sample the same oligomeric states but populate different distributions. Higher FRET efficiencies for GDP•$AlF_x$ suggest the transition state represents the tight, high-affinity conformation in both isoforms.

*Sequence of GTP hydrolysis-driven conformational changes in human ATL isoforms.*

Isoform specific conformational and catalytic differences prompted us to define the timing of key steps in the GTP hydrolysis cycle. By assaying the pre-steady state regime, we elucidated the timing of GTP-loading, FRET-based conformational changes, and phosphate release. The use of equivalent experimental conditions enabled direct comparison of kinetic events.

The initial rates of nucleotide binding to ATL were determined with 2'-(or-3')-O-(N-Methylanthraniloyl) (mant)-nucleotides (i.e. mant-GTP and mant-GDP). These nucleotides are conjugated with an environmentally sensitive fluorophore that increases in quantum yield upon protein binding **(Figure 2.4A, top)**. With substrate at a 500-fold molar excess over protein, we observed near immediate mant-GTP and mant-GDP binding to hATL1 with rate constants of 169.1 ± 1.4 $sec^{-1}$ and 524.9 ± 11.5 $sec^{-1}$, respectively **(Figure 2.4A, middle),** consistent with our earlier report (Byrnes et al., 2013). The rate of nucleotide binding to hATL3 was slower than for hATL1, with

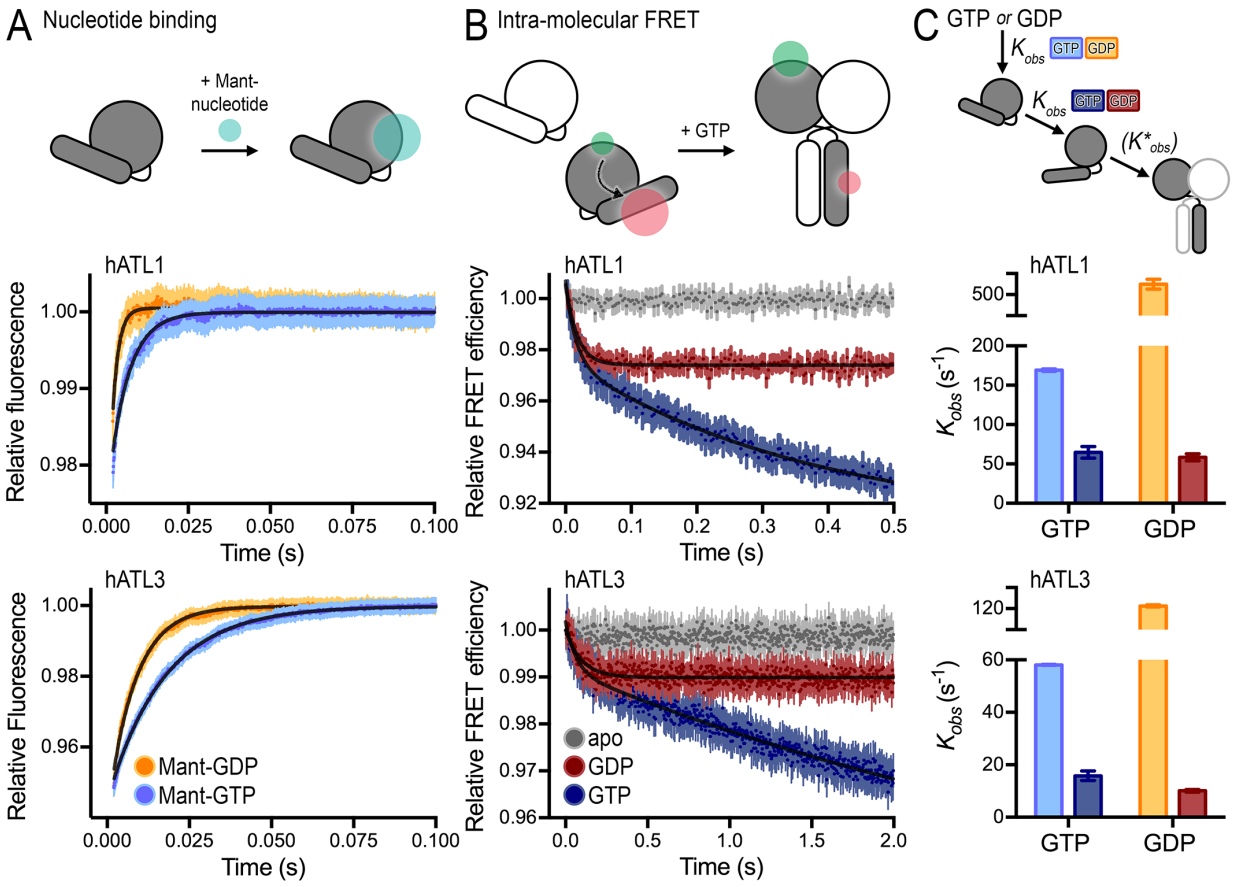


**Figure 2.4. Differences in nucleotide binding and intramolecular conformational changes in hATL1 and hATL3. (A)** Nucleotide-loading rates. Mant-conjugated nucleotide (500 $\mu$M) binding to hATL catalytic core isoforms (1 $\mu$M) was determined by stopped-flow kinetics. Graphs showing means and SEM are plotted from a minimum of two biological replicates with five technical repeats each. **(B)** Intramolecular FRET. hATL1 and hATL3 were labeled site-specifically at cysteine residues in their G and middle domains. Pre-steady state kinetics of nucleotide-induced conformational changes were determined. Graphs showing means and SEM are plotted from a minimum of two biological replicates with eight technical repeats each. **(C)** Rates determined based on the experiments shown in (A) and (B). The second, slower phase observed with GTP is not plotted ($hATL1^{slow}$ = 2.6 $sec^{-1}$; $hATL3^{slow}$ = 0.24 $sec^{-1}$).

observed rate constants for mant-GTP and mant-GDP of 58.1 ± 0.1 $sec^{-1}$ and 121.3 ± 0.5 $sec^{-1}$, respectively **(Figure 2.4A, bottom)**. The differences in nucleotide binding rates define the first major mechanistic difference between hATL1 and hATL3 catalytic cycles.

Relatively few studies have focused on the molecular events prior to ATL homodimerization (Byrnes et al., 2013; Liu et al., 2015). To investigate conformational changes within ATL protomers, we developed an intramolecular FRET sensor to measure distance changes between the G and middle domains. A single protomer is labeled at the sites used for the G and middle domain dimerization FRET, residues that are 60Å or 70Å apart in distinct crystallographic states of hATL1 (**Figure 2.4B, top**) (Byrnes et al., 2011). The role of this sensor was to measure conformational changes that occur within the monomer. The experiment uses a 1:10 molar ratio of labeled to unlabeled protein to minimize FRET signal contributions across the G and middle domain dimer interfaces.

When either hATL1 or hATL3 bound GTP, there was a rapid loss of FRET signal indicating a distance increase between the G and middle domain, followed by a slow phase of FRET signal increase. The rapid, initial conformational change was also present when we used GDP, GTPγS, or GppNHp, and with a catalytically defective ATL in the presence of GTP **(Figure 2.4B and Figures 2.5A-2.5C)**. In contrast, the slower second phase was an exclusive feature of GTP plus an active enzyme **(Figure 2.4B)**. The FRET data for GTP and GDP were fit by a double and single exponential decay, respectively; only the fast rate constant for GTP is reported for comparison. Intramolecular conformational changes in hATL1 proceeded with a rate constant for

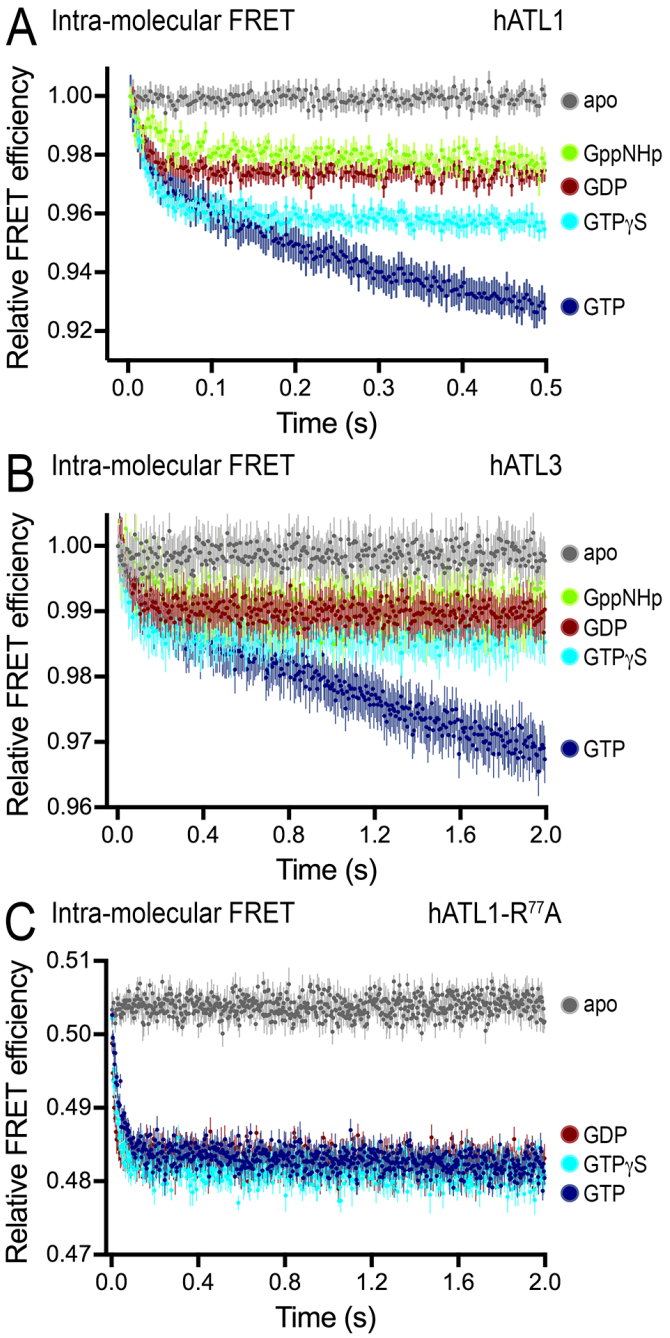


**Figure 2.5. Effect of nucleotide analogs on intra- molecular FRET in hATL1. (A)**, hATL3 **(B)**, and hATL1-R77A **(C)**. Analogous experiments were carried out with non-hyrdolyzable analogs GppNHp and GTPγS. Graphs showing means and standard error of the mean (SEM) are plotted from a minimum of two biological replicates with eight technical repeats each.

GTP and GDP of 64.7 ± 7.4 $sec^{-1}$ and 58.5 ± 4.6 $sec^{-1}$; the corresponding values for hATL3 were 15.8 ± 1.8 $sec^{-1}$ and 10.1 ± 0.5 $sec^{-1}$ **(Figure 2.4B, middle/bottom)**. This conformational change within a protomer was markedly slower than nucleotide binding, and the rates for the conformational change were similar for both GTP and GDP, in contrast to the rates for nucleotide association. This suggested that the conformational change was a distinct step after nucleotide binding for both hATL1 and hATL3 **(Figure 2.4C)**. Furthermore, the additional slow phase observed in the presence of GTP and, presumably GTP hydrolysis, occurred at a rate comparable to the dimerization steps described below. This phase was most likely due to dimerization of the FRET reporter protein with an unlabeled protein, which acted to fully extend the distances between the G and middle domains**.**

The mant-nucleotide and intramolecular-FRET experiments revealed a distance increase between the G and middle domains following nucleotide binding. These events occurred in rapid succession with no observable delay, indicating there was no accumulation of intermediate species. Next, we revisited homodimerization events between the G and middle domains independently, using a stopped-flow with shorter dead-time and a red-shifted photomultiplier tube to enable higher sensitivity in data collection (Byrnes et al., 2013; Ingólfsson and Andersen, 2010) **(Figure 2.6A, top)**. These technical improvements enabled two important mechanistic signatures to be interpreted from the G and middle domain FRET traces driven by GTP hydrolysis: first, both hATL1 and hATL3 displayed a lag-phase prior to their exponential growth; second, comparing this delay between the G and middle domains indicated sequential steps, with the G domain dimerization occurring before the middle domain dimerization

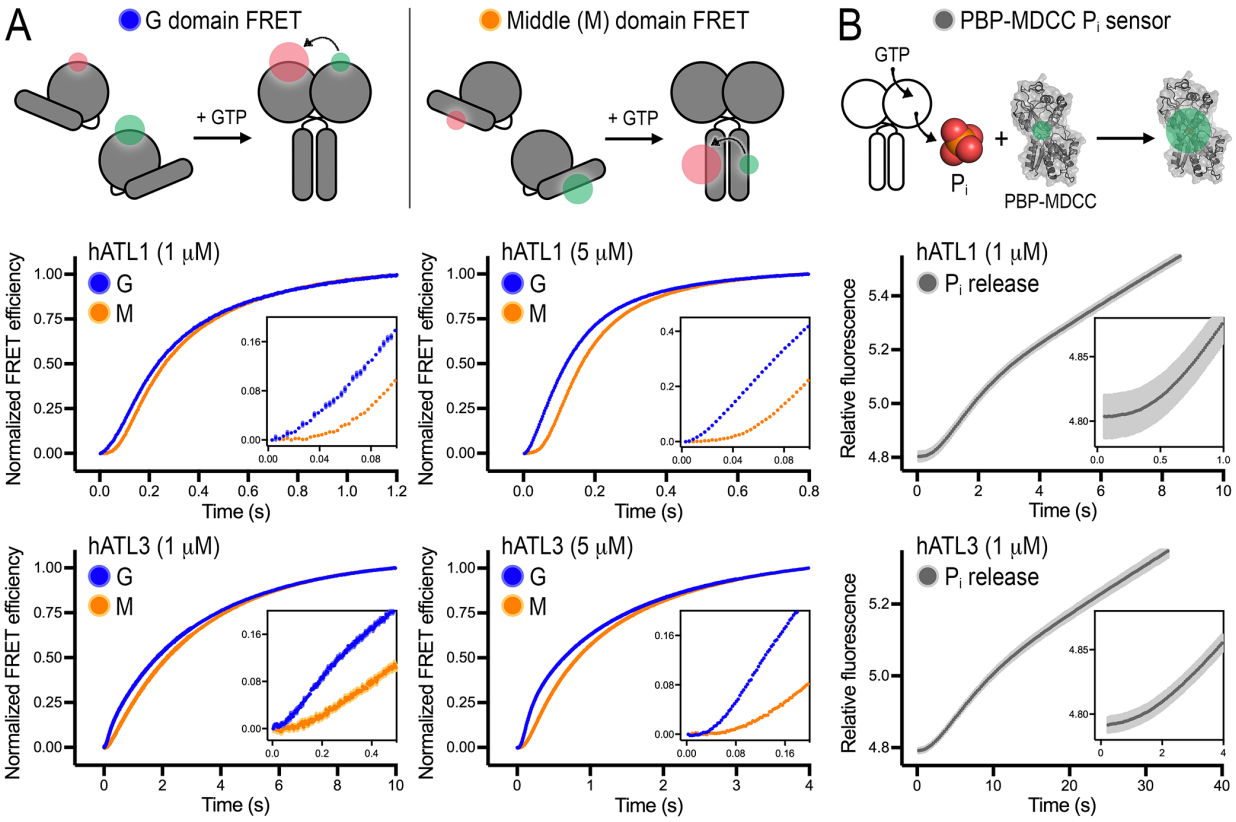


**Figure 2.6. Pre-steady state kinetics reveals delays between hATL G and middle domain dimerization, and phosphate release. (A)** G and middle domain FRET. For both ATL isoforms, the timing of G and middle domain dimerization as a function of GTP hydrolysis was determined using the FRET reporters introduced in Figure 2.2. Two protein concentrations were used (1 $\mu$M, left graphs; 5 $\mu$M, right graphs). Insets show a zoom-in view of the early time points. **(B)** Phosphate release kinetics. Phosphate release was determined by measuring the change in PBP-MDCC sensor signal upon binding of inorganic phosphate. Insets show a zoom-in view of the early time points. Graphs showing means and SEM are plotted from a minimum of two biological replicates with eight technical repeats each.

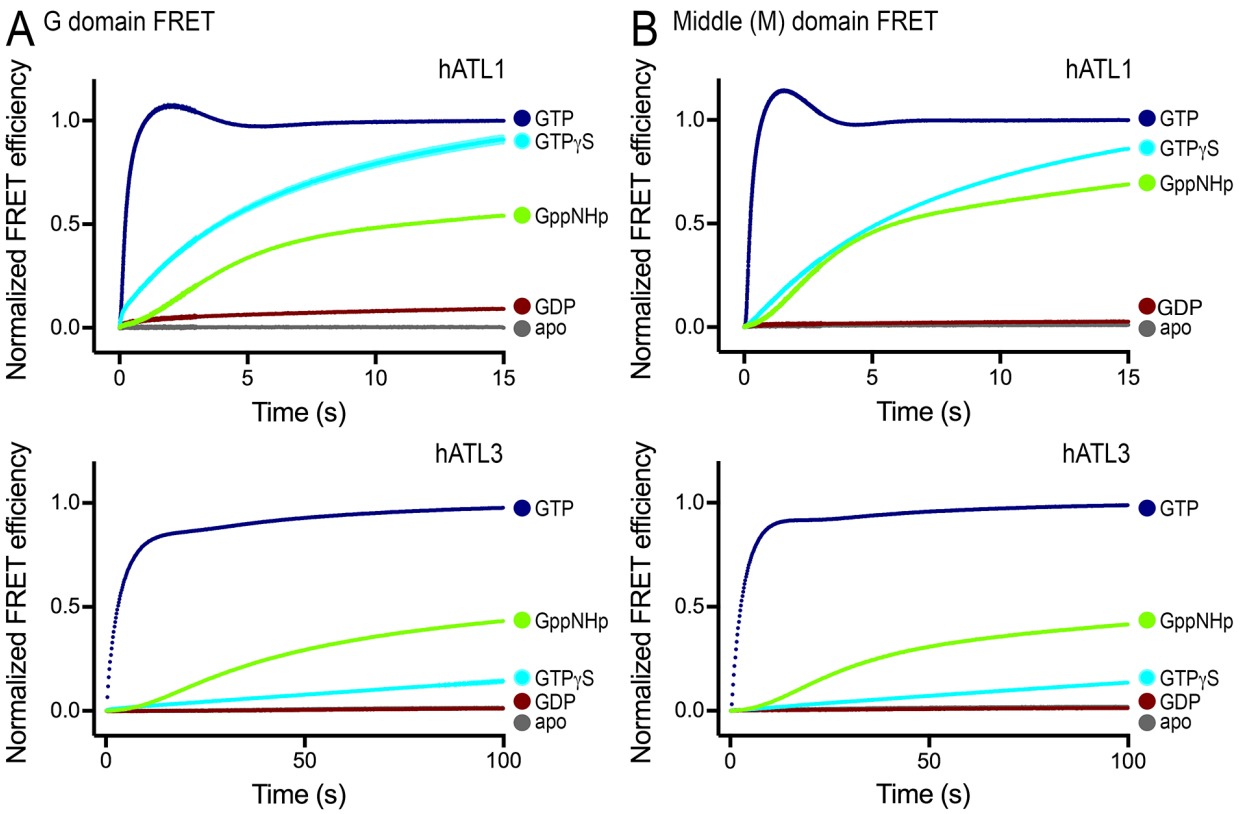


**Figure 2.7. Long time scale G and middle-domain dimerization.** G **(A)** and middle **(B)** domain FRET time courses with hydrolyzable and non-hydrolyzable nucleotides. Data shown for GTP are identical to those displayed in Figure 4, albeit at a shorter timespan. Analogous experiments were carried out with non-hyrdolyzable analogs GppNHp and GTPγS, GDP and the apo-state.

**(Figure 2.6A, left)**. Increasing the concentration of protein by a factor of five increased both dimerization rates, however the difference between the G and middle domain lag-phases became more pronounced **(Figure 2.6A, right)**. These results suggest that dimerization, as a physical step, is rate-limiting in this sequence.

Thus far, timing experiments have revealed that nucleotide loading and a conformational change within the protomer preceded sequential homodimerization of the G and middle domains. These steps required GTP hydrolysis to be initiated in the protomer because GTP binding alone was not sufficient for rapid G and middle domain

dimerization **(Figures 2.7A-2.7B)**. The longest of the lag-phases for these steps was dimerization of the middle domains, which initiated exponential growth at 170 and 380 ms for hATL1 and hATL3 (at 1 μM total protein), respectively. In summary and consistent with our previous studies using CFP/YFP-based hATL1 sensors (Byrnes et al., 2013), hATL1 and hATL3 G domain dimerization appears to occur after hydrolysis has been initiated, and G domain dimerization is required for middle domain dimerization. We refer to initiation of nucleotide hydrolysis because we cannot distinguish between G domain dimerization being driven by the transition state, consistent with it being the tightest state at equilibrium **(Figure 2.2B)**, or by the post-hydrolysis state (i.e. GDP+$P_i$). Additional evidence supporting our conclusion that G domain dimerization cannot be driven by GTP binding alone include the slow kinetics observed with non-hydrolyzable GTP analogs (i.e. GppNHp and GTPγS) and hydrolysis-deficient hATL1 binding GTP **(Figures 2.5 and 2.7)** (Byrnes et al., 2013). With prolonged equilibration, G and middle domain dimerization will occur under these experimental conditions, though due to the timescales, these transitions are most likely not physiologically pertinent **(Figure 2.7)** (Byrnes et al., 2013).

Lastly, we investigated the timing of phosphate release relative to the previously described events. We used a coumarin-labeled PstS phosphate binding protein (PBP-MDCC) that increases quantum yield upon binding inorganic phosphate **(Figure 2.6B top)** (Brune et al., 1994). For these experiments, 10 μM PBP-MDCC was included in the reaction to track phosphate release produced by ATL over time. Similar to G and middle domain FRET traces, a substantial lag-phase was present with a duration of 1.5 and 6.4 sec for hATL1 and hATL3, respectively **(Figure 2.6B)**. This phase reflected the

accumulation of intermediates in the steps measured previously and indicated that homodimerization preceded phosphate release. This lag phase was followed by a classical pre-steady state burst and the steady state accumulation of phosphate. As in the cases of the previous steps, both hATLs shared the same kinetic signatures of phosphate release, but completed their transitions between states at different time-scales**.**

To determine the timing of GTP hydrolysis relative to the prior events, we used quench-flow (for sub-second/pre-steady-state reaction rates) and standard quenching (for the seconds-to-minutes/steady-state time scale) approaches. Quantification of phosphate in the denatured and neutralized samples was done with the phosphate sensor PBP-MDCC. Pre-steady state kinetics showed an almost instantaneous rise in phosphate production with reactions rates ($k_{obs}$) of 27.2 $sec^{-1}$ and 12.9 $sec^{-1}$ for hALT1 and hATL3, respectively **(Figure 2.8A)**. There is no further phosphate production (GTP hydrolysis) during the next few 100 ms **(Figure 2.8A)**, but phosphate production increases linearly at longer time scales when steady state is reached **(Figure 2.8B)** and corresponds to phosphate release in non-quenched experiments **(Figure 2.8B)**. Together, these results indicate that initial GTP hydrolysis occurs with rate constants similar to the conformational changes observed by intramolecular FRET **(Figures 2.4B 2.4C)**.

*Dimerization is a prerequisite for phosphate release.*

Our timing studies indicated that phosphate release occurred much later than any other step in the reaction mechanism. Therefore, we hypothesized that dimerization

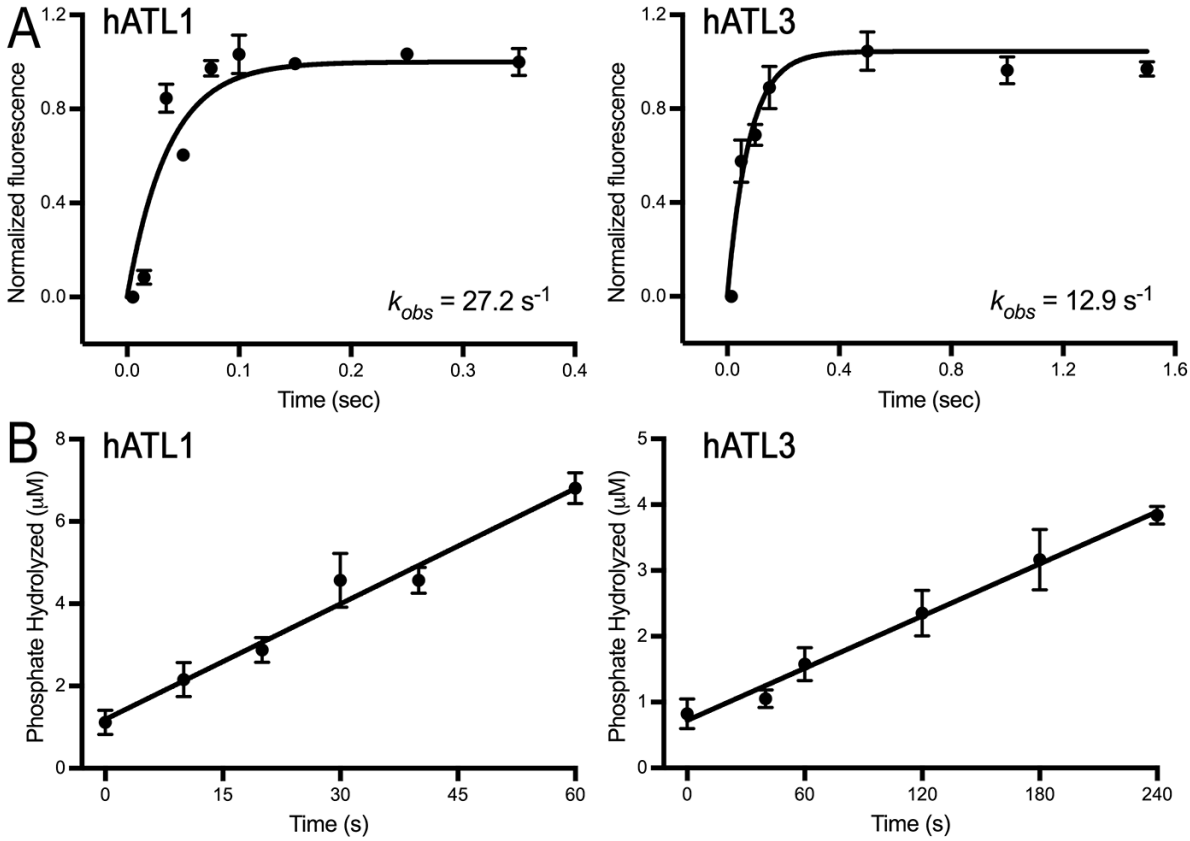


**Figure 2.8. GTP-hydrolysis kinetics measured by quench techniques.** Quench-flow **(A)** and bench-top quenching **(B)** establishes pre-steady-state and steady-state GTP hydrolysis timing. Hydrolyzed phosphate bound to the protein and free in solution was detected after quenching and neutralization of the reaction (1 µM ATL and 500 µM GTP) using the phosphate sensor PBP•MDCC (5 µM). Quench-flow data for hATL1 represent 3 technical replicates. Quench-flow data for hATL3 represent two biological replicates with 3 and 8 technical replicates. Bench-top quenching data comprise 3 technical replicates. Graphs show the mean and standard error of the mean (SEM).

is a prerequisite for phosphate release. The sensitivity of PBP•MDCC enabled us to measure ATL mediated phosphate release at nanomolar concentrations of protein. At concentrations above 250 nM, activity scales linearly **(Figure 2.1D)**, however, lower concentrations of enzyme resulted in phosphate release activity being reduced nonlinearly **(Figure 2.9A)**. At each enzyme concentration tested, a $k_{cat}$ value was calculated and plotted as a function of enzyme concentration. If $k_{cat}$ was independent of enzyme concentration, we would expect a constant relation, but if $k_{cat}$ changed with

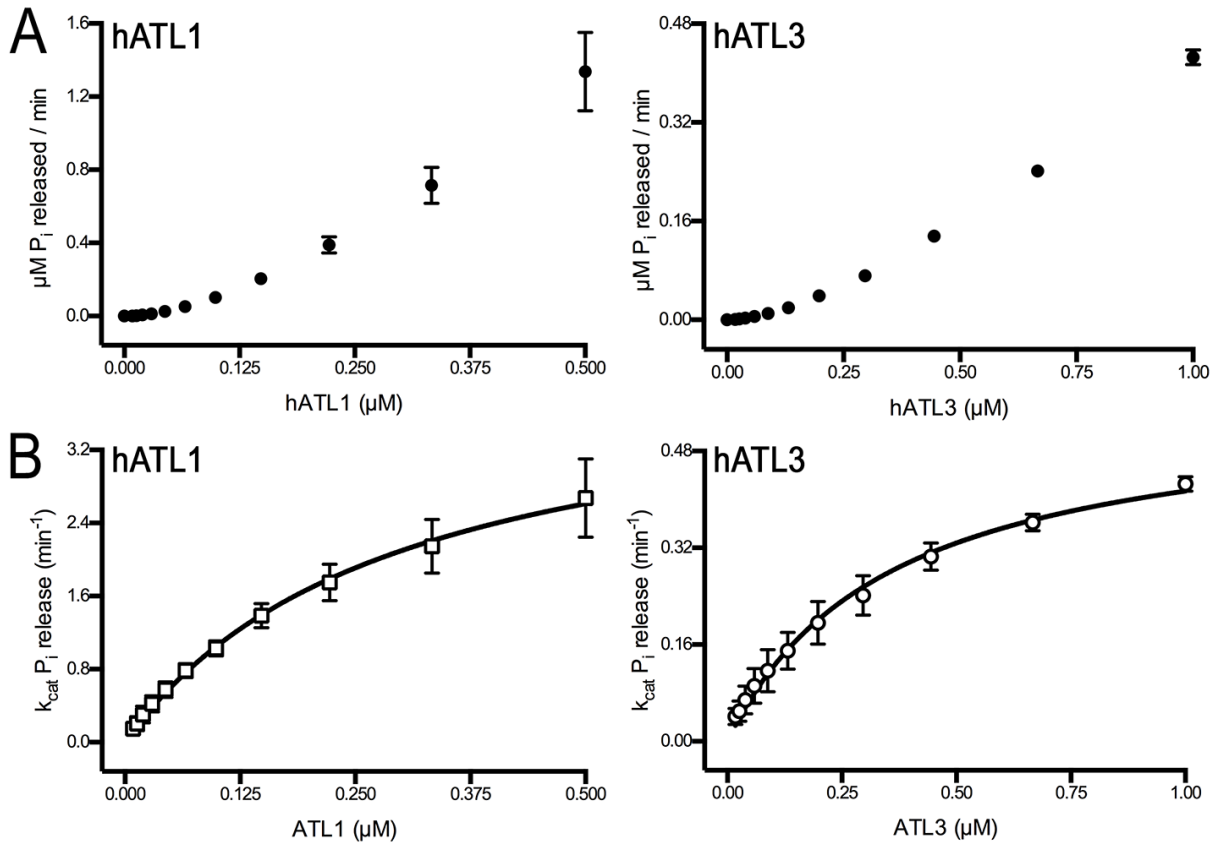


**Figure 2.9. Cooperativity of phosphate release indicates a requirement of ATL dimerization for full catalytic activity. (A)** Phosphate release kinetics as a function of enzyme concentration are plotted for the catalytic core fragments of hATL1 and hATL3. **(B)** $k_{cat}$ depends on enzyme concentration. Data were fit to a binding-saturation model to determine activity-derived dimer dissociation constants for hATL1 and hATL3 (300 and 330 nM, respectively). Note that fitting the data results in maximal $k_{cat}$ values for hATL1 and hATL3 of 4.2 and 0.6 $min^{-1}$, respectively. The differences between these results and the data in Figure 1D are likely due to the use of different assays and differences in range of enzyme concentrations used. Also, we included BSA (50 $\mu$M) in the reaction buffer to stabilize enzymes at low protein concentrations (Kunzelmann et al., 2005), and molecular crowding may contribute to the apparent lower catalysis rates reported here (Aumiller et al., 2014). Graphs showing means and standard deviation of the mean (SD) are plotted from of two biological replicates with 3 technical repeats each.

enzyme concentration, one can postulate that phosphate release is enhanced by ATL dimerization (Kunzelmann et al., 2005), either directly or indirectly. For hATL1 and hATL3, $k_{cat}$ depended on enzyme concentrations and the dependency was most apparent in the low nanomolar regime **(Figure 2.9B)**. These curves were fit to a saturation-binding model to determine an activity-derived dimerization $K_d$ as described in the Materials and Methods. The $K_d$ values obtained for hATL1 and hATL3 were 300 nM ± 30 and 350 nM ± 30, respectively.

*The crystal structure of hATL3 reveals a mechanism for post-hydrolysis regulation.*

We determined the crystal structure of the catalytic core fragment of hATL3 comprising G and middle domains (residues 21-442). The structure was solved at 2.1 Å in space group C2 with 2 molecules in the asymmetric unit **(Table 2.1 and Figure 2.10A)**. The protein is bound to GDP despite being crystalized in the presence of GTPγS and $Mg^{2+}$. Globally, the hATL3 structure resembles earlier structures of hATL1 and dmATL bound to GDP•$Mg^{2+}$ where the G and middle domains are engaged and individual protomers are forming a weak dimer interface between G domains (interface surface area = 780 $Å^2$, $\Delta^iG$ = -5.9 kcal/mol (Krissinel and Henrick, 2007)) **(Figure 2.10A)** (Bian et al., 2011; Byrnes and Sondermann, 2011; Wu et al., 2015). One of the hallmarks of this functional state, a central helix, α4, that is bent as a result of the G-middle domain docking, is also preserved in hATL3 **(Figure 2.10B)**.

The hATL3 structure revealed a novel active site organization: whereas hATL1 (PDB 3Q5E), dmATL (PDB 3X1D), and Sey1 (PDB 5CA8) exhibit the same binding configuration for GDP•$Mg^{2+}$ (Byrnes and Sondermann, 2011; Wu et al., 2015; Yan et al.,

| Table 2.1: X-ray data collection and refinement statistics. | |
|---|---|
| | hATL3•GDP (Residues 21-442) |
| **Data Collection** | |
| X-ray source | CHESS |
| Wavelength | 0.6362 |
| Space group | C 1 2 1 |
| Unit cell | |
| a, b, c (Å) | 130.7, 57.1, 143.4 |
| α, β, γ (°) | 90, 116.2, 90 |
| Resolution (Å)[a] | 29.03 - 2.096 (2.171 - 2.096) |
| Number of Reflections | |
| Total | 251811 (17778) |
| Unique | 55378 (4912) |
| Completeness (%) | 98.41 (88.17) |
| Multiplicity | 4.5 (3.6) |
| I/σ(I) | 12.43 (1.14) |
| Rmeas (%) | 10.8 |
| Rmerge (%) | 9.5 |
| $R_{pim}$ (%) | 5 |
| CC1/2 | 0.992 (0.36) |
| CC* | 0.998 (0.728) |
| **Refinement** | |
| Rwork / Rfree (%) | 19.7 / 22.5 |
| rms deviations | |
| Bond length (Å) | 0.012 |
| Bond angles (°) | 1.24 |
| No. of atoms | |
| Protein | 5975 |
| Ligands | 56 |
| Water | 239 |
| Ave. B-factors (Å$^2$) | |
| Protein (total) | 57.9 |
| Protein (chain A) | 48 |
| Protein (chain B) | 69.4 |
| Ligands | 41.4 |
| Water | 52.1 |
| Ramachandran (%) | |
| Favored | 97.3 |
| Outliers | 0 |

(a) Values in brackets are fore the highest resolution bin.

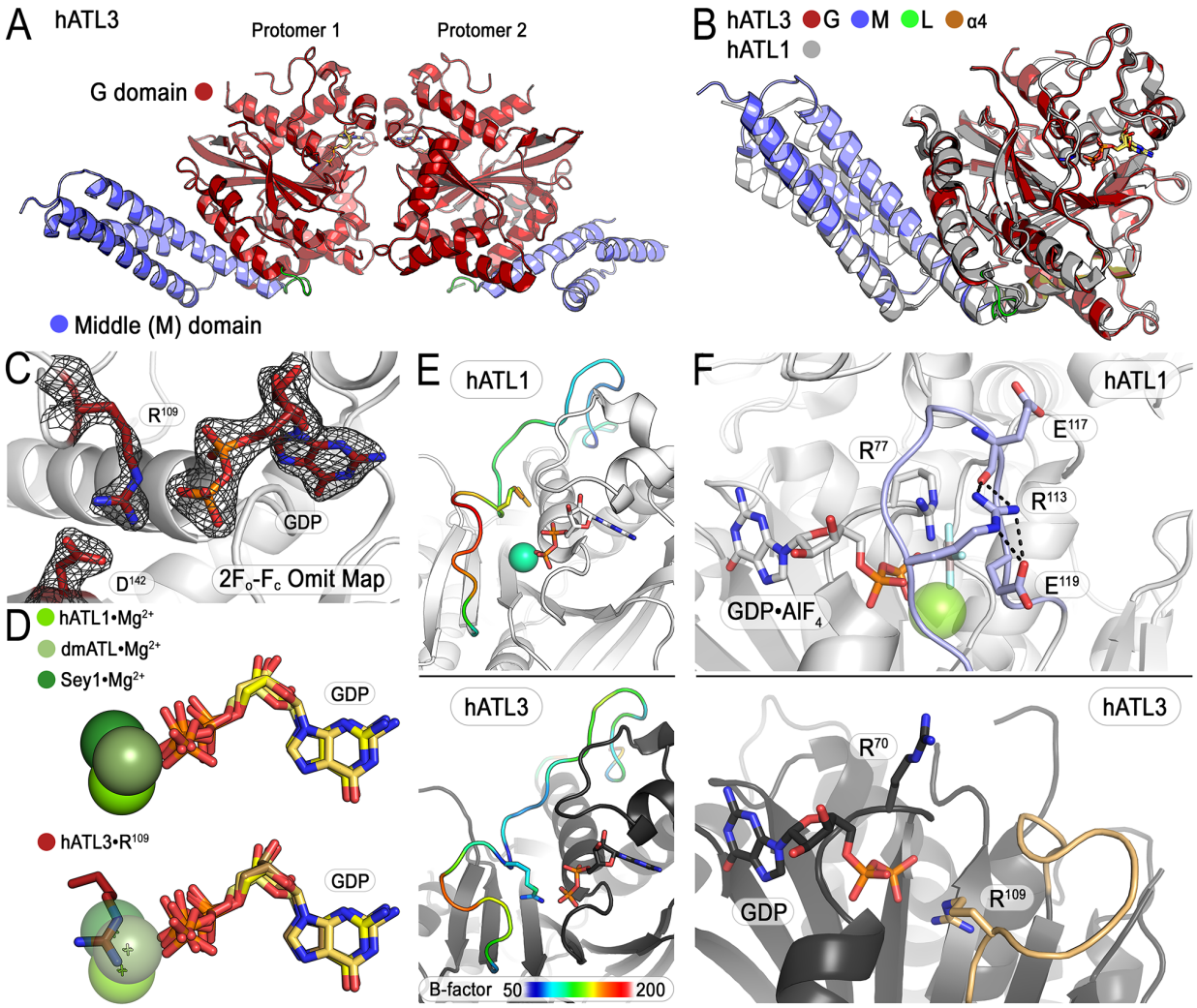


**Figure 2.10. The structure of hATL3's catalytic core fragment depicts a novel active site conformation. (A)** Asymmetric unit depicts a weak dimer interface between G domains (red) while middle domains (slate) are engaged with their respective G domains. **(B)** Alignment of hATL3 and hATL1 (PDB 3Q5E) structures using their G domains as a reference. Color code: hATL3 G domain (red), middle domain (slate), G-middle domain linker (green), and α4 (tan). **(C)** $R^{109}$ in the active site of hATL3 occupies the canonical $Mg^{2+}$ binding site and makes an intramolecular salt-bridge with $D^{142}$. A $2F_0$-$F_C$ omit map was calculated and contoured to 1.25 σ for GDP, $R^{109}$, and $D^{142}$. **(D)** GDP•$Mg^{2+}$ alignments for hATL1, dmATL, and Sey1 depicted a conserved binding organization (top). $R^{109}$ of hATL3 was superimposed to illustrate the spatial relation to the $Mg^{2+}$ binding site (bottom). **(E)** Temperature factor analysis for loops containing the $R^{113}$ and $R^{109}$ in hATL1 and hATL3, respectively. **(F)** A second role for the $R^{113}$ in stabilizing G2/switch I in the transition state structure of hATL1 (PDB 4IDO) by forming hydrogen bonds with the carbonyl of residue $E^{117}$ and the side chain of $E^{119}$ (light blue), is illustrated, compared to the open configuration of G2/switch I in hATL3 with $R^{109}$ occupying the canonical $Mg^{2+}$ binding site (light orange).

2015), the canonical $Mg^{2+}$ was displaced by the guanidinium group of an intramolecular arginine residue at position 109 ($R^{109}$) in the hATL3 structure **(Figures 2.10C and 2.10D)**, an active site residue that is distinct from the catalytic arginine finger ($R^{70}$ in hATL3, $R^{77}$ in hATL1). The conformation of $R^{109}$ is further stabilized through a salt-bridge formed with an aspartate residue at position 142, one of the main $Mg^{2+}$-coordinating residues in ATLs **(Figure 2.10C)** (Bian et al., 2011; Byrnes and Sondermann, 2011). hATL1 and hATL3 B-factors for the loop containing the active site arginine indicated that this region was more flexible in the hATL1 structure **(Figure 2.10E).** Location of the $Mg^{2+}$-displacing arginine in the transition state structure of hATL1 (PDB 4IDO) suggested a secondary role in stabilizing G2/switch I and capping the nucleotide; this was contrasted with the open state of G2/switch I for hATL3 **(Figure 2.10F)**. Despite being crystallized with GTPγS•$Mg^{2+}$, the solved structure displayed a GDP•$R^{109}$ in the active site, which may be due to hATL3 slowly hydrolyzing GTPγS or the presence of the GDP contamination in GTPγS (up to 12% according to the manufacturer; Sigma-Aldrich, St. Louis, MO). Independent of the origin of the crystallographic state, we hypothesized that the active site architecture depicts a post-hydrolysis conformation resembling a $Mg^{2+}$ removal mechanism with analogies to mechanisms described for nucleotide exchange factors (Bos et al., 2007).

To validate this novel structural insight and probe the functional role for $R^{109}$ for ATL's GTPase cycle, we mutated the residue to an alanine in the catalytic core fragment of both hATL1 and hATL3 and tested their activities. The $R^{109}$A and $R^{113}$A mutation in hATL3 and hATL1, respectively, reduced steady state activity of the enzymes to ~40% of their corresponding wild-type parent **(Figures 2.11A and 2.11B)**. An initial indication

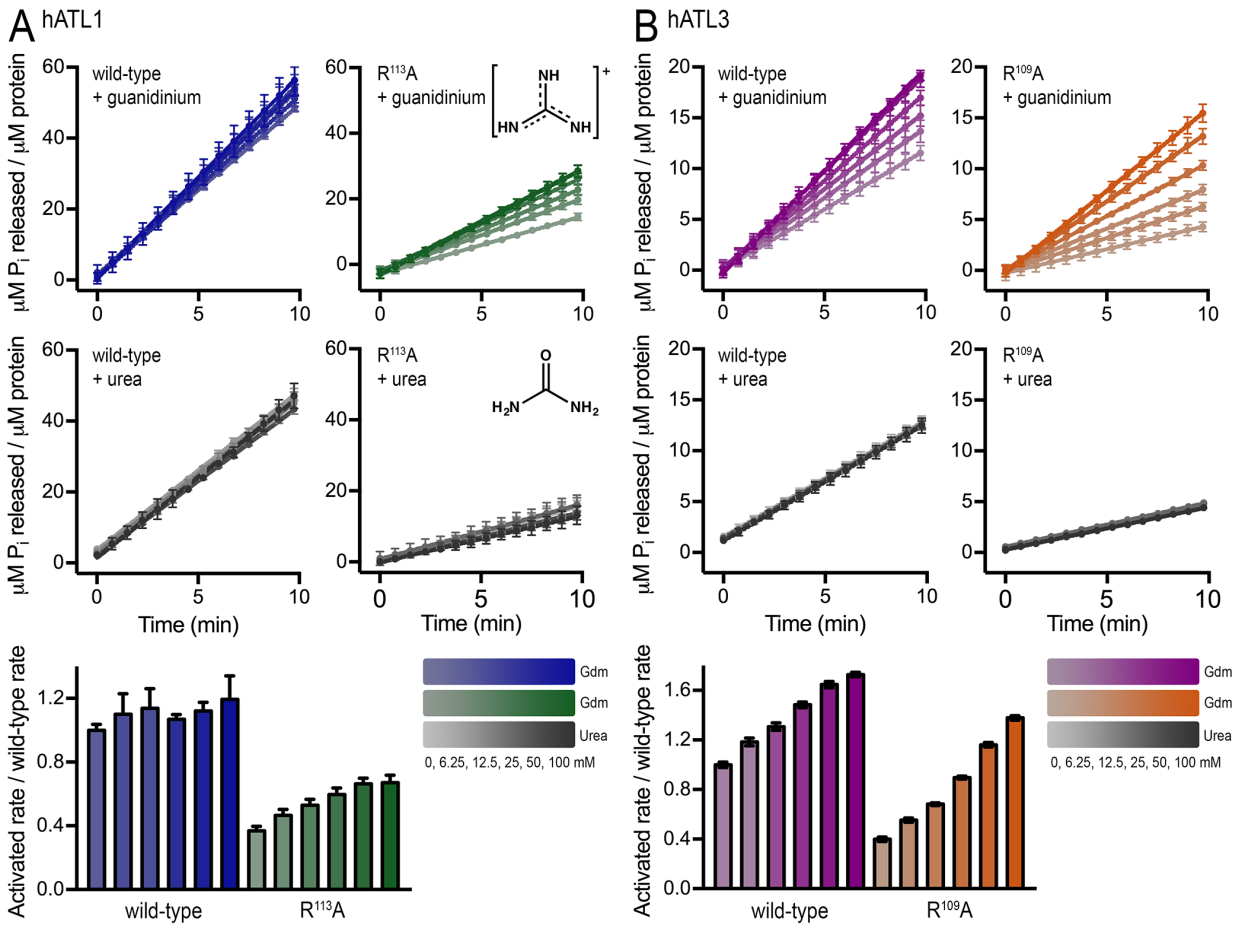


**Figure 2.11. Guanidinium rescues catalytic defects of hATL1-R$^{113}$A and hATL3-R$^{109}$A.** Phosphate release kinetics of hATL1 **(A)** and hATL3 **(B)** and their arginine mutants, R$^{113}$A and R$^{109}$A, respectively (hATL1 and hATL1-R$^{113}$A, 0.5 $\mu$M; hATL3 and hATL3-R$^{109}$A, 2 $\mu$M). Kinetics were measured using a coupled assay in the presence of increasing amounts of guanidinium (Gdm) or urea. Stimulated over wild-type (basal) rate is plotted in the lower panels. Graphs showing means and SEM are plotted from two biological replicates with three technical repeats each.

that the arginine residue is important for a post-hydrolysis step in ATL's catalytic cycle comes from affinity calculations based on nucleotide on- and off-rate measurements. The data show reduced affinity of hATL1 and hATL3 for mant-GDP, when R$^{113}$ or R$^{109}$, respectively, were mutated to alanine (*data not shown*). Results for mant-GTPγS showed a less consistent trend. These experiments were conducted with $Mg^{2+}$ in the reaction buffer. We also estimated the effect of $Mg^{2+}$ on nucleotide affinity by measuring reaction rates to wild-type and mutant protein at fixed enzyme and nucleotide

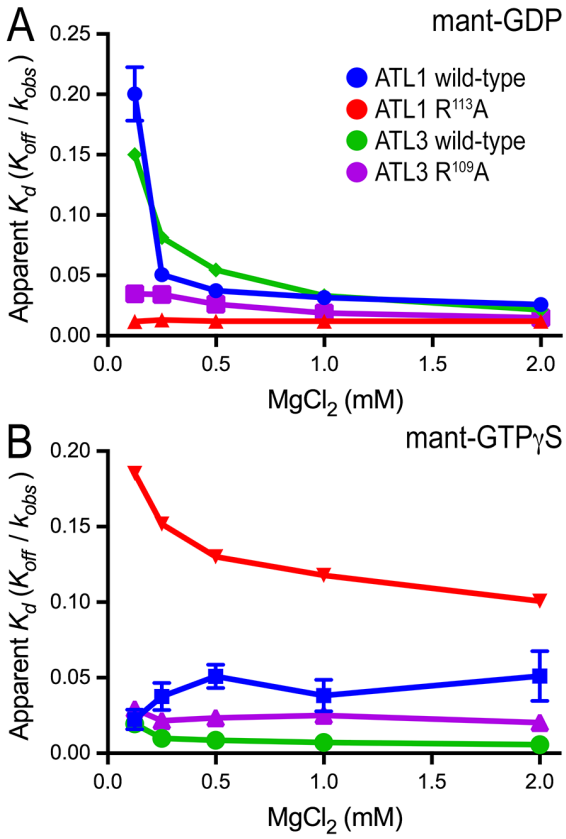


**Figure 2.12. Mg2+ effect on nucleotide binding to hATL1 and hATL3.** An apparent Kd based on mant-GDP (A) or mant-GTPγS (B) binding to hATL1 wild-type, hATL1-R113A, hATL3 wild-type, and hATL3-R109A (1 μM protein concentration) are plotted as a function of $Mg^{2+}$ concentration in the reaction. See Material and Methods for details. Graphs show the mean and standard error of the mean (SEM) of 3 technical replicates.

concentrations, but increasing $Mg^{2+}$ concentration **(Figure 2.12)**. Wild-type hATL1 and hATL3 show an inverse trend of $Mg^{2+}$ concentration and apparent GDP affinity, suggesting competition between the arginine residue and the catalytic $Mg^{2+}$ ion; this effect was lost in the corresponding arginine-to-alanine mutants.

We next tested the correlation between the loss-of-function phenotype to specific active site chemistry by attempting activity rescue experiments with the functional moiety of arginine (guanidinium) presented *in trans*. For these experiments, enzymatic activity was measured for both wild-type and mutant proteins in the presence of increasing amounts of guanidinium. Wild-type hATL1 responded to guanidinium only

marginally, while the corresponding $R^{113}A$ mutant could be rescued to ~70% of wild-type activity over the range of 0 - 100 mM additive **(Figure 2.11A)**. Because guanidinium is a protein denaturant, we wanted to ensure that this rescue effect was not due to a change in protein stability; therefore, we tested urea, a similarly sized yet distinct molecule with denaturing capabilities, which did not rescue activity **(Figures 2.11A and 2.11B)**. In contrast to hATL1, both wild-type hATL3 and the corresponding $R^{109}A$ mutant were activated significantly by guanidinium to levels of 170% and 140%, respectively **(Figure 2.11B)**.

To evaluate if guanidinium acts specifically via recycling the post-hydrolysis state of ATL, we compared the chemical rescue effect between continuously cycling enzymes versus enzymes undergoing only one round of hydrolysis. This experiment tests, albeit indirectly, the hypothesis that one role of the active site arginine residue ($R^{109}$ in hATL3) is in resetting ATL for subsequent hydrolysis cycles. If so, no effect should be apparent in phosphate release measured by single-turnover kinetics (equimolar GTP and ATL). We tested hATL3's catalytic core fragment and mutant thereof because it exhibited the most pronounced guanidinium response for both wild-type and $R^{109}A$ constructs. Our previous guanidinium rescue experiment measured phosphate release using a commercially available coupled biochemical reaction (Enzchek, Molecular Probes), which cannot be used to measure pre-steady state conditions. Thus, we returned to using the PBP-MDCC sensor both as a secondary independent assay to confirm the rescue effect of an actively cycling enzyme and to test guanidinium's effect on single-turnover reactions. As demonstrated in **Figure 2.11**, addition of guanidinium rescued the activity of an actively cycling wild-type and $R^{109}A$ hATL3 when an excess of GTP is

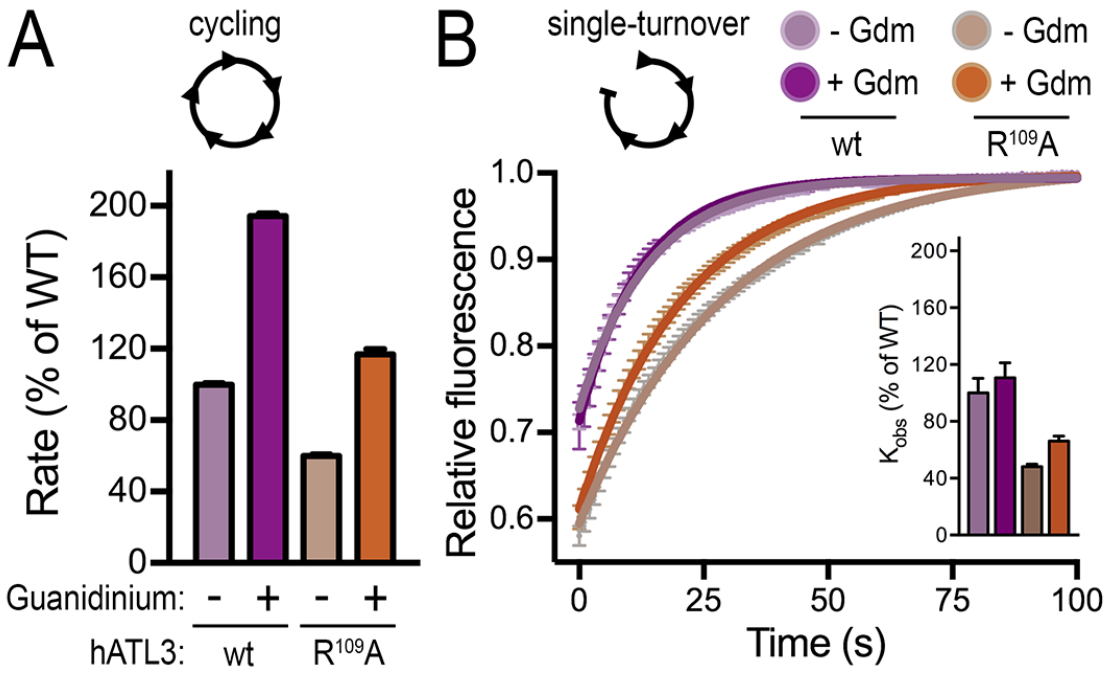


**Figure 2.13. Guanidinium accelerates steady state but not single-turnover kinetics of hATL3.** Phosphate release from wild-type or $R^{109}A$ hATL3 was measured in the absence or presence of 50 mM guanidinium using the PBP-MDCC phosphate sensor either under steady-state **(A)** or single-turnover **(B)** conditions. Graphs showing means and SEM are plotted from a minimum of two biological replicates with three technical repeats each.

present **(Figure 2.13A)**. As for the single-turnover reaction, the wild-type protein was unaffected by the addition of 50 mM guanidinium and the $R^{109}A$ mutant exhibited only a marginal increase in activity with guanidinium **(Figure 2.13B)**, suggesting a role for $R^{109}$ in cycle turnover. In other words, we were able to rescue enzyme activity when ATL is cycling but not under single-turnover conditions. We propose that the arginine is acting specifically in the removal of catalytic $Mg^{2+}$ and subsequently resetting the enzymatic cycle for the next rounds of GTP binding and hydrolysis.

## DISCUSSION

Here, we determined the timing of individual molecular events through ATL's catalytic cycle **(Figures 2.1-2.14)**. Our previous work illustrated that engagement of the middle and G domains facilitates GTP loading (Byrnes et al., 2013). We assess this domain orientation post-nucleotide binding via intramolecular-FRET measurements here. Upon nucleotide binding, a distance increase between the G and middle domains is observed. Both nucleotide binding and monomeric conformational changes proceed without lag-phases indicating that there is no accumulation of rate-limiting intermediates that would delay the reactions. The monomeric conformational change most likely occurs prior to GTP hydrolysis since it was observed with GTP, GDP, GppNHp, and GTPγS at comparable reaction rates that are slower than nucleotide binding events. This observation suggests that a power-stroke model where G domain dimers initiate hydrolysis for concerted switching of the middle domains is unlikely under the present experimental conditions. Additional results in support of this notion are provided by the non-hydrolyzable nucleotide analogs that do not promote G or middle domain dimerization anywhere near the rates with GTP for either hATL1 or hATL3 **(Figure 2.7)** (Byrnes et al., 2013).

Lag phases are apparent in the kinetics of hATL G and middle domain dimerization as well as phosphate release, which establish a clear succession of events **(Figures 2.6 and 2.14A)**. These kinetic signatures appear distinct from those observed with human GBP1, a prototype for this class of self-stimulated DRPs (Ghosh et al., 2006; Kunzelmann et al., 2006). Notably, phosphate release from GBP1 lacks a

pronounced lag phase (Kunzelmann et al., 2006), suggesting that hATL's mechanism is a variation of the canonical model in some regards.

Our comparative study revealed a conserved feature of an initial G domain encounter after GTP hydrolysis has been initiated. This step enables the subsequent dimerization of the otherwise monomeric middle domains in rapid succession by increasing the apparent local concentration to infinity, establishing a high-affinity tether, which explains why the catalytic core fragment comprising G and middle domain is an effective, GTP hydrolysis-dependent competitor of ATL-mediated membrane fusion unlike the individual G and middle domains (Moss et al., 2011; Pendin et al., 2011; Wang et al., 2016; 2013). Based on timing and enzyme cooperativity, we propose that homodimerization is required and may facilitate the release of phosphate. This interpretation is consistent with previous crystal structures that depict a hATL1 dimer as a tight dimer bound to a transition state analog and as a loosened dimer in a post-hydrolysis, GDP-bound state **(Figure 2.1C)** (Bian et al., 2011; Byrnes and Sondermann, 2011).

The general mechanisms are conserved in hATL1 and hATL3, although hATL3 proceeds through each key step of the GTP hydrolysis cycle significantly slower than hATL1, resulting in an overall 4-fold difference in catalytic rates between these two most distinct ATL isoforms. These differences are encoded solely in their respective G domains, despite sequence conservation being highest for this domain (73%) compared to the other domains and motifs in ATLs **(Figure 2.1B)**.

A recent study using an ATL ortholog from *Drosophila melanogaster* confirms our earlier observations of close-to concomitant G and middle domain dimerization in a

GTP-hydrolyzing system and established cooperativity in phosphate release activity akin to our results for hATL1 and hALT3 **(Figure 2.9)** (Winsor et al., 2017; Byrnes et al. 2013). In contrast to our model, authors proposed a transient G domain dimerization event prior to nucleotide hydrolysis that would precede the stable G and middle domain dimer to explain enzyme cooperativity. While this hypothesis awaits experimental confirmation, our timing studies indicate, at least for hATL1 and hATL3, a sequential process starting with GTP hydrolysis that is followed by G and middle domain dimerization **(Figure 2.14A)**. It is important to note that the cooperativity we report here signifies stimulated phosphate release and/or overcoming the energy barrier of the transition state. This argument is based on the observation that GTP binding alone is insufficient to drive G (or middle) domain dimerization at timescales observed with GTP. Our interpretation is supported by measuring GTP hydrolysis directly using quench-techniques, to establish that the initial burst of hydrolysis occurs in the ms time regime while complete homodimerization requires seconds (**Figure 2.8A).** Our model that GTP hydrolysis is initiated within an ATL monomer is bolstered by current studies on the fusion event, where fusion is preceded by the transient tethering of ATL-containing vesicles which requires GTP hydrolysis, not just GTP binding (Liu et al., 2015). ATLs are enriched at sites of membrane tethering and fusion (Saini et al., 2014), but evidence of higher order, regular arrays akin to dynamin assemblies remains elusive. Without higher order assembly, the synergy of a power stroke to drive fusion would be lost. Furthermore, ATL-mediated fusion requires continuous GTP hydrolysis in a cycling system (Liu et al., 2015; Wang et al., 2013; Wang et al., 2016). In MFN, continuous GTP hydrolysis is required for progressive assembly into an oligomeric docking ring, an

**Figure 2.14. Refined working model for a functional cycle of hATL. (A)** Sequence of conformational and quaternary structure changes. Timing is deduced from experiments carried out with hATL1. hATL3 follows the same functional cycles, yet this isoform proceeds through several key steps slower than hATL1. **(B)** Mechanism of nucleotide exchange in Rop-type small GTPases. The GEF PRONE8 induces a switch II conformation that introduces a clash between $A^{62}$ and catalytic site $Mg^{2+}$ ion. **(C)** Structural model for nucleotide exchange on Ypt7. The GEF complex Mon1•Ccz1 pushed Ypt7's switch I into the active site of the small GTPase. As one outcome, $K^{38}$ of the GTPase occupies the position of the catalytic $Mg^{2+}$ ion, a step important for nucleotide exchange.

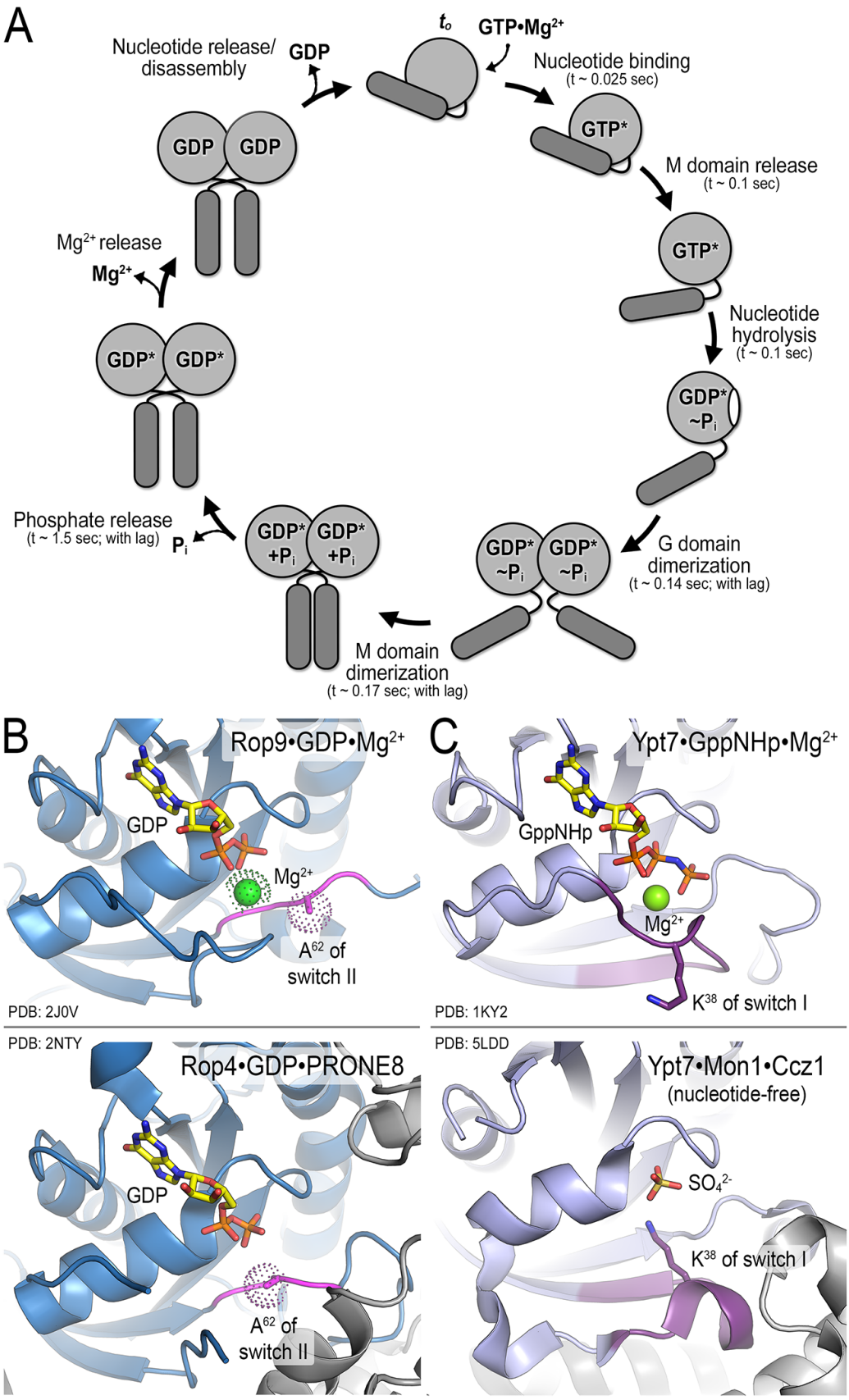
A
Nucleotide release/
disassembly
GDP
$t_o$
GTP•Mg2+
Nucleotide binding
(t ~ 0.025 sec)
GTP*
M domain release
(t ~ 0.1 sec)
GTP*
Nucleotide
hydrolysis
(t ~ 0.1 sec)
GDP*
~Pi
G domain
dimerization
(t ~ 0.14 sec; with lag)
GDP*
~Pi
GDP*
~Pi
M domain
dimerization
(t ~ 0.17 sec; with lag)
GDP*
+Pi
GDP*
+Pi
Phosphate release
(t ~ 1.5 sec; with lag)
Pi
GDP*
GDP*
Mg2+ release
Mg2+
GDP
GDP
B
Rop9•GDP•Mg2+
GDP
Mg2+
A62 of
switch II
PDB: 2J0V
C
Ypt7•GppNHp•Mg2+
GppNHp
Mg2+
K38 of switch I
PDB: 1KY2
PDB: 2NTY
Rop4•GDP•PRONE8
GDP
A62 of
switch II
PDB: 5LDD
Ypt7•Mon1•Ccz1
(nucleotide-free)
SO4 2-
K38 of switch I

intermediate thought to precede outer mitochondrial membrane fusion (Brandt et al., 2016). In addition, biochemical experiments assessing full-length MFN oligomerization and proteoliposome tethering (tethering experiments used a MFN chimera that includes dmATL transmembrane domains) determined that self-association of MFN through the soluble domains requires active GTP hydrolysis (Ishihara et al., 2004; Qi et al., 2016).

The requirement for continuous GTP hydrolysis for efficient membrane fusion postulates a mechanism for resetting ATL molecules post-hydrolysis and post-dimerization for subsequent rounds of action (Liu et al., 2015). The crystal structure of hATL3's catalytic core fragment provided novel mechanistic insight in this regard by revealing an intramolecular arginine residue that we propose assists in the recycling of the GDP•$Mg^{2+}$ bound state. This step could temporarily stabilize a GDP-bound complex or facilitate GDP release, enabling ATL to adopt a subsequent nucleotide-free state. The latter possibility of GDP•$Mg^{2+}$ clearance is supported by previously published structures of hATL1 depicting functional states of the enzyme (Byrnes et al., 2013; Byrnes and Sondermann, 2011): In the hATL1•GDP•$Mg^{2+}$ structure with the middle domain engaging the G domain (PDB 3Q5E) (Byrnes and Sondermann, 2011), the $Mg^{2+}$-displacing arginine residue $R^{113}$ faces outward and is highly flexible based on temperature factor analysis **(Figure 2.10E)**. In all GTP analog and transition state-bound structures (Byrnes et al., 2013), $R^{113}$ forms hydrogen bonds with the carbonyl from $E^{117}$ and the side chain of $E^{119}$, which appear to stabilize G2/switch I and cap the nucleotide-$Mg^{2+}$ binding site **(Figure 2.10F)** (Wittinghofer and Vetter, 2011). $R^{109}$ of hATL3 is conserved in all metazoan ATL orthologs, and appears to correspond structurally to $R^{59}$ in dynamin. $R^{59}$ toggles between an outward facing conformation in

the transition state (PDB 2X2F) (Chappie et al., 2010), to one in which its side chain points towards the $Mg^{2+}$ binding site in the GDP bound state (PDB 5D3Q) (Anand et al., 2016). These states in dynamin suggest a similar conformational change, whether $R^{59}$ has a similar role to hATL1 $R^{113}$ and hATL3 $R^{109}$ remains to be seen.

The stabilizing role of $R^{113}$ in ATL's transition state suggests a mechanistic role for the arginine beyond $Mg^{2+}$ displacement. This may explain the overall activity decrease with proteins mutated at that site and our inability to fully rescue hATL1 $R^{113}A$ to the rates exhibited by hATL1 wild-type protein **(Figures 2.11A and 2.13A)**. In the hATL1•GDP•$Mg^{2+}$ structure with parallel but loosely packed middle domains, which likely depicts a state following phosphate release (Byrnes et al., 2013; Byrnes and Sondermann, 2011), $F^{76}$ of the P-loop rotates upward and displaces the $R^{113}$-$E^{117}$ hydrogen bond and may destabilize G2/switch I in preparation for GDP•$Mg^{2+}$ release. The hATL3 structure included in this study depicts the arginine as fully occupying the $Mg^{2+}$-binding site and the G2/switch I retracted and open to allow GDP dissociation. Consistent with a role for this conserved ATL arginine to be required for a recycling step, the chemical rescue using guanidinium has a pronounced effect on steady state kinetics but not on the events leading up to phosphate release **(Figure 2.13)**.

Guanidinium also increases phosphate release of wild-type hATL3, a phenomenon that is less pronounced in hATL1. We speculate that dynamics of the loop displaying $R^{113}$ in hATL1 render the enzyme maximally efficient in $Mg^{2+}$ release, and hence a chemical rescue is only apparent in the $R^{113}A$ mutant protein where function is compromised. However, hATL3 is a much slower enzyme than hATL1. We hypothesize that the lower activity may be attributed at least in part to slower dynamics of the loop

that presents $R^{109}$ in hATL3. The postulated slower loop dynamics (or longer dwell times in an open and/or closed conformation) may allow guanidinium to exert an effect even on the wild-type protein, presumably targeting a state when $R^{109}$ would not occupy the position observed in the crystal structure.

Alterations to the $Mg^{2+}$-binding site have been described as a general mechanism for nucleotide exchange factors that facilitate the exchange of GDP for GTP in small G proteins (Bos et al., 2007). Structural and computational studies suggest that $Mg^{2+}$ removal can be achieved through shifting residues that coordinate $Mg^{2+}$, sterically occluding the $Mg^{2+}$-binding site, or repositioning of residues to displace the $Mg^{2+}$ (Béraud-Dufour et al., 1998; Boriack-Sjodin et al., 1998; Bos et al., 2007; Itzen et al., 2006; Kiontke et al., 2017; Mooney et al., 2016; Renault et al., 2001; Thomas et al., 2007). Two similar $Mg^{2+}$ displacement mechanisms have been shown structurally, where intramolecular residues (alanine and lysine) fulfill the role of ATL's arginine (Kiontke et al., 2017; Thomas et al., 2007). Thomas *et al.* determined the structure of the GDP-bound small GTP-binding protein Rop in complex with its guanine nucleotide exchange factor (GEF), PRONE8, which induces conformational changes of switch I and II and enable an alanine residue within Rop to displace $Mg^{2+}$. The absence of this configuration in the plant specific Rho GTPase Rop9 bound to GDP•$Mg^{2+}$ indicates it is specific to a nucleotide exchange mechanism **(Figure 2.14B)** (Sørmo et al., 2006; Thomas et al., 2007). Kiontke *et al.* determined the structure of the Mon1-Ccz1 complex (MC1), a GEF for the Rab GTPase Ypt7/Rab7, which shows rearrangement of switch I where the amine group of a switch I lysine residue occupies the position of the $Mg^{2+}$ ion

found in other nucleotide-bound structures **(Figure 2.14C)** (Constantinescu et al., 2002; Kiontke et al., 2017).

In summary, ATLs appear to be a self-regulating enzyme that combine intrinsic mechanisms for nucleotide loading via middle-G domain interactions (Byrnes et al., 2013), dimerization dependent stimulation of phosphate release, and nucleotide displacement through removal of the nucleotide-coordinating $Mg^{2+}$.

## MATERIALS AND METHODS

*Protein expression and purification.*

Bacterial overexpression plasmids for the catalytic core fragment of hATL1 (1-446), hATL3 (1-442), all point mutations including cysteine-engineered FRET variants, and PBP $A^{222}C$ were produced by standard molecular biology, following established protocols (Byrnes et al., 2013; Byrnes and Sondermann, 2011). Protein expression and purification were conducted as described previously (Brune et al., 1994; Byrnes et al., 2013; Byrnes and Sondermann, 2011). Briefly, proteins were expressed in *E. coli* BL21DE3 (at 18°C). Cells were collected by centrifugation, resuspended in $Ni^{2+}$-NTA A buffer (25 mM Tris pH 8.4, 500 mM NaCl, 20 mM Imidazole), sonicated, and soluble fractions were isolated via centrifugation at 38,000 x g for 1 hour. The hexahistidine-tagged proteins were enriched on $Ni^{2+}$-NTA matrix and eluted in $Ni^{2+}$-NTA A buffer containing 500 mM imidazole. Proteins were then buffer exchanged into 25 mM Tris pH 7.5, 400 mM NaCl, and 5 mM EDTA, concentrated, and subjected to gel filtration on a GE S200 16/60 liquid chromatography column equilibrated in 25 mM HEPES pH 7.5, 100 mM NaCl.

*Size-exclusion chromatography coupled to multi-angle light scattering.*

Protein samples at 40 µM were injected onto a WTC-050 SEC column (Wyatt Technology, Goleta, CA), equilibrated with 25 mM Tris pH 7.5, 100 mM NaCl, 4 mM $MgCl_2$, and 2 mM EGTA. Nucleotide depended oligomerization was assessed by incubating protein with various nucleotides at 1 mM for a minimum of 1 hour prior to SEC-MALS analysis. The gel filtration column was coupled to a static 18-angle light

scattering detector (DAWN HELEOS-II) and a refractive index detector (Optilab T-rEX) (Wyatt Technology, Goleta, CA). Data were collected every second at a flow rate of 1 ml/min. Data analysis was carried out using ASTRA VI, yielding the molar mass and mass distribution (polydispersity) of the sample. For normalization of the light scattering detectors and data quality control, monomeric fraction of BSA (Sigma, St. Louis, MO) was also analyzed.

*Dye Labeling.*

Site-specific dye labeling was achieved by replacing non-conserved surface amino acids with cysteine residues within the G, middle, or both domains. To maintain singly labeled protein, surface exposed cysteine residues for both hATL1 and hATL3 were replaced with alanine residues. Construct-specific mutations for intra- and intermolecular FRET are listed in Figure S2. Labeling was conducted at 100 μM protein, 150 μM AlexaFluor-488, AlexaFluor-647 (Molecular Probes, Eugene, OR), or both, in a buffer containing 25 mM HEPES pH 7, 100 mM NaCl. This reaction was incubated on ice for 30 minutes and excess dye was removed with a NAP-5 column (GE, Marlborough, MA) pre-equilibrated with buffer containing 25 mM HEPES pH 7.5, 100 mM NaCl, 2 mM $MgCl_2$. PBP with a hexahistidine C-terminal tag (100 μM) was labeled with MDCC (Sigma, St. Louis, MO) (150 μM) in the presence of a phosphate mop (0.4 U/mL purine nucleoside phosphorylase and 400 μM 7-Methylguanosine from Sigma, St. Louis, MO for 1 hour at 25ºC. Purification of the phosphate-free PBP-MDCC was achieved with Qiagen $Ni^{2+}$-NTA and subsequent buffer exchanged into 25 mM HEPES pH 7.5 and 100 mM NaCl using a PD-10 column (GE, Marlborough, MA).

*Stopped-flow nucleotide-binding, FRET, and phosphate release kinetics.*

Experiments were conducted at 25ºC on an SX-20 stopped-flow spectrofluorometer (Applied Photophysics, Leatherhead, UK) equipped with a 150-W xenon lamp with a standard and a red-shifted (for FRET assays) photomultiplier tubes (Applied Photophysics, Leatherhead, UK). Data for FRET time courses (equilibrium and steady state measurements) were collected with a Gemini EM microplate reader (Molecular Devices, Sunnyvale, CA) with sensor excitation at 473 nm and fluorescence being recorded at 515 and 665 nm for donor and acceptor channels respectively. All experimental reactions consist of 1 or 5 μM protein and 500 μM nucleotide in a buffer containing 25 mM HEPES pH 7.5, 100 mM NaCl, and 2 mM $MgCl_2$.

Single-fluorescence measurements: Nucleotide binding with mant-GDP or mant-GTP (Molecular Probes, Eugene, OR) was measured with an excitation wavelength of 290 nm and fluorescence was recorded above 420 nm using a Schott high-pass filter (Schott, Elmsford, NY). Phosphate release measurements with wild-type ATL protein containing 10 μM PBP-MDCC used excitation at 425 nm and fluorescence signals were recorded above 455 nm using a Schott high-pass filter (Schott, Elmsford, NY).

Dual-fluorescence measurements: Intramolecular FRET reactions used a 1:10 ratio of stochastically labeled protein (0.1 μM) and unlabeled protein (0.9 μM). Intermolecular FRET reactions use a 1:1 ratio of donor and acceptor labeled proteins (0.5 μM each). AlexaFluor-488 and AlexaFluor-647 excitation wavelength was set to 420 nm and emission filters used were Chroma D525/50 band-pass filter (Chroma, Bellows

Falls, VT) and a 645 nm Schott high-pass filter (Schott, Elmsford, NY) for donor and acceptor fluorescence, respectively.

*Single-turnover enzyme kinetics.*

Single-turnover experiments were conducted with 15 μM GTP, 15 μM protein, 15 μM PBP-MDCC, in the absence or presence of 50 mM guanidinium. Data collection was conducted with a Hi-Tech SFA-20 stopped-flow coupled to a Fluoromax-4 spectrofluorometer (excitation of 430 nm, emission of 468 nm, 2 nm slits) at 25ºC.

*Stopped-flow data processing.*

Mant-nucleotide maximum binding signals were baseline-adjusted to a final value of 1. Raw FRET donor and acceptor signals were used to calculate a FRET efficiency where FRET efficiency = $I_{Acceptor}$ / ($I_{Donor}$ + $I_{Acceptor}$). Intramolecular FRET efficiency was baseline-adjusted to an initial value of 1. Mant-nucleotide binding data and intramolecular FRET data were fit to single exponential association and single/double exponential decay function, respectively. Intermolecular FRET efficiencies were normalized between 0 and 1. Raw PBP-MDCC phosphate binding results were averaged and displayed as relative changes in fluorescence. All results displayed are the mean values ± SEM (in several graphs, error bars were smaller than the data point symbols and hence appear absent). Lag times for stopped-flow G and middle domain FRET and phosphate release were defined by the duration of time it takes to transition from the lag to exponential growth phases. This time point was calculated by fitting early data points to a third order polynomial and taking the first and second derivatives to

determine when the second derivative is equal to zero **(Figure S6)**. All data processing and fitting was completed using GraphPad Prism (GraphPad, La Jolla, CA).

*Steady state phosphate release kinetics.*

Enzchek phosphate detection kit was used as described by manufacturer (Molecular Probes, Eugene, OR) with the exception of the addition of NaCl to the reaction buffer at a final concentration of 100 mM. A range of protein concentrations was assayed with an initial amount of 500 μM GTP present at 25ºC. Raw data were converted to μM phosphate with a standard curve and the first 20% of substrate conversion was fit to a linear regression to obtain the rate (μM Pi/min). The rate is plotted as a function of enzyme concentration in (μM) and the slope of the linear regression is the turnover number ($k_{cat} = V$ / [Enzyme]).

PBP•MDCC phosphate release measurements were conduced in a reaction containing 25 mM HEPES pH 7.5, 100 mM $NaCl_2$, 2 mM $MgCl_2$, 500 μM GTP, and 10 μM PBP•MDCC at 25ºC. 50 μM BSA was added to stabilize enzymes at low concentrations (Kunzelmann et al., 2005). A range of enzyme concentrations were used. Data were collected with a Gemini EM microplate reader (Molecular Devices, Sunnyvale, CA) with sensor excitation 430 nm and fluorescence being recorded at 468 nm. Data processing to attain rates (μM phosphate / min) and $k_{cat}$ ($min^{-1}$) was conducted as mentioned above. The $k_{cat}$ values were also plotted as a function of enzyme concentration to illustrate stimulated phosphate release; these data were fit to a saturation-binding model ($Y = Y_{max}*E/(K_d + E)$) to calculate activity-derived dimerization $K_d$ values.

*Quench Flow Kinetics.*

Rapid GTP hydrolysis was measured directly using both an SX-20 stopped-flow spectrofluorometer (Applied Photophysics, Leatherhead, UK) equipped with a quench flow adaptor or a KinTek RQF-3 (KinTek Corp., Austin, TX) at 25ºC. A reaction containing 25 mM Tris pH 7.5, 100 mM $NaCl_2$, 2 mM $MgCl_2$, 500 μM GTP, and 1 μM ATL was quenched with a final concentration of 10% trichloroacetic acid and neutralized with 1.5 M Tris pH 8.8. Longer time points were initiated and quenched manually. Free phosphate was measured with 5 μM PBP•MDCC using a Gemini EM microplate reader (Molecular Devices, Sunnyvale, CA) with sensor excitation 430 nm and fluorescence being recorded at 468 nm. Data collected on each instrument (8 technical replicates using the SX-20 and 3 technical replicates using the KinTek RQF-3), were normalized and averaged.

*hATL3 crystallization.*

hATL3 crystals were obtained for the catalytic core fragment comprising residues (21-442) through sitting drop vapor diffusion. Protein (10-30 mg/ml) was incubated with 2 mM GTPγS / 4 mM $MgCl_2$ for 1 hour at 25°C, mixed with an equal volume of reservoir solution, and incubated at 20°C. Initial crystals unsuitable for data collection were obtained using a reservoir solution of 0.2 M NaCl, 0.1 M Tris pH 8.5, 25% PEG3350. A seed stock in reservoir solution was prepared using Seed Beads™ (Hampton Research, Aliso Viejo, CA) and subsequent optimizations were performed via hanging drop vapor diffusion by adding crystal seed stock to drops containing protein (30 mg/ml), 0.2 M

NaCl, 0.1 M Tris pH 8.5, 25% PEG3350. Large single crystals appeared within 24 hours at 20°C and, upon harvesting, were soaked in the previously mentioned condition supplemented with 25% glycerol as a cyroprotectant for 5 minutes and frozen in liquid nitrogen.

X-ray diffraction data were collected at the Cornell High Energy Synchrotron Source (CHESS). Data processing and scaling was carried out with X-ray Detector Software (XDS) and CCP4 software suite (Kabsch, 2010; Winn et al., 2011). Phases were attained through Molecular Replacement (MR) methods using the PHENIX software package and the coordinates of hATL1 (PDB 3Q5E) as the search model ((Adams et al., 2010)). Refinements were carried out in PHENIX (Adams et al., 2010) and COOT (Emsley and Cowtan, 2004), producing the final model. Data collection and model statistics are summarized in Table 1. Figure illustrations were made in Pymol (Version 1.8.4, Schrödinger, LLC). The aforementioned software packages were accessed through SBGrid (www.sbgrid.org; (Morin et al., 2013)).

*N-Methylanthraniloyl (Mant)-nucleotide binding.*

On and off rates of mant-GDP and mant-GTPγS were determined by monitoring increased fluorescence upon mant-nucleotide binding to ATL. A KinTek SF-2004 stopped-flow was used to rapidly mix ATL and mant-nucleotides to a final concentration of 1 μM ATL and increasing amounts of nucleotide (2.4 - 12 μM) at 25ºC. Samples were excited using an Ocean Optics DH-mini deuterium light source and the emission fluorescence was collected using an HQ460/40 emission filter (Chroma). Data were fit to exponential association equations and the rate constants were plotted versus

nucleotide concentration. The resulting slope of the linear fit corresponds to $k_{on}$ and the y-intercept to $k_{off}$. Dissociation constants ($K_d$) were calculated as $k_{off}$ / $k_{on}$. An apparent $K_d$ ($k_{off}$ / $k_{obs}$) was reported in experiments varying the amount of $MgCl_2$. In this case, the $k_{off}$ values were directly measured at various $MgCl_2$ concentrations by mixing 1 μM protein with 5 μM mant-nucleotide and chasing with 1 mM unlabeled nucleotide. Single-exponential decay rate constant yielded $k_{off}$. The apparent $k_{on}$ ($k_{obs}$) values were measured at various $MgCl_2$ concentrations by mixing 1 μM ATL and 5.4 μM mant-nucleotide, and data were fit to exponential association equations with the rate constant yielding $k_{obs}$.

*Quantification and statistical analysis.*

Data fitting including baseline corrections, normalization, calculation of mean and error (SEM), and statistical tests were carried out in GraphPad Prism (version 7.0a). The number of biological and technical replicates as well as the entity plotted are indicated in the figure legends. Data baseline correction and normalization, where applied, were indicated in the corresponding method section and in the axis labels. No explicit power analysis was used.

*Data and Software Availability.*

The coordinates of the hATL3•GDP crystal structure have been deposited in the PDB under accession code PDB 5VGR.

## REFERENCES


Adams, P.D., Afonine, P.V., Bunkoczi, G., Chen, V.B., Davis, I.W., Echols, N., Headd, J.J., Hung, L.W., Kapral, G.J., Grosse-Kunstleve, R.W., et al. (2010). PHENIX: a comprehensive Python-based system for macromolecular structure solution. Acta Crystallogr. D Biol. Crystallogr. 66, 213-221.

Anand, R., Eschenburg, S., and Reubold, T.F. (2016). Crystal structure of the GTPase domain and the bundle signalling element of dynamin in the GDP state. Biochem. Bioph. Res. Co. 469, 76–80.

Aumiller, W.M., Jr., Davis, B.W., Hatzakis, E., and Keating, C.D. (2014). Interactions of macromolecular crowding agents and cosolutes with small-molecule substrates: effect on horseradish peroxidase activity with two different substrates. J. Phys. Chem. B 118, 10624–10632.

Béraud-Dufour, S., Robineau, S., Chardin, P., Paris, S., Chabre, M., Cherfils, J., and Antonny, B. (1998). A glutamic finger in the guanine nucleotide exchange factor ARNO displaces Mg2+ and the beta-phosphate to destabilize GDP on ARF1. EMBO J. 17, 3651–3659.

Bian, X., Klemm, R.W., Liu, T.Y., Zhang, M., Sun, S., Sui, X., Liu, X., Rapoport, T.A., and Hu, J. (2011). Structures of the atlastin GTPase provide insight into homotypic fusion of endoplasmic reticulum membranes. Proc. Natl. Acad. Sci. USA 108, 3976–3981.

Boriack-Sjodin, P.A., Margarit, S.M., Bar-Sagi, D., and Kuriyan, J. (1998). The structural basis of the activation of Ras by Sos. Nature 394, 337–343.

Bos, J.L., Rehmann, H., and Wittinghofer, A. (2007). GEFs and GAPs: critical elements in the control of small G proteins. Cell 129, 865–877.

Brandt, T., Cavellini, L., Kühlbrandt, W., and Cohen, M.M. (2016). A mitofusin-dependent docking ring complex triggers mitochondrial fusion in vitro. eLife 5, e14618.

Brune, M., Hunter, J.L., Corrie, J.E., and Webb, M.R. (1994). Direct, real-time measurement of rapid inorganic phosphate release using a novel fluorescent probe

and its application to actomyosin subfragment 1 ATPase. Biochemistry 33, 8262–8271.

Byrnes, L.J., Singh, A., Szeto, K., Benvin, N.M., O'Donnell, J.P., Zipfel, W.R., and Sondermann, H. (2013). Structural basis for conformational switching and GTP loading of the large G protein atlastin. EMBO J. 32, 369–384.

Byrnes, L.J., and Sondermann, H. (2011). Structural basis for the nucleotide-dependent dimerization of the large G protein atlastin-1/SPG3A. Proc. Natl. Acad. Sci. USA 108, 2216–2221.

Chappie, J.S., Acharya, S., Leonard, M., Schmid, S.L., and Dyda, F. (2010). G domain dimerization controls dynamin's assembly-stimulated GTPase activity. Nature 465, 435–440.

Constantinescu, A.-T., Rak, A., Alexandrov, K., Esters, H., Goody, R.S., and Scheidig, A.J. (2002). Rab-subfamily-specific regions of Ypt7p are structurally different from other RabGTPases. Structure 10, 569–579.

Daumke, O., and Praefcke, G.J.K. (2016). Mechanisms of GTP hydrolysis and conformational transitions in the dynamin superfamily. Biopolymers 105, 580–593.

Emsley, P., and Cowtan, K. (2004). Coot: model-building tools for molecular graphics. Acta Crystallogr. D Biol. Crystallogr. 60, 2126–2132.

Faust, J.E., Desai, T., Verma, A., Ulengin, I., Sun, T.L., Moss, T.J., Betancourt-Solis, M.A., Huang, H.W., Lee, T., and McNew, J.A. (2015). The atlastin C-terminal tail is an amphipathic helix that perturbs the bilayer structure during endoplasmic reticulum homotypic fusion. J. Biol. Chem. 290, 4772–4783.

Ferguson, S.M., and De Camilli, P. (2012). Dynamin, a membrane-remodelling GTPase. Nat. Rev. Mol. Cell. Biol. 13, 75–88.

Fink, J.K. (2013). Hereditary spastic paraplegia: clinico-pathologic features and emerging molecular mechanisms. Acta Neuropathol. 126, 307-328.

Fischer, D., Schabhuttl, M., Wieland, T., Windhager, R., Strom, T.M., and Auer-Grumbach, M. (2014). A novel missense mutation confirms ATL3 as a gene for hereditary sensory neuropathy type 1. Brain 137, e286.

Gasper, R., Meyer, S., Gotthardt, K., Sirajuddin, M., and Wittinghofer, A. (2009). It takes two to tango: regulation of G proteins by dimerization. Nat. Rev. Mol. Cell. Biol. 10, 423–429.

Ghosh, A., Praefcke, G.J.K., Renault, L., Wittinghofer, A., and Herrmann, C. (2006). How guanylate-binding proteins achieve assembly-stimulated processive cleavage of GTP to GMP. Nature 440, 101–104.

Guelly, C., Zhu, P.-P., Leonardis, L., Papić, L., Zidar, J., Schabhüttl, M., Strohmaier, H., Weis, J., Strom, T.M., Baets, J., et al. (2011). Targeted high-throughput sequencing identifies mutations in atlastin-1 as a cause of hereditary sensory neuropathy type I. Am. J. Hum. Genet. 88, 99–105.

Hu, J., Shibata, Y., Zhu, P.P., Voss, C., Rismanchi, N., Prinz, W.A., Rapoport, T.A., and Blackstone, C. (2009). A class of dynamin-like GTPases involved in the generation of the tubular ER network. Cell 138, 549–561.

Hu, X., Wu, F., Sun, S., Yu, W., and Hu, J. (2015). Human atlastin GTPases mediate differentiated fusion of endoplasmic reticulum membranes. Protein Cell 6, 307–311.

Hubner, C.A., and Kurth, I. (2014). Membrane-shaping disorders: a common pathway in axon degeneration. Brain 137, 3109–3121.

Ingólfsson, H.I., and Andersen, O.S. (2010). Screening for small molecules' bilayer-modifying potential using a gramicidin-based fluorescence assay. Assay Drug Dev. Technol. 8, 427–436.

Ishihara, N., Eura, Y., and Mihara, K. (2004). Mitofusin 1 and 2 play distinct roles in mitochondrial fusion reactions via GTPase activity. J. Cell. Sci. 117, 6535–6546.

Itzen, A., Pylypenko, O., Goody, R.S., Alexandrov, K., and Rak, A., (2006). Nucleotide exchange via local protein unfolding--structure of Rab8 in complex with MSS4. EMBO J. 25, 1445–1455.

Kabsch, W. (2010). XDS. Acta Crystallogr. D Biol. Crystallogr. 66, 125-132.

Kiontke, S., Langemeyer, L., Kuhlee, A., Schuback, S., Raunser, S., Ungermann, C., and Kümmel, D. (2017). Architecture and mechanism of the late endosomal Rab7-like Ypt7 guanine nucleotide exchange factor complex Mon1-Ccz1. Nature Commun. 8, 14034.

Krissinel, E., and Henrick, K. (2007). Inference of macromolecular assemblies from crystalline state. J. Mol. Biol. 372, 774–797.

Kunzelmann, S., Praefcke, G.J.K., and Herrmann, C. (2006). Transient kinetic investigation of GTP hydrolysis catalyzed by interferon-gamma-induced hGBP1 (human guanylate binding protein 1). J. Biol. Chem. 281, 28627–28635.

Kunzelmann, S., Praefcke, G.J.K., and Herrmann, C. (2005). Nucleotide binding and self-stimulated GTPase activity of human guanylate-binding protein 1 (hGBP1). Meth. Enzymol. 404, 512–527.

Li, J., Yan, B., Si, H., Peng, X., Zhang, S.L., and Hu, J. (2017). Atlastin regulates store-operated calcium entry for nerve growth factor-induced neurite outgrowth. Sci Rep 7, 43490.

Liu, T.Y., Bian, X., Sun, S., Hu, X., Klemm, R.W., Prinz, W.A., Rapoport, T.A., and Hu, J. (2012). Lipid interaction of the C terminus and association of the transmembrane segments facilitate atlastin-mediated homotypic endoplasmic reticulum fusion. Proc. Natl. Acad. Sci. USA 109, E2146.

Liu, T.Y., Bian, X., Romano, F.B., Shemesh, T., Rapoport, T.A., and Hu, J. (2015). Cis and trans interactions between atlastin molecules during membrane fusion. Proc. Natl. Acad. Sci. USA 112, E1851–E1860.

McNew, J.A., Sondermann, H., Lee, T., Stern, M., and Brandizzi, F. (2013). GTP-dependent membrane fusion. Annu. Rev. Cell Dev. Biol. 29, 529–550.

Mooney, M.C., Xu, Y., McClory, J., and Huang, M. (2016). A disappearing act performed by magnesium: the nucleotide exchange mechanism of Ran GTPase by quantum mechanics/ molecular mechanics studies. Theor. Chem. Acc. 135, 1–13.

Morin, A., Eisenbraun, B., Key, J., Sanschagrin, P.C., Timony, M.A., Ottaviano, M., and Sliz, P. (2013). Collaboration gets the most out of software. eLife 2, e01456.

Moss, T.J., Andreazza, C., Verma, A., Daga, A., and McNew, J.A. (2011). Membrane fusion by the GTPase atlastin requires a conserved C-terminal cytoplasmic tail and dimerization through the middle domain. Proc. Natl. Acad. Sci. USA 108, 11133–11138.

Muriel, M.P., Dauphin, A., Namekawa, M., Gervais, A., Brice, A., and Ruberg, M. (2009). Atlastin-1, the dynamin-like GTPase responsible for spastic paraplegia SPG3A, remodels lipid membranes and may form tubules and vesicles in the endoplasmic reticulum. J. Neurochem. 110, 1607–1616.

Nixon-Abell, J., Obara, C.J., Weigel, A.V., Li, D., Legant, W.R., Xu, C.S., Pasolli, H.A., Harvey, K., Hess, H.F., Betzig, E., et al. (2016). Increased spatiotemporal resolution reveals highly dynamic dense tubular matrices in the peripheral ER. Science 354, aaf3928.

Orso, G., Pendin, D., Liu, S., Tosetto, J., Moss, T.J., Faust, J.E., Micaroni, M., Egorova, A., Martinuzzi, A., McNew, J.A., et al. (2009). Homotypic fusion of ER membranes requires the dynamin-like GTPase atlastin. Nature 460, 978–983.

Pendin, D., Tosetto, J., Moss, T.J., Andreazza, C., Moro, S., McNew, J.A., and Daga, A. (2011). GTP-dependent packing of a three-helix bundle is required for atlastin-mediated fusion. Proc. Natl. Acad. Sci. USA 108, 16283–16288.

Polisetty, R.V., Gautam, P., Sharma, R., Harsha, H.C., Nair, S.C., Gupta, M.K., Uppin, M.S., Challa, S., Puligopu, A.K., Ankathi, P., et al. (2012). LC-MS/MS analysis of differentially expressed glioblastoma membrane proteome reveals altered calcium signaling and other protein groups of regulatory functions. Mol. Cell. Proteomics 11, M111.013565.

Praefcke, G.J.K., and McMahon, H.T. (2004). The dynamin superfamily: universal membrane tubulation and fission molecules? Nat. Rev. Mol. Cell. Biol. 5, 133–147.

Qi, Y., Yan, L., Yu, C., Guo, X., Zhou, X., Hu, X., Huang, X., Rao, Z., Lou, Z., and Hu, J. (2016). Structures of human mitofusin 1 provide insight into mitochondrial tethering. J. Cell Biol. 215, 621–629.

Rao, K., Stone, M.C., Weiner, A.T., Gheres, K.W., Zhou, C., Deitcher, D.L., Levitan, E.S., and Rolls, M.M. (2016). Spastin, atlastin, and ER relocalization are involved in axon but not dendrite regeneration. Mol. Biol. Cell 27, 3245–3256.

Renault, L., Kuhlmann, J., Henkel, A., and Wittinghofer, A. (2001). Structural basis for guanine nucleotide exchange on Ran by the regulator of chromosome condensation (RCC1). Cell 105, 245–255.

Renvoisé, B., and Blackstone, C. (2010). Emerging themes of ER organization in the development and maintenance of axons. Curr. Opin. Neurobiol. 20, 531–537.

Rismanchi, N., Soderblom, C., Stadler, J., Zhu, P.P., and Blackstone, C. (2008). Atlastin GTPases are required for Golgi apparatus and ER morphogenesis. Hum. Mol. Genet. 17, 1591–1604.

Saini, S.G., Liu, C., and Lee, T.H. (2014). Membrane tethering by the atlastin GTPase depends on GTP hydrolysis but not on forming the cross-over configuration. Mol. Biol. Cell 25, 3942–3953.

Sørmo, C.G., Leiros, I., Brembu, T., Winge, P., Os, V., and Bones, A.M. (2006). The crystal structure of Arabidopsis thaliana RAC7/ROP9: The first RAS superfamily GTPase from the plant kingdom. Phytochemistry 67, 2332–2340.

Thomas, C., Fricke, I., Scrima, A., Berken, A., and Wittinghofer, A. (2007). Structural evidence for a common intermediate in small G Protein-GEF reactions. Mol. Cell 25, 141–149.

Wang, S., Romano, F.B., Field, C.M., Mitchison, T.J., and Rapoport, T.A. (2013). Multiple mechanisms determine ER network morphology during the cell cycle in Xenopus egg extracts. J. Cell Biol. 203, 801–814.

Wang, S., Tukachinsky, H., Romano, F.B., and Rapoport, T.A. (2016). Cooperation of the ER-shaping proteins atlastin, lunapark, and reticulons to generate a tubular membrane network. eLife 5, e18605.

Warnock, D.E., Hinshaw, J.E., and Schmid, S.L. (1996). Dynamin self-assembly stimulates its GTPase activity. J. Biol. Chem. 271, 22310–22314.

Winn, M.D., Ballard, C.C., Cowtan, K.D., Dodson, E.J., Emsley, P., Evans, P.R., Keegan, R.M., Krissinel, E.B., Leslie, A.G.W., McCoy, A., et al. (2011). Overview of the CCP4 suite and current developments. Acta Crystallogr. D Biol. Crystallogr. 67, 235–242.

Winsor, J., Hackney, D.D., and Lee, T.H. (2017). The crossover conformational shift of the GTPase atlastin provides the energy driving ER fusion. J. Cell Biol. jcb. 201609071.

Wittinghofer, A., and Vetter, I.R. (2011). Structure-function relationships of the G domain, a canonical switch motif. Annu. Rev. Biochem. 80, 943–971.

Wu, F., Hu, X., Bian, X., Liu, X., and Hu, J. (2015). Comparison of human and Drosophila atlastin GTPases. Protein Cell 6, 139–146.

Yan, L., Sun, S., Wang, W., Shi, J., Hu, X., Wang, S., Su, D., Rao, Z., Hu, J., and Lou, Z. (2015). Structures of the yeast dynamin-like GTPase Sey1p provide insight into homotypic ER fusion. J. Cell Biol. 210, 961–972.

Zhao, G., Zhu, P.P., Renvoisé, B., Maldonado-Báez, L., Park, S.H., and Blackstone, C. (2016). Mammalian knock out cells reveal prominent roles for atlastin GTPases in ER network morphology. Exp. Cell. Res. 349, 32-44.

# CHAPTER 3

# DEFECTIVE ALLOSTERIC COUPLING IN THE CATALYTIC CORE OF A MUTANT ATLASTIN ASSOCIATED WITH HEREDITARY SPASTIC PARAPLEGIA §

## ABSTRACT

The dynamin-related GTPase atlastin (ATL) catalyzes membrane fusion of the endoplasmic reticulum (ER), establishing a network of branched membrane tubules. When ATL function is compromised, morphology of the ER deteriorates and can result in neurological disorders such as Hereditary Spastic Paraplegia (HSP) and Hereditary Sensory Neuropathy (HSN). ATLs harness the energy of GTP hydrolysis to initiate a series of conformational changes that enable homodimerization and subsequent membrane fusion. Disease-associated mutations cluster in regions adjacent to ATL's catalytic site, but the consequences for its molecular mechanism are often poorly understood. Here, we elucidate structural and functional defects of an atypical HSP variant, ATL1-$F^{151}S$, that is impaired in its nucleotide hydrolysis cycle but still capable of sampling the high affinity homodimer when bound to a transition state analog. Crystal structures of mutant proteins yield models of the monomeric pre-hydrolysis and post-hydrolysis states of ATL. Together, these studies define a mechanism for allosteric coupling where $F^{151}$ is the central residue in a hydrophobic interaction network connecting the active-site to an inter-domain interface responsible for nucleotide loading.

---

§ The following sections comprise a forthcoming manuscript. Contributors include John P. O'Donnell, Laura Byrnes, Richard B. Cooley, and Holger Sondermann.

## INTRODUCTION

Hereditary spastic paraplegia (HSP) comprises a group of genetic neurological disorders that manifest as spasticity and weakness in the distal extremities. One of the predominantly mutated loci contributing to HSP is the atlastin-1 (*atl1*) gene which causes ~10% of autosomal dominant (subtype SPG3A) and the majority of early onset cases (Fink, 2013). Similarly, mutations in *atl1* and *atl3* were identified recently as a cause of Hereditary Sensory Neuropathy (HSN) type I (Fischer et al., 2014; Guelly et al., 2011; Kornak:2014ib), emphasizing the crucial role of atlastins (ATLs) in axonopathies and for normal cellular physiology (Hubner and Kurth, 2014).

The *atl* genes encode for a subclass within the dynamin-related protein (DRP) superfamily (Ferguson and De Camilli, 2012). DRPs use the energy from GTP hydrolysis to control a multitude of cellular events including vesicle scission, fusion and fission of organelle membranes, cytokinesis, and antiviral activity (Praefcke and McMahon, 2004). DRPs often contain a GTPase (G) domain, helical middle domain, lipid association domain, and GTPase effector domain (GED) that forms part of the protein's stalk which is important for oligomerization and assembly-dependent enzyme stimulation (Daumke and Praefcke, 2016; Praefcke and McMahon, 2004). Similarly, ATLs consist of G and middle domains, and a transmembrane anchor, but lack the canonical GED, and consequentially do not form regular higher-order complexes akin to those observed with dynamin, GBP and MxA (Chappie et al., 2010; Ghosh et al., 2006; Haller et al., 2010).

ATLs localize to the endoplasmic reticulum (ER) where they catalyze the fusion of membrane tubules to form three-way junctions, establishing the highly reticular

morphology of the smooth ER found at the periphery of the cell body (J. Hu et al., 2009; Orso et al., 2009; Rismanchi et al., 2008). The branched structure of the peripheral ER is suppressed upon the expression of dominant-negative ATL alleles, gene deletions, and transient siRNA knock-downs (J. Hu et al., 2009; Rismanchi et al., 2008; Wang et al., 2016; G. Zhao et al., 2016). In a reconstituted system using an invertebrate *Drosophila melanogaster* ortholog, catalytically active ATL is sufficient to generate and maintain a branched, tubular network from liposomes (Powers et al., 2017). Effective fusion of these membranes both *in vitro* and in the cell rely on ATLs traversing multiple cycles of conformational changes and oligomerization events that are driven by both GTP binding and hydrolysis (Byrnes et al., 2013; Liu et al., 2015; O'Donnell et al., 2017; Powers et al., 2017). Higher eukaryotic genomes typically encode three main ATL isoforms (ATL1-3) with varying GTPase activity and notable differences in sub-cellular localization (X. Hu et al., 2015; Yan et al., 2015). ATL1 is the most active isoform and decorates the tubular ER network evenly, whereas ATL3 is a less efficient enzyme and localizes preferentially to junction points in the ER network that appear to be associated with membrane fusion events (Nixon-Abell et al., 2016). A closer structural comparison of two ATL isoforms (ATL1 and ATL3) indicates that despite differences in GTP-hydrolysis kinetics, the overall sequence of molecular events leading to ATL dimerization (and presumably membrane fusion) is conserved (O'Donnell et al., 2017). In both cases, monomeric ATL binds GTP, undergoes an intramolecular conformational change, and hydrolyzes GTP, which enables the sequential dimerization of the G and middle domains. Dimerization precedes phosphate release, and an intramolecular arginine residue displaces the catalytic magnesium allowing the dissociation of the

homodimer and the cycle to be reset (O'Donnell et al., 2017). The key components of ATL's cycling mechanism are impaired in mutant variants that are associated with neurological disorders, HSP and HSN, compromising the overall fidelity of the system (Guelly et al., 2011; Rismanchi et al., 2008; Ulengin et al., 2015).

There is an emerging theme that neurological disorders are caused or affected by defects in organelle structure and membrane trafficking, exemplified by HSP, HSN, and related neurodegenerative diseases (Blackstone et al., 2011). However, the underlying structural and functional principles often remain poorly understood. In the case of ATLs, part of the knowledge gap can be attributed to the lack of reoccurring mutations that would define residue-specific hotspots within the proteins. Overall, mutations appear family-specific and distribute across ATL's primary sequence (Byrnes and Sondermann, 2011; Fink, 2013). When mapped onto the three-dimensional structures of ATL, the majority of mutants cluster in or near the protein's active site or a region connecting the active site to an allosteric interface between the G and middle domains responsible for nucleotide loading (Bian et al., 2011; Byrnes et al., 2013; Byrnes and Sondermann, 2011). The majority of HSP/HSN mutations elicit dominant-negative phenotypes yet the mutations are buried within the folded protein, supporting the notion that the mutations' primary defects are intrinsic to ATLs. However, there is no unifying mechanistic model for how mutations effect ATL function as the disease variants impair nucleotide hydrolysis, protein oligomerization, or both (Bian et al., 2011; Byrnes and Sondermann, 2011; Ulengin et al., 2015). Unfortunately, characteristic defects often cannot be gleaned from their location in the protein's structure, and this lack of predictive power necessitates studies on individual mutants to elucidate

pathogenic mechanisms. Here, we biochemically characterize the HSP mutation $F^{151}S$ and show that despite being able to bind nucleotide, the enzyme is deficient in forming higher order oligomers in the presence of GTP or non-hydrolyzable GTP analogs. However, this HSP mutant can dimerize through G and middle domains when bound to GDP•$AlF_x$, a transition state analog. $F^{151}$ clusters with other HSP mutations but displays a unique structure-function profile. We propose that $F^{151}$ serves as a pivotal residue that couples ATL's nucleotide hydrolysis and conformational switching with the $F^{151}S$ mutation breaking this allosteric path. Additional structural information of mutants and the isolated G domain, all with varying capacities to dimerize, adds to our understanding of ATL's switching between pre- and post-hydrolysis states.

## RESULTS AND DISCUSSION

*The non-canonical HSP mutation $F^{151}S$ fails to hydrolyze GTP but retains nucleotide binding ability.*

When analyzed in the context of the soluble catalytic core fragment comprising ATL's G and middle domains, the majority of HSP mutations exhibit a modest reduction in GTPase activity and limited impairment of dimerization at equilibrium (Bian et al., 2011; Byrnes and Sondermann, 2011; Ulengin et al., 2015). Re-examination of how GTPase activity correlates to dimerization for previously characterized HSP mutations illustrates that nearly all mutants can efficiently dimerize when bound to transition state and non-hydrolyzable GTP analogs (GDP•$AlF_x$ and GppNHp, respectively) (**Figure 3.1A**) (Byrnes and Sondermann, 2011). The propensity to dimerize in the transition state is strong as indicated by mutant dimer fractions ranging between 89-100% (**Figure 3.1A; left**), and the non-hydrolyzable GTP analog shows similar dimerization potential ranging from 47-100% (**Figure 3.1A; right**). At the same time, mutations have a broader effect on GTPase activity ranging between 28-100% of wild-type activity (**Figure 3.1A**). Two exceptions are $Q^{191}R$ that retains GTPase activity but cannot dimerize when bound to GppNHp, and $R^{217}Q$ that cannot hydrolyze GTP or dimerize when in the presence of either GDP•$AlF_x$ or GppNHp (Byrnes and Sondermann, 2011) (**Figure 3.1A**). Effects of $Q^{191}R$ on ATL1's molecular mechanism have not been examined in greater detail and hence it is not clear how the apparent defect in oligomerization propensities manifests. In contrast, the cause of $R^{217}Q$'s negative effect on ATL function is obvious. The guanidinium group of $R^{217}$ directly contributes to the binding of the nucleotide by coordinating the guanine base; when mutated to glutamine,

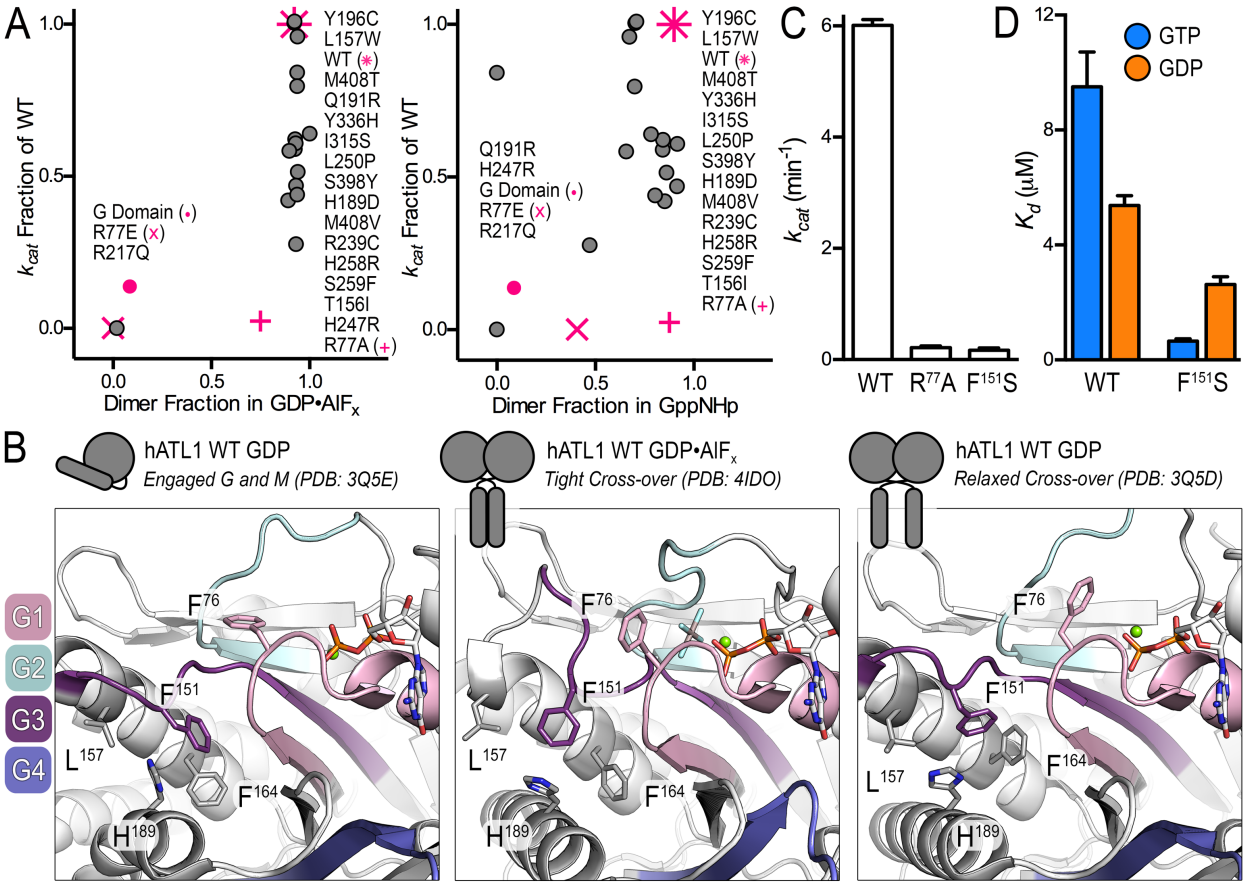


**Figure 3.1. The atypical HSP mutation, ATL1-F$^{151}$S, is catalytically deficient but retains ability to bind nucleotide. (A)** Re-evaluation of the correlation between GTPase activity and dimerization propensities of HSP mutations found in ATLs (*HSP mutations, gray dots; engineered mutations, pink*) (Byrnes and Sondermann, 2011). **(B)** The atypical ATL1-F$^{151}$S mutation is located between the active-site and intramolecular domain interface responsible for nucleotide loading. Switch regions are labeled (*G1, pink; G2, teal; G3, dark purple; G4, blue/purple*). **(C)** Turnover number ($k_{cat}$) of phosphate-release for wild-type, catalytically-deficient R$^{77}$A mutant, and F$^{151}$S. **(D)** Affinity of GTP and GDP for wild-type and F$^{151}$S ATLs were calculated using mant-nucleotides. Graphs showing means and standard error of the mean (SEM) are plotted from two biological replicates with three technical repeats each.

the affinity for nucleotide is lost (Byrnes and Sondermann, 2011). Similar to the $R^{217}Q$ mutant, engineered ATL variants such as $R^{77}E$, a charge reversal mutation of the catalytic arginine, and a truncated construct expressing the isolated G domain, both have impaired GTPase activity and cannot dimerize in GDP•$AlF_x$ (Bian et al., 2011; Byrnes and Sondermann, 2011) (**Figure 3.1A, pink x and •**). The loss of function for both $R^{77}E$ and the isolated G domain can be attributed to a decreased affinity for nucleotide (Bian et al., 2011; Byrnes et al., 2013). A more subtle mutation at the catalytic arginine finger, $R^{77}A$, renders the protein GTPase inactive despite preserving GDP and GTP binding with affinities comparable to wild-type enzyme; nevertheless, if left to equilibrate for extended period of time, the enzyme begins to exhibit the propensity to dimerize in GppNHp and GDP•$AlF_x$ (Byrnes et al., 2013) (**Figure 3.1A, pink +**). Overall, these mutational analyses show that even in cases where GTPase activity and nucleotide binding are compromised, ATLs are still able to oligomerize at equilibrium. At the same time, equilibrium oligomerization does not equate to proper function as cellular ATL function depends on coordinated, GTPase-driven conformational and quaternary structure changes (Liu et al., 2015; Powers et al., 2017).

Here we characterized the HSP mutant ATL1-$F^{151}S$, assessing its GTPase activity, nucleotide affinity, and oligomerization propensity. $F^{151}$ is located in G3/switch 2, positioned between the site of nucleotide hydrolysis and an intramolecular interface where the middle domain docks onto the G domain in a conformation that we previously identified as a requirement for nucleotide loading (Byrnes et al., 2013; Byrnes and Sondermann, 2011) (**Figure 3.1B**). The biochemical properties of ATL1-$F^{151}S$ indicate a deviation from trends presented by previously analyzed HSP and engineered mutants

(Bian et al., 2011; Byrnes and Sondermann, 2011; Ulengin et al., 2015) (**Figure 3.1A**), although $F^{151}S$ does present the same dominant-negative effect on ER morphology as other HSP mutations (Rismanchi et al., 2008; X. Zhao et al., 2001). In particular, ATL1-$F^{151}S$ was unable to hydrolyze GTP with a turnover number equivalent to the catalysis-deficient ATL1-$R^{77}A$ mutant, which is in agreement with previous reports (Bian et al., 2011) (**Figure 3.1C**). Notably, $F^{151}S$ confers one of the lowest GTPase rates of any HSP mutation that is not in direct contact with the nucleotide. Since the mutation is removed from the active-site, it was not surprising that ATL1-$F^{151}S$ retains the ability to bind both GTP and GDP, but it is curious that it does so at higher affinities than wild-type protein (**Figure 3.1D**).

*$F^{151}S$ dimerizes only when bound to the transition state analog at equilibrium.*

Considering that ATL1-$F^{151}S$ is catalytically-inactive but retains the ability to bind nucleotide (**Figure 3.1C and 3.1D**), we would predict that its dimerization profile would be similar to that of the $R^{77}A$ mutant (Byrnes et al., 2013). The oligomerization capability of ATL1-$F^{151}S$ was assessed upon incubating the protein with various nucleotides and nucleotide analogs and measuring the molecular weights of the protein-nucleotide mixtures using size exclusion chromatography-coupled multi-angle light scattering (SEC-MALS) (De et al., 2010). The wild-type ATL1 catalytic core exhibited nucleotide-dependent dimerization consistent with previous studies where nucleotide-free (apo) and GDP-bound proteins were monomeric with a molecular weight of 50 kDa and GppNHp and GDP•$AlF_x$ were dimeric with a molecular weight of 100 kDa (Byrnes and Sondermann, 2011; O'Donnell et al., 2017) (**Figure 3.2A**). ATL1 equilibrated with GTP

eluted as a monomer due to both substrate consumption and buffer exchange into the mobile phase which did not include GTP (**Figure 3.2A**). Analogous to wild-type protein, apo and GDP-bound species of ALT1-$F^{151}S$ eluted as monomers (**Figure 3.2B**). The light scattering chromatogram from GTP-bound ATL1-$F^{151}S$ displays two interesting signatures; the GTP-bound species elutes ~0.3 mL earlier and is band broadened by ~0.3 mL as determined from the difference between initial and final elution volumes at half maximal intensities when compared to other monomer SEC profiles from both wild-type and $F^{151}S$ (**Figure 3.2A and 3.2B**). Since the molecular weight is consistently monomeric across the peak, this observation suggests that $F^{151}S$ is able to undergo a specific conformational change when bound to GTP that does not occur in other protein-nucleotide complexes. We expected ATL1-$F^{151}S$ to dimerize in the presence of GppNHp due to the similar nucleotide binding abilities shared with $R^{77}A$ (Byrnes et al., 2013); however, ATL1-$F^{151}S$ remained predominantly monomeric with only a small population adopting a dimeric state (**Figure 3.2B**). In contrast to the GppNHp results, ATL1-$F^{151}S$ can fully dimerize when bound to GDP•$AlF_x$. This nucleotide-dependent dimerization profile makes ATL1-$F^{151}S$ unique and the only characterized HSP mutant protein that is deficient in catalytic cycling, unable to dimerize when bound to non-hydrolyzable GTP analog, but capable to dimerize with a transition state analog.

*$F^{151}S$ dimerizes through both G and middle domains when bound to GDP•$AlF_x$.*

SEC-MALS analysis reports on the absolute molecular weight of the species in solution but cannot discriminate between the relative orientation of the G and middle domains in dimeric assemblies. Using FRET-based approaches, we have previously

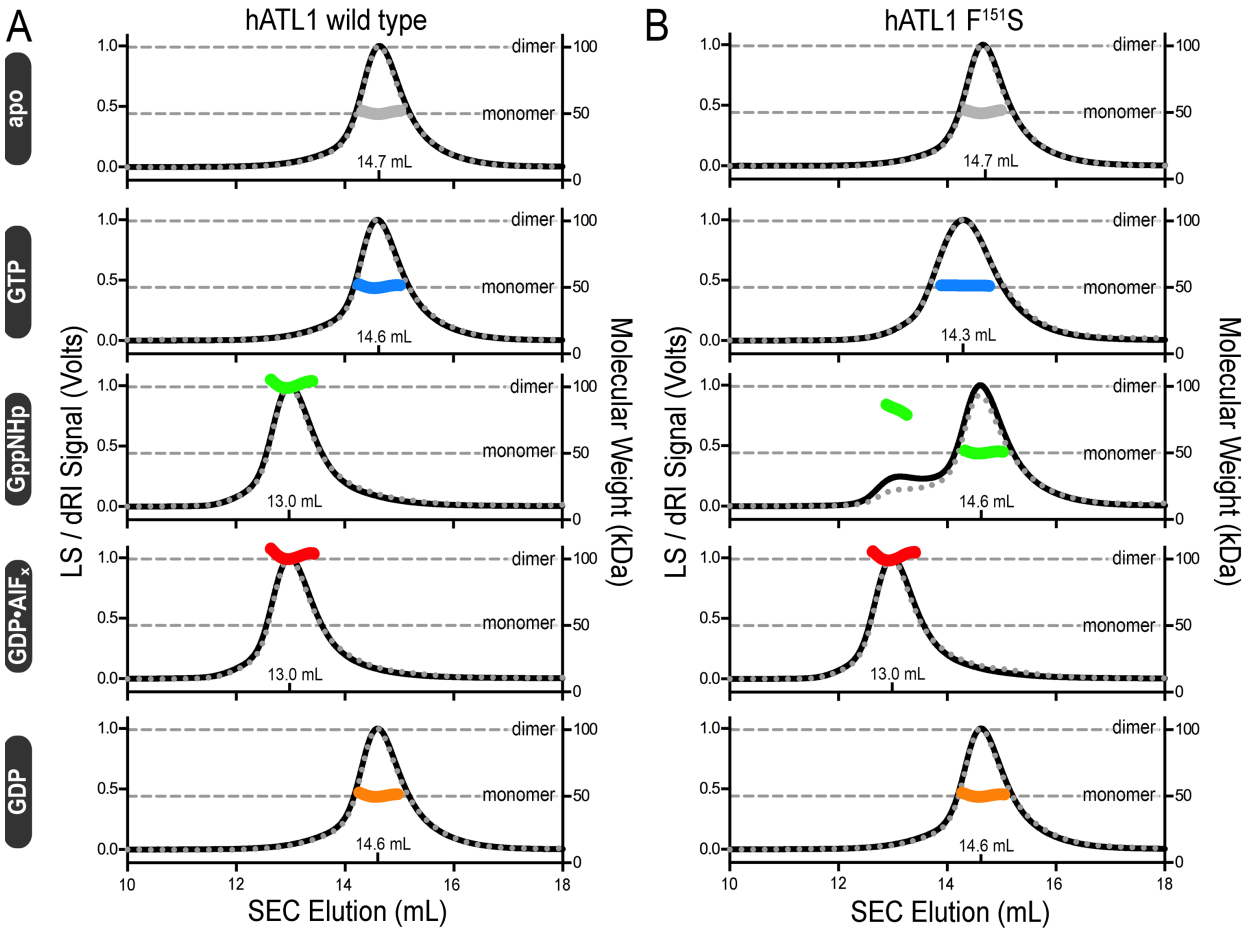


**Figure 3.2. Molecular weight determination indicates the ATL-F$^{151}$S only dimerizes when bound to the transition state analog, GDP•AlF$_x$. (A)** Absolute molecular weights (colored data points across elution peaks) of wild-type ATL catalytic core fragment (injection: 40 $\mu$M ± 1 mM nucleotide) were determined using SEC-MALS (90°-light scattering black solid; refractive index signal, gray dotted; theoretical monomer and dimer molecular weights, horizontal gray dashed lines). Wild-type enzyme samples the canonical monomer/dimer states previously described (Byrnes et al., 2013; O'Donnell et al., 2017). **(B)** The equivalent ATL1-F$^{151}$S construct using the same experimental conditions only fully dimerizes when bound to GDP•AlF$_x$ and the GTP bound species has a band-broadened SEC profile that elutes earlier than other similar samples.

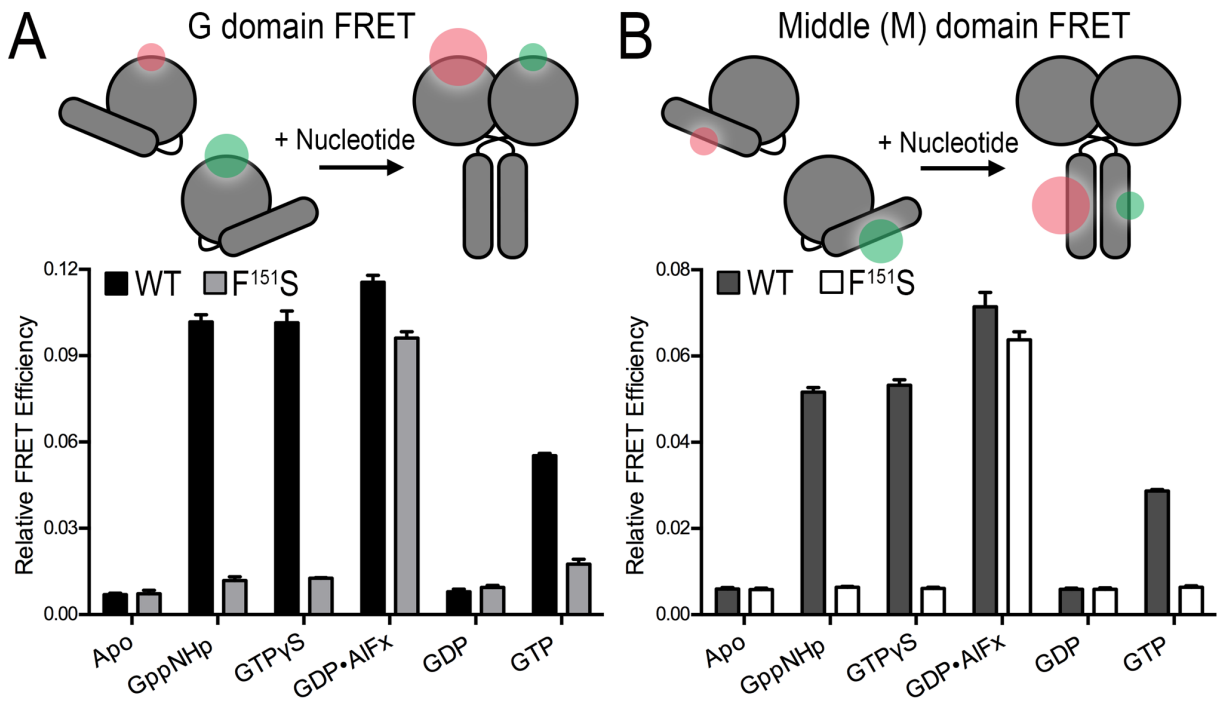


**Figure 3.3. ATL1-F$^{151}$S utilizes both the G and middle domains in transition state dimer.** **(A)** Equilibrium and steady state G domain FRET dimerization. Both wild-type and F$^{151}$S proteins were labeled site-specifically with donor and acceptor FRET fluorophores and measurements including 1 $\mu$M protein and 500 $\mu$M nucleotide were taken once equilibrium or steady state conditions were fulfilled. **(B)** Equilibrium and steady state G domain FRET dimerization. Analogous FRET measurements were conducted with wild-type and F$^{151}$S proteins labeled site-specifically at their middle-domains. Graphs showing means and standard deviation (SD) are plotted from two biological replicates with three technical repeats each.

shown that ATLs proceed through a series of conformational changes where dimerization of the G and middle domains occurs in close succession (O'Donnell et al., 2017). To determine the conformations ATL1-F$^{151}$S is able to adopt, we used the same FRET sensors to differentiate between G and middle domain dimerization (**Figure 3.3**). In short, engineered surface exposed cysteine residues were incorporated into the G or middle domains and labeled with small organic donor or acceptor fluorophore (Byrnes et al., 2013; O'Donnell et al., 2017; Chapter 2) (**Figures 3.3A and 3.3B, top**). Equilibrium FRET efficiencies in the presence of various nucleotides were calculated for ATL1 wild-

type and the corresponding $F^{151}S$ variant; the duration required to reach equilibrium was determined via kinetic time-courses (*data not shown*). Similar to previous publications, the G and middle domains of ATL1 wild-type form homodimers in the presence of GppNHp, GTPγS, and GDP•$AlF_x$ while the enzyme remains monomeric when bound to GDP or in the absence of nucleotide (Byrnes et al., 2013; O'Donnell et al., 2017) (**Figure 3.3A and 3.3B**). In agreement with the SEC-MALS molecular weight determination, the ATL1-$F^{151}S$ catalytic core fragment is unable to dimerize with non-hydrolyzable nucleotides but can form G and middle domain homodimers when bound to GDP•$AlF_x$. Since the middle domain FRET efficiency for ATL1-$F^{151}S$ bound to GDP•$AlF_x$ is greater than wild-type bound to non-hydrolyzable analogs, we can conclude that the mutant is competent in forming the high-affinity transition state dimer (Liu et al., 2015; O'Donnell et al., 2017) (**Figure 3.3B**).

*Structural characterization of ATL1 variants with diverse dimerization capacities.*

GTPase-driven dimerization is crucial for ATL function. Previous studies shed light on the dimer conformations ATLs sample (Bian et al., 2011; Byrnes et al., 2013; Byrnes and Sondermann, 2011; O'Donnell et al., 2017; Saini et al., 2014; Winsor et al., 2017), but the conformation of the monomeric states are less well defined. Here, we determined crystal structures of ATL1 mutants $R^{77}A$, $R^{77}A/F^{151}S$, and $F^{151}S$, all of which display distinct oligomerization propensities. We also crystallized the isolated G domain in the presence of GDP•$Mg^{2+}$ as another reference model for a catalytic- and dimerization-incompetent state. The G domain fails to dimerize in any nucleotide since it cannot adopt the GTP-loading-competent state (Byrnes et al., 2013). A structure for the

isolated G domain of ATL1 (residues 1-339) was solved in space group $F2_3$, containing four molecules per asymmetric unit, at a maximum resolution of 3.0 Å (**Table 3.1**). The four GDP•$Mg^{2+}$-bound promoters assemble into two identical dimers via a G domain dimer interface seen in previous publications, GDP•$Mg^{2+}$-bound ATL structures, despite the protein's inability to oligomerize in solution (Bian et al., 2011; Byrnes et al., 2013; Byrnes and Sondermann, 2011; O'Donnell et al., 2017; Wu et al., 2015) (**Figure 3.4A**). One key feature of this structure is the the configuration of the fourth α-helix (α4) of the G domain fold, which is straight. Based on previous ATL1 structures, this helix can adopt two principal configurations, straight and bent (Bian et al., 2011; Byrnes and Sondermann, 2011; O'Donnell et al., 2017; Wu et al., 2015) (**Figure 3.4B; left**). When bent, G and middle domains are engaged and this interaction enables GTP loading of the G domain (Byrnes et al., 2013). GTP-binding is followed by an intramolecular conformational change that is thought to represent the release of the G and middle domains (O'Donnell et al., 2017). The straightening of helix α4 is one potential mechanism for the kick-off of the middle domain. In conclusion, the structure of the isolated G domain represents a GTPase-cycling incompetent state and provides further structural evidence that helix α4 bending requires middle domain docking, which is associated with GTP binding (**Figure 3.4B; right**). Of note, $F^{151}$ is resolved in the isolated G domain structure. The residue shares the same conformation and environment as seen in a crystallographic state of ATLs bound to GDP•$Mg^{2+}$, where the middle domain is dislodged from the G domain, and G and middle domains form weak homodimers with a adjacent promoter in the crystal lattice. We refer to this conformation

**Table 3.1: X-ray data collection and refinement statistics.**

| | ATL1 $R^{77}A$ $Mg^{2+}$, GDP 1-446 | ATL1 $R^{77}A/F^{151}S$ $Mg^{2+}$, GDP 1-446 | ATL1 $F^{151}S$ $Mg^{2+}$, GDP•$AlF_x$ 1-446 | $ATL1^G$ $Mg^{2+}$, GDP 1-339 |
|---|---|---|---|---|
| **Data Collection** | | | | |
| X-ray source | CHESS | CHESS | CHESS | CHESS |
| Wavelength | 0.9759 | 0.6314 | 0.9770 | 0.9759 |
| Space group | P1 | P1 | P 21 21 21 | F 2 3 |
| Unit cell | | | | |
| a, b, c (Å) | 51.1, 68.4, 75.9 | 52.1, 68.1, 76.0 | 49.6, 115.7, 184.3 | 308.0, 308.0, 308.0 |
| α, β, γ (°) | 117.0, 89.8, 99.0 | 116.9, 90.8, 98.5 | 90, 90, 90 | 90, 90, 90 |
| Resolution (Å)[a] | 42.36 - 1.95 (2.06 - 1.95) | 42.75 - 1.99 (2.10 - 1.99) | 49.0 - 1.90 (2.00 - 1.90) | 48.70 - 3.00 (3.16 - 3.00) |
| Number of Reflections | | | | |
| Total | 153067 (22418) | 117856 (15186) | 571474 (55219) | 1229123 (177115) |
| Unique | 63315 (9210) | 60236 (7994) | 83775 (11190) | 48244 (7006) |
| Completeness (%) | 96.4 (96.2) | 95.7 (86.9) | 98.8 (92.6) | 99.9 (99.8) |
| Multiplicity | 2.4 (2.4) | 2.0 (1.9) | 6.8 (4.9) | 25.5 (25.3) |
| I/σ(I) | 7.1 (2.1) | 9.9 (1.5) | 10.7 (1.3) | 22.8 (3.0) |
| $R_{meas}$ (%) | 10.3 (56.0) | 8.6 (85.7) | 12.9 (137.3) | 20.1 (145.5) |
| $R_{merge}$ (%) | 7.9 (43.0) | 6.4 (63.4) | 11.9 (123.5) | 19.7 (142.6) |
| CC1/2 | 0.991 (0.784) | 0.996 (0.598) | 0.997 (0.419) | 0.999 (0.847) |
| **Refinement** | | | | |
| $R_{work}$ / $R_{free}$ (%) | 20.5 / 23.9 | 20.3 / 24.4 | 17.8 / 22.2 | 17.0 / 20.5 |
| rms deviations | | | | |
| Bond length (Å) | 0.007 | 0.009 | 0.007 | 0.002 |
| Bond angles (°) | 0.929 | 0.973 | 0.865 | 0.534 |
| No. of atoms | | | | |
| Protein | 5872 | 6088 | 6660 | 9730 |
| Ligands | 94 | 63 | 116 | 116 |
| Water | 281 | 198 | 557 | 92 |
| Ave B-factors (Å$^2$) | | | | |
| Protein (total) | 43.3 | 44.3 | 35.3 | 68.0 |
| Ligands | 40.83 | 54.8 | 33.2 | 49.7 |
| Water | 44.0 | 38.8 | 42.4 | 52.9 |
| Ramachandran (%) | | | | |
| Favored | 97.7 | 98.0 | 98.2 | 96.4 |
| Outliers | 0 | 0 | 0 | 0 |
| PDB Code: | 6B9D | 6B9E | 6B9F | 6B9G |

(a) Values in brackets are fore the highest resolution bin.

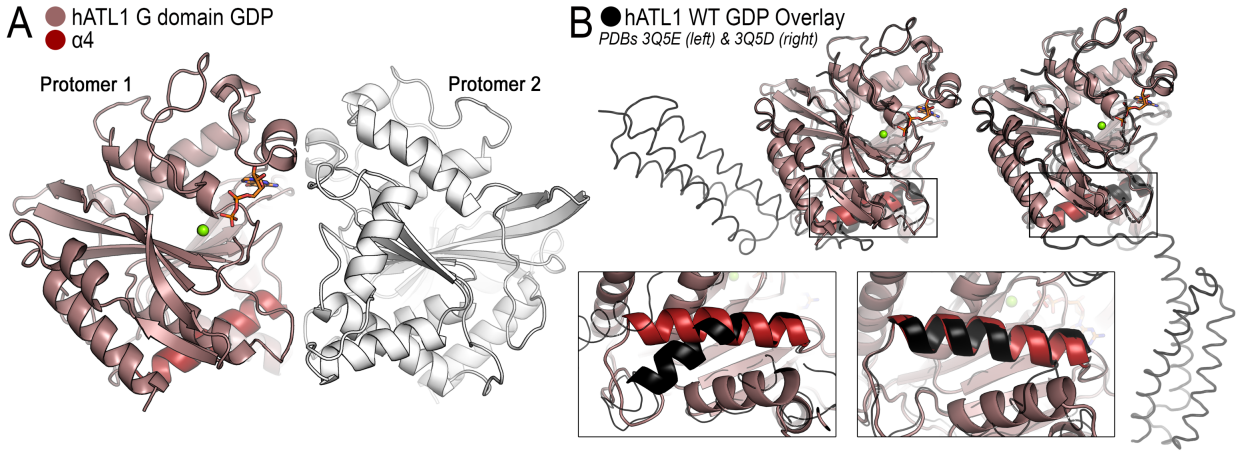


**Figure 3.4. Crystal structure of the isolated G domain of ATL1 bound to GDP•$Mg^{2+}$. (A)** G domain structure displays weak crystal packing interactions that involve switch regions. The G domain (*colored salmon*), helix α-4 (*red*), and a second protomer (*white*) are illustrated. **(B)** Comparison of the isolated G domain with either the engaged (*PDB: 3Q5E; left*) or relaxed cross-over (*PDB: 3Q5D; right*) structures (*both black*) indicates that helix α-4 is straight.

as the relaxed cross-over state, which is thought to represent a post-hydrolysis dimer (Bian et al., 2011; Byrnes and Sondermann, 2011).

One caveat with previous structural studies of ATL, including the isolated G domain above, stems from a preferred crystal packing interaction where the G domains of two molecules form a loose dimer even when the protein is bound to GDP•$Mg^{2+}$ (Bian et al., 2011; Byrnes et al., 2013; O'Donnell et al., 2017; Wu et al., 2015). This conformation is reminiscent of the tight dimer observed in the transition state and involves the switch regions (G1-G4) of the G domains, but has a smaller interfacial area than the transition state (Byrnes et al., 2013). On the other hand, in solution, GDP•$Mg^{2+}$ does not support protein dimerization (Byrnes et al., 2013; Morin-Leisk et al., 2011; O'Donnell et al., 2017) (**Figures 3.2 and 3.3**), and hence the corresponding structures may not portray the solution conformations accurately. Here, we developed a strategy to capture the structure of GDP•$Mg^{2+}$-bound ATL1 with monomeric G domains by mutating

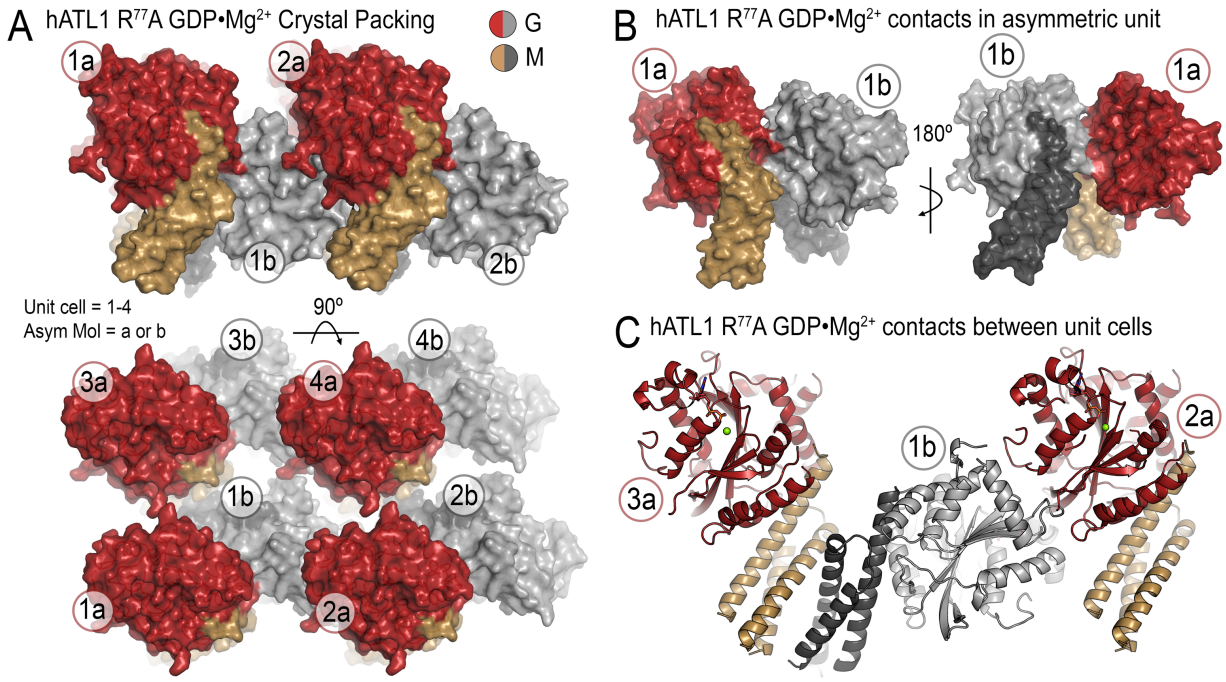


**Figure 3.5. Novel ATL crystal packing and asymmetric contents of crystals containing ATL1-R$^{77}$A bound to GDP•Mg$^{2+}$. (A)** Schematic of crystal packing and contacts made in in the ATL1-R$^{77}$A structure. Two protomers exist in a unit cell and their G domains are colored either red / light gray and middle domains are colored tan / dark gray. Each protomer is labeled by a unit cell number and letter corresponding to its position asymmetric unit. **(B)** Asymmetric unit contents illustrate a novel contact between protomers. **(C)** Contacts made between unit cells consist of middle domain mediated (molecules 3a and 1b) and G domain mediated (molecules 1b and 2a).

R$^{77}$, a residue that forms a salt bridge with E$^{224}$ from an adjacent G domain in all GDP-bound crystal structures determined to date. Using crystals that diffracted X-rays to 1.95 Å, we were able to determine the structure of ATL1-R$^{77}$A (residues 1-446) bound to GDP•Mg$^{2+}$. The structure was solved by molecular replacement in space group P1 with two molecules in the asymmetric unit (**Table 3.1**). The R$^{77}$A mutation led to novel crystal packing contacts within the asymmetric unit and between unit cells that differ from those described previously (**Figure 3.5A**). Within the asymmetric unit (**Figure 3.5B; molecules 1a and 1b**), protomers have an average interface area of 491 Å$^2$, and

between unit cells, the G domains (**Figure 3.5C; molecules 1b and 2a**) have an interface area of 969 Å$^2$ and middle domains (**Figure 3.5C; molecules 3a and 1b**) have an interface area of 576 Å$^2$. However, none of these interfaces have been predicted to be biologically relevant (Krissinel and Henrick, 2007), and they do not involve the G domain's switch regions or active site (**Figure 3.5**). As a result of these new packing interactions, the switch regions are free to move and consequently disordered, consistent with the conformations observed for other G proteins bound to GDP (Vetter, 2014) (**Figure 3.6A**). The loop containing the mutated catalytic-arginine is resolved and the alanine occupies the same conformation as seen in the wild type structure (*PDB: 3Q5E*) (**Figure 3.6A; inset**). Based on the structural changes, we propose that this structure represents the pre-hydrolysis, monomeric form of ATL1.

In order to attain a monomeric form of ATL-F$^{151}$S, we paired the HSP mutation with R$^{77}$A and determined the structure of ATL1-R$^{77}$A/F$^{151}$S bound to GDP•Mg$^{2+}$ in space group P1 with two molecules in each asymmetric unit (**Table 3.1**). Globally, ATL1-R$^{77}$A/F$^{151}$S adopts the same crystal packing and contacts as found in GDP•Mg$^{2+}$-bound ATL1-R$^{77}$A bound to GDP•Mg$^{2+}$ (**Figure 3.7**). Unfortunately, the F$^{151}$S mutation was located on a flexible loop of the G3 region (switch 2) and could not be resolved; the presumed location of the mutation is indicated (**Figure 3.6B; pink halo**). Despite the high degree of similarity between structures (RMSD = 0.25Å), the ATL1-R$^{77}$A/F$^{151}$S structure has fewer disordered loops than R$^{77}$A which may be due to the addition of the F$^{151}$S mutation (**Figure 3.6B**). Interestingly, the guanine cap in ATL1-R$^{77}$A/F$^{151}$S adopts an open conformation, and the overlay with all other crystal forms (*i.e.* G/M-engaged; transition state; relaxed-crossover) indicates that the guanine cap and the resolved

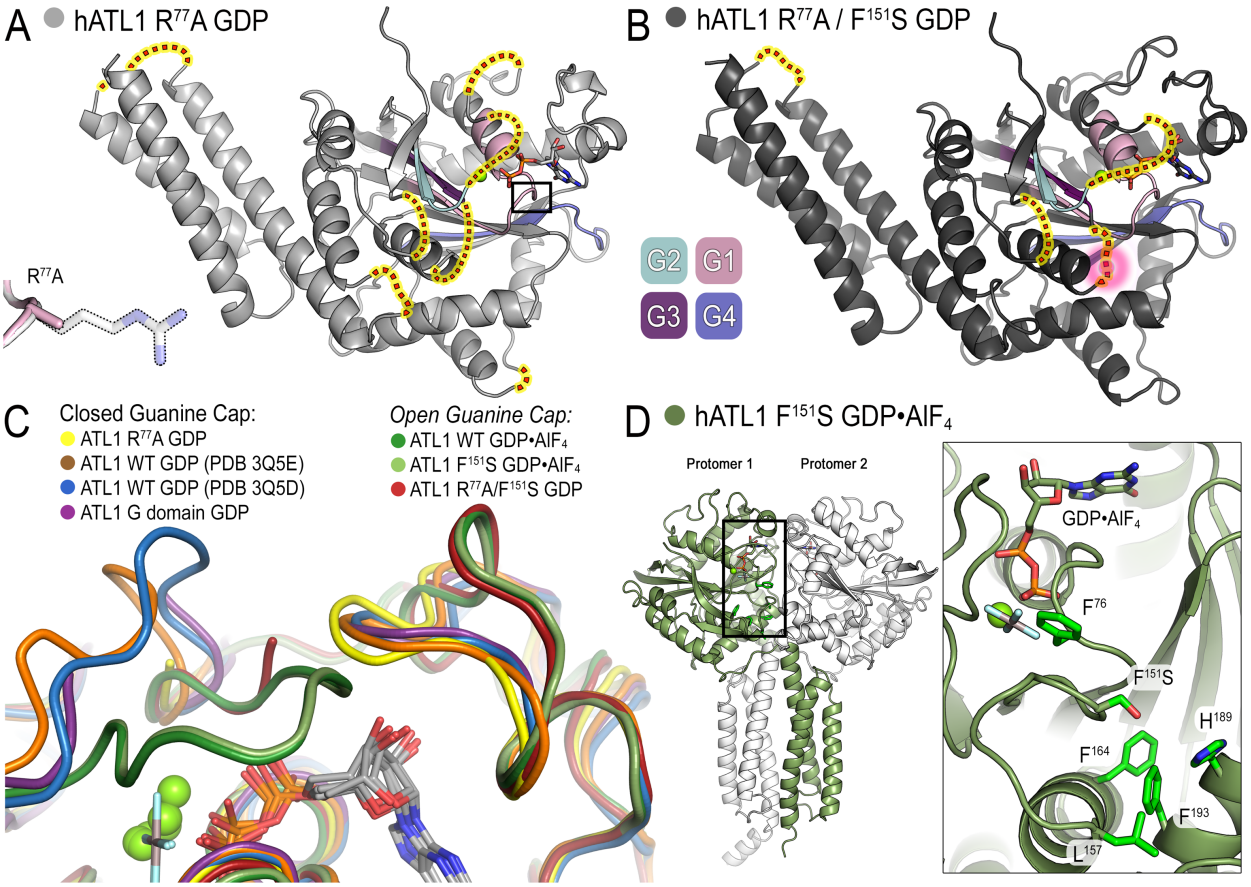


**Figure 3.6. Structures of ATL1 mutants have diverse dimerization capacities and guanine cap configuration. (A)** ATL1-R$^{77}$A bound to GDP•Mg$^{2+}$ (gray) exists in a monomeric state with G and middle domains engaged. Switch regions (*G1, pink; G2, teal; G3, dark purple; G4, blue/purple*) are largely disordered and their hypothetical locations are included (*red dots highlighted yellow*). Inset shows alpha-carbon backbone of loop containing R$^{77}$A is not perturbed. **(B)** ATL1-R$^{77}$A/F$^{151}$S bound to GDP•Mg$^{2+}$ (gray) also exists in a monomeric state with G and middle domains engaged. Switch regions (*G1, pink; G2, teal; G3, dark purple; G4, blue/purple*) are more ordered and the ATL1-R$^{77}$A structure and their hypothetical locations are included (*red dots highlighted yellow*). The F$^{151}$S mutation is part of the G3 switch region and is disorder; hypothetical location of the mutation is outlined in a pink halo. **(C)** Various crystal structures are aligned to observe the position of the guanine cap. The ATL1 R$^{77}$A structure (yellow) had this loop closed onto the guanine base like other GDP•Mg$^{2+}$ bound structures (*brown, blue, purple*). However, the both the ATL1 R$^{77}$A/F$^{151}$S GDP bound (*red*) and the ATL1 F$^{151}$S GDP•AlFx (*light green*) bound structures mirror the wild-type transition state structure (*PDB: 4IDO, dark green*) and have a retracted guanine cap. **(D)** ATL1-F$^{151}$S bound to GDP•AlF$_x$ (protomer 1, green; protomer 2, white) is fully capable of equilibrating into the high affinity transition state despite the F$^{151}$S mutation buried within the core of the enzyme.

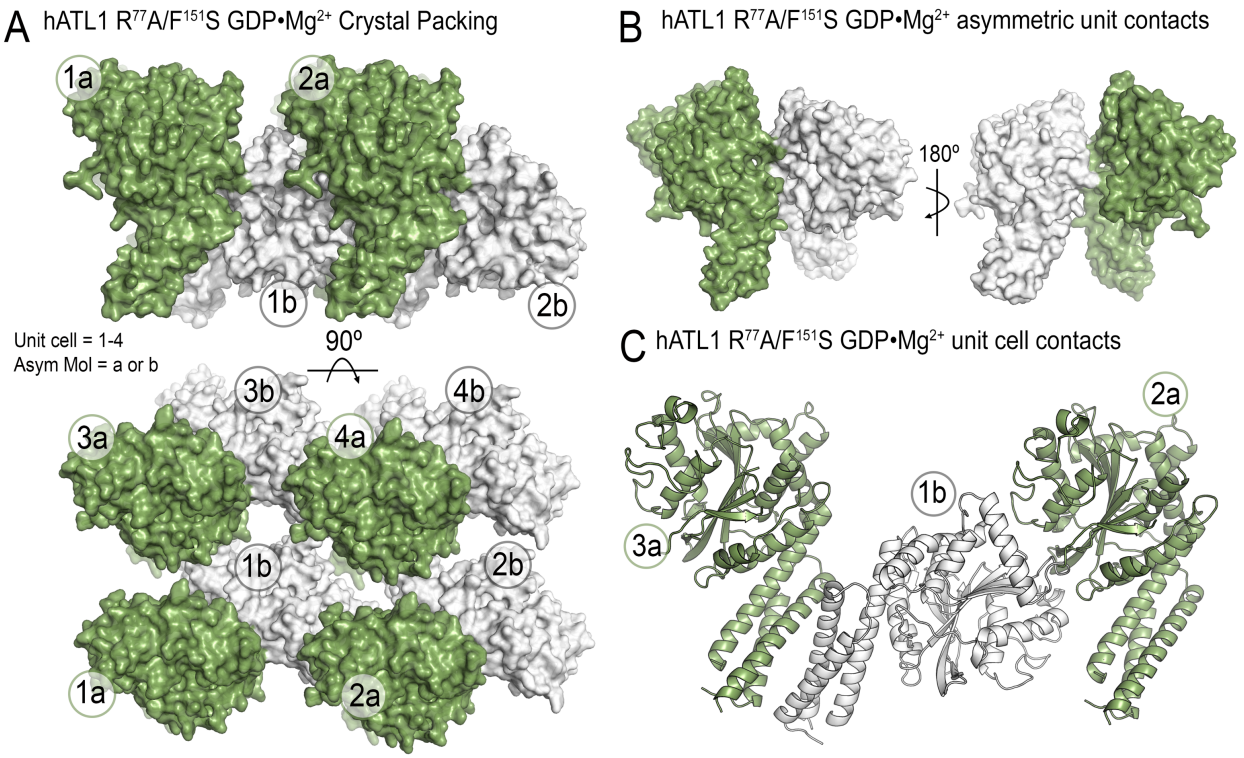


**Figure 3.7. Crystals containing ATL1-R$^{77}$A/F$^{151}$S bound to GDP•Mg$^{2+}$ exhibit same crystal packing and asymmetric contents as seen for the ATL1-R$^{77}$A structure. (A)** Crystal packing is the same as ATL1-R$^{77}$A structure, each protomer is labeled by a unit cell number and letter corresponding to its position asymmetric unit, and colored either green or white. **(B)** Asymmetric unit contents mirrors the ATL1-R$^{77}$A structure. **(C)** Crystal contacts made between unit cells is also consistent with ATL1-R$^{77}$A structure.

portion of G2 mirrors the transition state form of ATL (**Figure 3.6C**). In contrast, ATL1-R$^{77}$A adopts a conformation more similar to all other non-transition state structures (**Figure 3.6C**).

We were also able to attain the transition state structure of ATL1-F$^{151}$S with crystals diffracting X-rays to 1.9 Å. phasing by molecular replacement and subsequent refinement in space group $P2_12_12_1$ yielded the final model with two molecules per asymmetric unit (**Table 3.1** and **Figure 3.6D**). Despite including a non-conservative mutation in the buried core of the G domain, the structure is well-resolved and displays

the anticipated change in electron density at position 151, ATL1-$F^{151}S$ bound to GDP•$AlF_4$ is virtually identical to the synonymous wild-type transition state structure (*PDB: 4IDO*) with an RMSD of 0.22Å (**Figure 3.6D**) (Byrnes et al., 2013). This structure indicates that the $F^{151}S$ mutation is fully capable of equilibrating into the high affinity transition state but is unable to reach this energetic state with the endogenous substrate GTP.

## CONCLUDING DISCUSSION

Here, we characterized the atypical HSP mutation ATL1-$F^{151}S$ that is deficient in GTP-hydrolysis, cannot dimerize when bound to GTP or non-hydrolyzable analogs, but retains the ability to bind nucleotides and to dimerize through the G and middle domains when bound to a transition state analog. Mechanistically, this implicates $F^{151}$ in reducing the activation energy required for GTP-hydrolysis and/or inter-domain allostery linking nucleotide hydrolysis and middle domain engagement. Structural comparisons suggest a model where $F^{151}$ represents the central residue that couples intramolecular domains for allosteric communication (**Figure 3.8**). Crystal structures of various states elucidate a hydrophobic tract that links the active-site to helix α4, a motif that transitions from bent to straight during GTP-hydrolysis and the intramolecular release of G and middle domains. A structural comparison indicates that a hydrophobic tract begins with $F^{76}$ of the G1/P-loop, a residue that is adjacent to the catalytic arginine ($R^{77}$) and thought to sense the gamma-phosphate moiety. In the engaged, monomeric $R^{77}A$ structure, this side-chain is disordered but is resolved in the $R^{77}A/F^{151}S$ structure where it points toward the bound GDP (**Figure 3.8A)**. Weak crystal packing interactions that involve the G domain and its switch regions (*PDB: 3Q5E*) allow $F^{76}$ to rotate outwards, which in a monomeric ATL could represent the nucleotide loading state (**Figure 3.8B)**. In the presence of a nucleotide with gamma-phosphate or a transition state analog, $F^{76}$ moves outward in concert with a major reorientations of the switch regions that stabilize the phosphate moieties and align $R^{77}$ for nucleophilic attack (**Figure 3.8C**) (Byrnes et al., 2013). In the post-hydrolysis states, $F^{76}$ may return to the configuration seen in the

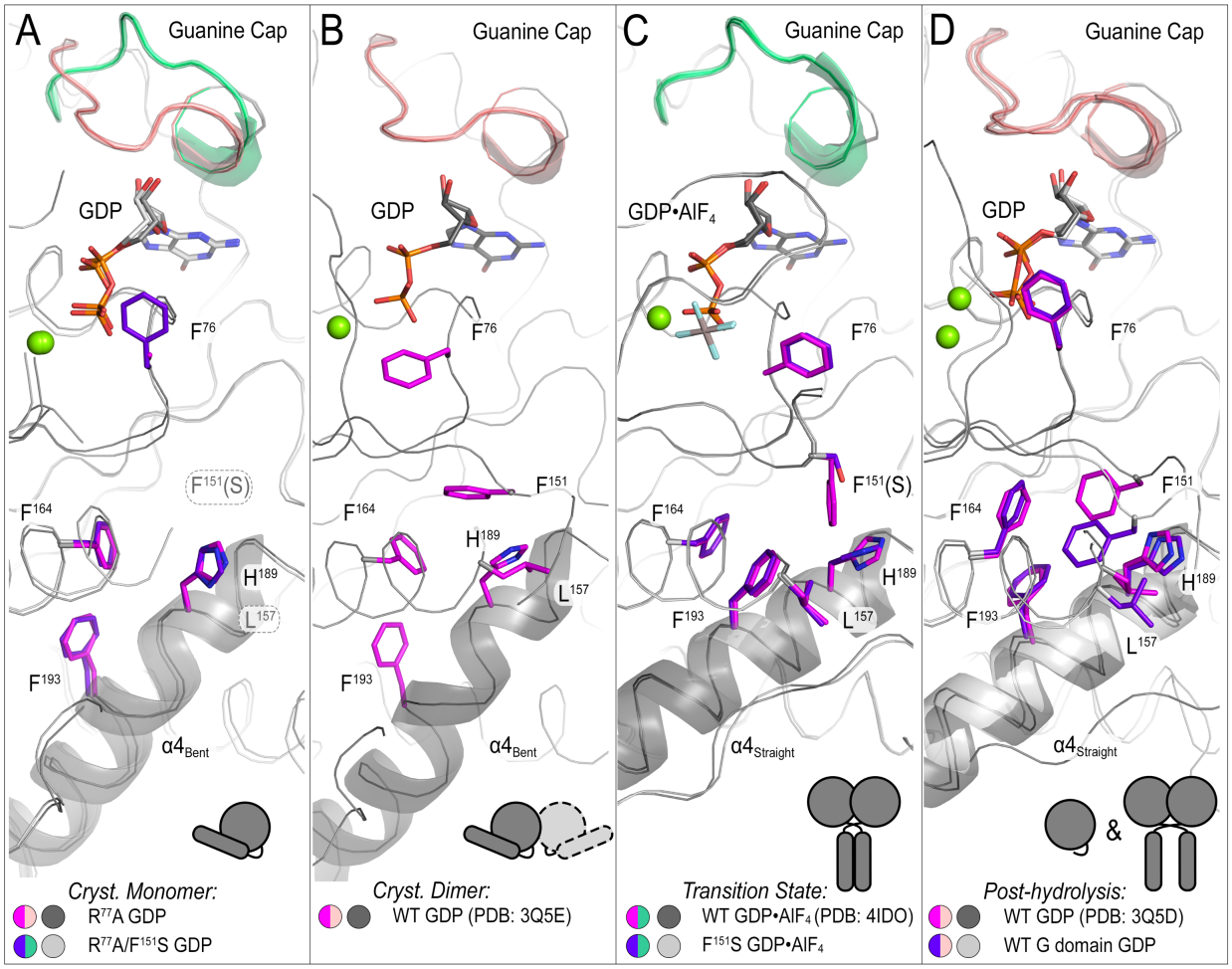


**Figure 3.8. Structure based model for a hydrophobic interaction network that establishes inter-domain allostery.** Hydrophobic residues connect the active-site (*GDP, white/black; guanine cap, green/salmon*) to helix α-4 (*cartoon helix*). **(A)** Structures depicting crystallographic monomers ($R^{77}A$, pink/dark gray; $R^{77}A/F^{151}S$, purple/light gray) are flexible with $F^{76}$ (in $R^{77}A$ structure), $F^{151}S$, and $L^{157}$ being disordered and helix α-4 bent. **(B)** When switch regions are stabilized via crystallographic dimer, the G/middle domain engaged structure (3Q5E, pink/dark gray) is more ordered with $F^{76}$ rotating away from the nucleotide and $F^{151}$ being resolved. **(C)** Both wild-type (pink/dark gray) and $F^{151}S$ (purple/ light gray) transition state structures exhibit a switch reorganization that is accompanied with a downward rotation of $F^{151}$ that pushes agains $H^{189}$ and $L^{157}$. The helix α-4 becomes straight and $F^{193}$, which is located at the helix's bend and may contribute energetic for helix straightening, rotates to form hydrophobic interactions with the the other labeled residues. **(D)** Structures resembling the post-hydrolysis state (*3Q5D, pink/dark gray; isolated G domain, purple/light gray*) exhibit a configuration that is en route to resetting the cycle. The helix α-4 remains straight and up stream residues ($F^{76}$ and $F^{193}$) begin to take on conformations seen in Panel A.

engaged monomeric structures, which may aid phosphate release and recycling the enzymatic cycle (**Figure 3.8D**).

$F^{76}$ is proximate to $F^{151}$, the site of the HSP disease mutation investigated above. $F^{151}$ adopts a number of conformations when comparing the various crystallographic states and is not resolved in the monomeric, engaged structures where the switch regions are largely disordered (**Figure 3.8A**). During the large reorganization of the switch regions leading to the conformation depicted in the transition state crystal structures, $F^{151}$ transitions from interacting with a single hydrophobic residue ($F^{163}$) to an environment that is highly hydrophobic. As $F^{151}$ rotates away from the active-site, it pushes against $L^{157}$ and the helix α4 located $H^{189}$ (**Figures 3.8B-3.8C**). Pushing against these residues causes a rotation of helix α4, which enables/results in its straightening. The straightening of helix α4 also involves $F^{193}$ which is located at helix α4's bend; this residue rotates to interact with the newly formed cluster of hydrophobic residues ($F^{151}$, $L^{157}$, $F^{163}$, and $H^{189}$) and may provide energetics for the molecular rearrangement (**Figure 3.8C**). It should also be noted this structural mechanism is not limited to an active-site outward relay for the GTPase-driven release of the G and middle domains, but is most likely bi-directional based on observations that the G/middle domain interface is required for nucleotide loading (Byrnes et al., 2013; O'Donnell et al., 2017).

The two $F^{151}$S-containing crystal structures establish that the mutant proteins sample the beginning and end states of the mechanism we propose above (**Figure 3.8A and 3.8C**). Additional support that $F^{151}$ is intimately linked to characteristics of the transition state is illustrated in the position of the guanine cap in the ATL1-$R^{77}$A/$F^{151}$S (G/middle-engaged) structure (**Figure 3.6C**). When this particular site is perturbed, the

protein exhibits an open conformation of the guanine cap that was previously reserved for structures adopting the tight cross-over dimer, e.g the transition state structure (Byrnes et al., 2013). The guanine cap is not stabilized through crystal packing in either ATL1-$R^{77}A$ or ATL1-$R^{77}A/F^{151}S$ structures, indicating the side chain identity at position 151 as the intrinsic reason for the apparent differences in ATL conformation and/or dynamics observed in the crystal structures. Notably, two residues that $F^{151}$ interacts with ($L^{157}$ and $H^{189}$) are both HSP disease mutants (Smith et al., 2009). Biochemical characterization of the corresponding disease variants, ATL1-$L^{157}W$ and ATL1-$H^{189}D$, indicates they are both catalytically active and able to fully dimerize when bound to either GppNHp or GDP•$AlF_x$ (**Figure 3.1A**) (Byrnes and Sondermann, 2011). This difference in mutant protein switching and activity argues that $F^{151}$ is a central residue responsible for the allosteric coupling between the active-site and intramolecular interface where the middle domain docks onto the G domains and regulates nucleotide binding, hydrolysis, and conformational changes.

In conclusion, the study of a disease-causing mutation in ATL1 revealed a pivotal intrinsic interaction network that couples the enzyme's active-site to the interface between G and middle domains. Perturbation at position $F^{151}$ affects bi-directional regulation across this allosteric network, whereas mutations at its periphery preserve core functionality and elicit more subtle effects. Despite the range of biochemical differences, disease-associated alleles of ATL confer equivalent aberrant ER phenotypes, suggesting that ATL fidelity is finely tuned for it function in cells.

## MATERIALS AND METHODS

*Phosphate-release kinetics.*

The release of free phosphate was detected using Enzchek Phosphate Assay Kit and the manufacturers protocol (Molecular Probes, Eugene OR) with the exception of the addition of 100 mM NaCl to the reaction buffer. Reactions consisted of 100 µL volume, 1 µM enzyme, and 500 µM GTP (Thermo Fisher Scientific, Waltham MA) in half area 96-well plates (Corning Inc. Corning NY) at 25ºC. Data were recorded at an absorbance of 366 nm using a BioTek Synergy II plate reader and the initial rate prior to 10% substrate conversion was fit to a linear regression and converted to units of µM/ min using a standard curve. Turnover number is defined as $k_{cat}$ = V / [Enzyme].

*Determination of dissociation constants with N-Methylanthraniloyl (mant)-nucleotides.*

On and off rates were determined from mant-nucleotide binding experiments and used to calculate a dissociation constants for mant-GDP and mant-GTP (Thermo Fisher Scientific, Waltham MA). A KinTek SF-2004 stopped-flow was used to rapidly mix mant-nucleotides and ATL to a final concentration of 2.5 µM nucleotide and increasing amounts of ATL (5-20 µM) at 25ºC. Samples were excited at 366 nm and signal from emission filter HQ460/40M (Chroma Technology Corp, Rockingham VT) was collected. Data were fit to exponential association equations and the rate constants were plotted versus ATL concentration; the resulting slope of the linear fit corresponds to $k_{on}$. $k_{off}$ was directly measured by preloading ATL with mant-nucleotide and chasing with high concentration of nucleotide to yield final concentrations of 2.5 µM ATL•mant-nucleotide and 2.5 mM unlabeled nucleotide. The resulting data were fit to a single exponential

decay curve where the observed rate constant corresponds to $k_{off}$. Dissociation constants ($K_d$) were calculated as $k_{off} / k_{on}$.

*Size-Exclusion Chromatography Coupled to Multi-Angle Light Scattering.*

Protein-nucleotide mixtures (40 μM ATL and 1 mM nucleotide) were injected onto a Superdex 200 Increase 10/300 column (GE Healthcare, Little Chalfont, UK), equilibrated with 25 mM HEPES pH 7.5, 100 mM NaCl, 4 mM MgCl2, and 2 mM EGTA. The GDP•$AlF_x$ sample was supplemented with 2 mM aluminum chloride and 20 mM sodium fluoride. Prior to injection, protein-nucleotide mixtures were incubated for a minimum of 1 hour. The gel filtration column was coupled to a static 18-angle light scattering detector (DAWN HELEOS-II) and a refractive index detector (Optilab T-rEX) (Wyatt Technology, Goleta, CA). Data were collected every second at a flow rate of 0.7 ml/min. Data analysis was carried out using ASTRA VI, yielding the molar mass and mass distribution (polydispersity) of the sample. The monomeric fraction of BSA (Sigma, St. Louis, MO; 5 mg/mL) was used to normalize of the light scattering detectors and used as a positive quality control.

*Dye Labeling and FRET measurements.*

Site-specific dye labeling was achieved by replacing non-conserved surface amino acids with cysteine residues within the G or middle domains. To maintain singly labeled protein, a surface exposed cysteine residue ($C^{375}A$) was replaced with an alanine residue. Labeling was conducted at 100 μM protein, 150 μM AlexaFluor-488 or AlexaFluor-647 (Molecular Probes, Eugene, OR), in a buffer containing 25 mM HEPES

pH 7, 100 mM NaCl. This reaction was incubated on ice for 30 minutes and excess dye was removed with a NAP-5 column (GE, Marlborough, MA) pre-equilibrated with buffer containing 25 mM HEPES pH 7.5, 100 mM NaCl, 2 mM $MgCl_2$. Data for FRET equilibrium and time-course measurements were collected with a Gemini EM micro-plate reader (Molecular Devices, Sunnyvale, CA) with sensor excitation at 473 nm and fluorescence being recorded at 515 and 665 nm for donor and acceptor channels respectively. All experimental reactions consist of 1 μM protein and 500 μM nucleotide in a buffer containing 25 mM HEPES pH 7.5, 100 mM NaCl, and 2 mM $MgCl_2$. Raw FRET donor and acceptor signals were used to calculate a FRET efficiency where FRET efficiency = $I_{acceptor} / (I_{donor} + I_{acceptor})$.

*ATL mutant and isolated G domain crystallization and structure determination.*

ATL crystals were obtain with the catalytic core fragment for mutants (residues 1-446) and the isolated G domain (residues 1-339) through sitting drop vapor diffusion. Protein (10-30 mg/mL) was incubated with 2 mM nucleotide and 4 mM $MgCl_2$ for 1 hour at 25ºC, subsequently mixed with equal volume of reservoir solution, and stored at 20ºC. Initial crystal hits were optimized via hanging drop vapor diffusion at a protein concentration of 30 mg/mL. Final optimized condition are as follows: ATL1 $R^{77}A$, 0.2 M sodium malonate pH 6, 20% PEG-3350, 1 mM GDP, 2 mM $MgCl_2$; ATL1 $R^{77}A/F^{151}S$, 0.1 M Bis Tris pH 5.5, 0.2 M ammonium sulfate, 22% PEG3350, 1 mM GDP, 2 mM $MgCl_2$, 10% xylitol (cryoprotectant); ATL1 $F^{151}S$, 0.1 M ammonium citrate tribasic pH 7, 0.1 M imidazole pH 7, 20% PEG monomethyl ether 2,000, 1 mM GDP, 2 mM $MgCl_2$, 2 mM $AlCl_2$, 20 mM NaF; ATL1 G domain, 0.2M DL-malic acid pH 7, 20% PEG-3350, 1 mM

GDP, 2 mM $MgCl_2$. Single crystals appeared between 24-48 hours at 20ºC and if crystals were not grown in a cryoprotectant (see above), they were supplemented with 25% glycerol for 5 minutes and frozen in liquid nitrogen.

X-ray diffraction data were collected at the Cornell High Energy Synchrotron Source (CHESS), and data processing and scaling was carried out with X-ray Detector Software (XDS) and CCP4 software suite (Kabsch, 2010; Winn et al., 2011). Phases were attained through Molecular Replacement (MR) methods using the PHENIX software package and the coordinates of ATL1 (*3Q5E, GDP bound structures; 4IDO, GDP•$AlF_x$ bound structure*) as the search model (Adams et al., 2010). Refinements were carried out in PHENIX (Adams et al., 2010) and COOT (Emsley and Cowtan, 2004) to produce the final models. Data collection and model statistics are summarized in Table 3.1. Figure illustrations were made in Pymol (Version 1.8.4, Schrodinger, LLC). The aforementioned software packages were accessed through SBGrid (www.sbgrid. org; (Morin et al., 2013)).

## REFERENCES


Adams, P.D., Afonine, P.V., Bunkoczi, G., Chen, V.B., Davis, I.W., Echols, N., Headd, J.J., Hung, L.W., Kapral, G.J., Grosse-Kunstleve, R.W., McCoy, A.J., Moriarty, N.W., Oeffner, R., Read, R.J., Richardson, D.C., Richardson, J.S., Terwilliger, T.C., Zwart, P.H., 2010. PHENIX: a comprehensive Python-based system for macromolecular structure solution. Acta Cryst (2010). D66, 213-221 [doi:10.1107/S0907444909052925] 66, 1–9. doi:10.1107/S0907444909052925

Bian, X., Klemm, R.W., Liu, T.Y., Zhang, M., Sun, S., Sui, X., Liu, X., Rapoport, T.A., Hu, J., 2011. Structures of the atlastin GTPase provide insight into homotypic fusion of endoplasmic reticulum membranes. Proc. Natl. Acad. Sci. U.S.A. 108, 3976–3981. doi:10.1073/pnas.1101643108

Blackstone, C., O'Kane, C.J., Reid, E., 2011. Hereditary spastic paraplegias: membrane traffic and the motor pathway. Nat. Rev. Neurosci. 12, 31–42. doi:10.1038/nrn2946

Byrnes, L.J., Singh, A., Szeto, K., Benvin, N.M., O'Donnell, J.P., Zipfel, W.R., Sondermann, H., 2013. Structural basis for conformational switching and GTP loading of the large G protein atlastin. EMBO J. 32, 369–384. doi:10.1038/emboj.2012.353

Byrnes, L.J., Sondermann, H., 2011. Structural basis for the nucleotide-dependent dimerization of the large G protein atlastin-1/SPG3A. Proc. Natl. Acad. Sci. U.S.A. 108, 2216–2221. doi:10.1073/pnas.1012792108

Chappie, J.S., Acharya, S., Leonard, M., Schmid, S.L., Dyda, F., 2010. G domain dimerization controls dynamin's assembly-stimulated GTPase activity. Nature 465, 435–440. doi:10.1038/nature09032

Daumke, O., Praefcke, G.J.K., 2016. Invited review: Mechanisms of GTP hydrolysis and conformational transitions in the dynamin superfamily. Biopolymers 105, 580–593. doi:10.1002/bip.22855

De, N., Navarro, M.V.A.S., Wang, Q., Krasteva, P.V., Sondermann, H., 2010. Biophysical assays for protein interactions in the Wsp sensory system and biofilm formation. Meth. Enzymol. 471, 161–184. doi:10.1016/S0076-6879(10)71010-7

Emsley, P., Cowtan, K., 2004. Coot: model-building tools for molecular graphics. Acta Crystallogr. D Biol. Crystallogr. 60, 2126–2132. doi:10.1107/S0907444904019158

Ferguson, S.M., De Camilli, P., 2012. Dynamin, a membrane-remodelling GTPase. Nat Rev Mol Cell Biol 13, 75–88. doi:10.1038/nrm3266

Fink, J.K., 2013. Hereditary spastic paraplegia: clinico-pathologic features and emerging molecular mechanisms. Acta Neuropathol. doi:10.1007/s00401-013-1115-8

Fischer, D., Schabhuttl, M., Wieland, T., Windhager, R., Strom, T.M., Auer-Grumbach, M., 2014. A novel missense mutation confirms ATL3 as a gene for hereditary sensory neuropathy type 1. Brain 137, e286–e286. doi:10.1093/brain/awu091

Ghosh, A., Praefcke, G.J.K., Renault, L., Wittinghofer, A., Herrmann, C., 2006. How guanylate-binding proteins achieve assembly-stimulated processive cleavage of GTP to GMP. Nature 440, 101–104. doi:10.1038/nature04510

Guelly, C., Zhu, P.-P., Leonardis, L., Papić, L., Zidar, J., Schabhüttl, M., Strohmaier, H., Weis, J., Strom, T.M., Baets, J., Willems, J., De Jonghe, P., Reilly, M.M., Fröhlich, E., Hatz, M., Trajanoski, S., Pieber, T.R., Janecke, A.R., Blackstone, C., Auer-Grumbach, M., 2011. Targeted high-throughput sequencing identifies mutations in atlastin-1 as a cause of hereditary sensory neuropathy type I. Am. J. Hum. Genet. 88, 99–105. doi:10.1016/j.ajhg.2010.12.003

Haller, O., Gao, S., Malsburg, von der, A., Daumke, O., Kochs, G., 2010. Dynamin-like MxA GTPase: Structural Insights into Oligomerization and Implications for Antiviral Activity. Journal of Biological Chemistry 285, 28419–28424. doi:10.1074/jbc.R110.145839

Hu, J., Shibata, Y., Zhu, P.-P., Voss, C., Rismanchi, N., Prinz, W.A., Rapoport, T.A., Blackstone, C., 2009. A Class of Dynamin-like GTPases Involved in the Generation of the Tubular ER Network. Cell 138, 549–561. doi:10.1016/j.cell.2009.05.025

Hu, X., Wu, F., Sun, S., Yu, W., Hu, J., 2015. Human atlastin GTPases mediate differentiated fusion of endoplasmic reticulum membranes. Protein Cell 6, 307–311. doi:10.1007/s13238-015-0139-3

Hubner, C.A., Kurth, I., 2014. Membrane-shaping disorders: a common pathway in axon degeneration. Brain 137, 3109–3121. doi:10.1093/brain/awu287

Kabsch, W., 2010. XDS. Acta Cryst (2010). D66, 125-132 [doi:10.1107/S0907444909047337] 66, 1–8. doi:10.1107/S0907444909047337

Krissinel, E., Henrick, K., 2007. Inference of Macromolecular Assemblies from Crystalline State. Journal of Molecular Biology 372, 774–797. doi:10.1016/j.jmb.2007.05.022

Liu, T.Y., Bian, X., Romano, F.B., Shemesh, T., Rapoport, T.A., Hu, J., 2015. Cis and trans interactions between atlastin molecules during membrane fusion. Proc. Natl. Acad. Sci. U.S.A. 112, E1851–60. doi:10.1073/pnas.1504368112

Morin, A., Eisenbraun, B., Key, J., Sanschagrin, P.C., Timony, M.A., Ottaviano, M., Sliz, P., 2013. Collaboration gets the most out of software. eLife 2, e01456–6. doi:10.7554/eLife.01456

Morin-Leisk, J., Saini, S.G., Meng, X., Makhov, A.M., Zhang, P., Lee, T.H., 2011. An intramolecular salt bridge drives the soluble domain of GTP-bound atlastin into the postfusion conformation. The Journal of Cell Biology 195, 605–615. doi:10.1083/jcb.201105006

Nixon-Abell, J., Obara, C.J., Weigel, A.V., Li, D., Legant, W.R., Xu, C.S., Pasolli, H.A., Harvey, K., Hess, H.F., Betzig, E., Blackstone, C., Lippincott-Schwartz, J., 2016. Increased spatiotemporal resolution reveals highly dynamic dense tubular matrices in the peripheral ER. Science 354, aaf3928–aaf3928. doi:10.1126/science.aaf3928

O'Donnell, J.P., Cooley, R.B., Kelly, C.M., Miller, K., Andersen, O.S., Rusinova, R., Sondermann, H., 2017. Timing and Reset Mechanism of GTP Hydrolysis- Driven Conformational Changes of Atlastin. Structure 1–29. doi:10.1016/j.str.2017.05.007

Orso, G., Pendin, D., Liu, S., Tosetto, J., Moss, T.J., Faust, J.E., Micaroni, M., Egorova, A., Martinuzzi, A., McNew, J.A., Daga, A., 2009. Homotypic fusion of ER membranes requires the dynamin-like GTPase atlastin. Nature 460, 978–983. doi:10.1038/nature08280

Powers, R.E., Wang, S., Liu, T.Y., Rapoport, T.A., 2017. Reconstitution of the tubular endoplasmic reticulum network with purified components. Nature. doi:10.1038/nature21387

Praefcke, G.J.K., McMahon, H.T., 2004. The dynamin superfamily: universal membrane tubulation and fission molecules? Nat Rev Mol Cell Biol 5, 133–147. doi:10.1038/nrm1313

Rismanchi, N., Soderblom, C., Stadler, J., Zhu, P.P., Blackstone, C., 2008. Atlastin GTPases are required for Golgi apparatus and ER morphogenesis. Human Molecular Genetics 17, 1591–1604. doi:10.1093/hmg/ddn046

Saini, S.G., Liu, C., Lee, T.H., 2014. Membrane tethering by the atlastin GTPase depends on GTP hydrolysis but not on forming the cross-over configuration. Molecular Biology of the Cell 25, 3942–3953. doi:10.1091/mbc.E14-08-1284

Smith, B., Bevan, S., Vance, C., Renwick, P., Wilkinson, P., Proukakis, C., Squitieri, F., Berardelli, A., Warner, T., Reid, E., Shaw, C., 2009. Four novel SPG3A/atlastinmutations identified in autosomal dominant hereditary spastic paraplegia kindreds with intra-familial variability in age of onset and complex phenotype. Clin. Genet. 75, 485–489. doi:10.1111/j.1399-0004.2009.01184.x

Ulengin, I., Park, J.J., Lee, T.H., 2015. ER network formation and membrane fusion by atlastin1/SPG3A disease variants. Molecular Biology of the Cell 26, 1616–1628. doi:10.1091/mbc.E14-10-1447

Vetter, I.R., 2014. The Structure of the G Domain of the Ras Superfamily, in: Ras Superfamily Small G Proteins: Biology and Mechanisms 1. Springer, Vienna, pp. 25–50. doi:10.1007/978-3-7091-1806-1_2

Wang, S., Tukachinsky, H., Romano, F.B., Rapoport, T.A., 2016. Cooperation of the ER-shaping proteins atlastin, lunapark, and reticulons to generate a tubular membrane network. eLife 5, 209. doi:10.7554/eLife.18605

Winn, M.D., Ballard, C.C., Cowtan, K.D., Dodson, E.J., Emsley, P., Evans, P.R., Keegan, R.M., Krissinel, E.B., Leslie, A.G.W., McCoy, A., McNicholas, S.J., Murshudov, G.N., Pannu, N.S., Potterton, E.A., Powell, H.R., Read, R.J., Vagin, A.,

Wilson, K.S., 2011. Overview of the CCP4 suite and current developments. Acta Crystallogr. D Biol. Crystallogr. 67, 235–242. doi:10.1107/S0907444910045749

Winsor, J., Hackney, D.D., Lee, T.H., 2017. The crossover conformational shift of the GTPase atlastin provides the energy driving ER fusion. The Journal of Cell Biology jcb.201609071. doi:10.1083/jcb.201609071

Wu, F., Hu, X., Bian, X., Liu, X., Hu, J., 2015. Comparison of human and Drosophila atlastin GTPases. Protein Cell 6, 139–146. doi:10.1007/s13238-014-0118-0

Yan, L., Sun, S., Wang, W., Shi, J., Hu, X., Wang, S., Su, D., Rao, Z., Hu, J., Lou, Z., 2015. Structures of the yeast dynamin-like GTPase Sey1p provide insight into homotypic ER fusion. The Journal of Cell Biology 210, 961–972. doi:10.1083/jcb.201502078

Zhao, G., Zhu, P.-P., Renvoisé, B., Maldonado-Báez, L., Park, S.H., Blackstone, C., 2016. Mammalian knock out cells reveal prominent roles for atlastin GTPases in ER network morphology. Experimental Cell Research. doi:10.1016/j.yexcr.2016.09.015

Zhao, X., Alvarado, D., Rainier, S., Lemons, R., Hedera, P., Weber, C.H., Tukel, T., Apak, M., Heiman-Patterson, T., Ming, L., Bui, M., Fink, J.K., 2001. Mutations in a newly identified GTPase gene cause autosomal dominant hereditary spastic paraplegia. Nat. Genet. 29, 326–331. doi:10.1038/ng758

# CHAPTER 4

# CONCLUSIONS AND FUTURE DIRECTIONS

## SUMMARY OF FINDINGS

The works presented here describe a detailed framework for understanding the molecular actions of the GTPase ATL, which we have shown to use a distinct mechanism when compared to the canonical dynamin-related proteins. The elucidation of this conceptual framework was enabled through the marriage of three-dimensional structures, kinetic analyses, and biophysical measurements. This multifaceted approach established and cross-validated conformational states of ATL and the timing of events as ATLs progresses through a series of GTP hydrolysis dependent conformational changes *en route* to a successful membrane fusion event. Generalization of the mechanism between human ATLs was enabled from our comparative study of two isoforms (hATL1 and hATL3), which indicates that both enzymes follow the same reaction trajectory but do so at different rates. In short, GTP loading is facilitated by formation of a G/middle domain interaction, GTP binding and hydrolysis is accompanied by an intramolecular conformational change resulting in sequential oligomerization of the G and middle domains. The formation of this homodimer is required for the release of phosphate and an intramolecular arginine residue is responsible for resetting the reaction through the removal of a catalytic magnesium ion (**Figure 4.1A and Chapter 2**) (Byrnes et al., 2013; O'Donnell et al., 2017).

We utilized the aforementioned approaches to better understand how an atypical Hereditary Spastic Paraplegia disease mutation effects ATL function. This mutation,

**Figure 4.1. Summary of findings. (A)** Kinetic model and sequence of key steps in ATL's GTPase cycle. Pre-steady state measurements (with high temporal resolution) of GTP-loading, FRET-based conformational changes, dimerization, and phosphate release which were all recorded under the same experimental conditions to enable the direct comparison of kinetic steps. Nucleotide binding, intramolecular conformational changes, and GTP hydrolysis occur in succession, without lag-phases. G and M domain dimerization and phosphate release follow with increasingly long lag phases, indicating a clear sequence of events. hATL1 and hATL3 follows the same functional cycles, yet hATL3 isoform proceeds through several key steps slower than hATL1 **(Chapter 2)**. **(B)** Equilibrium between engaged and released middle domain is coupled allosterically through a series of hydrophobic residues. $F^{151}$ is the pivotal allostery transducer that relays information from the active-site to helix α-4 **(Chapter 3)**.

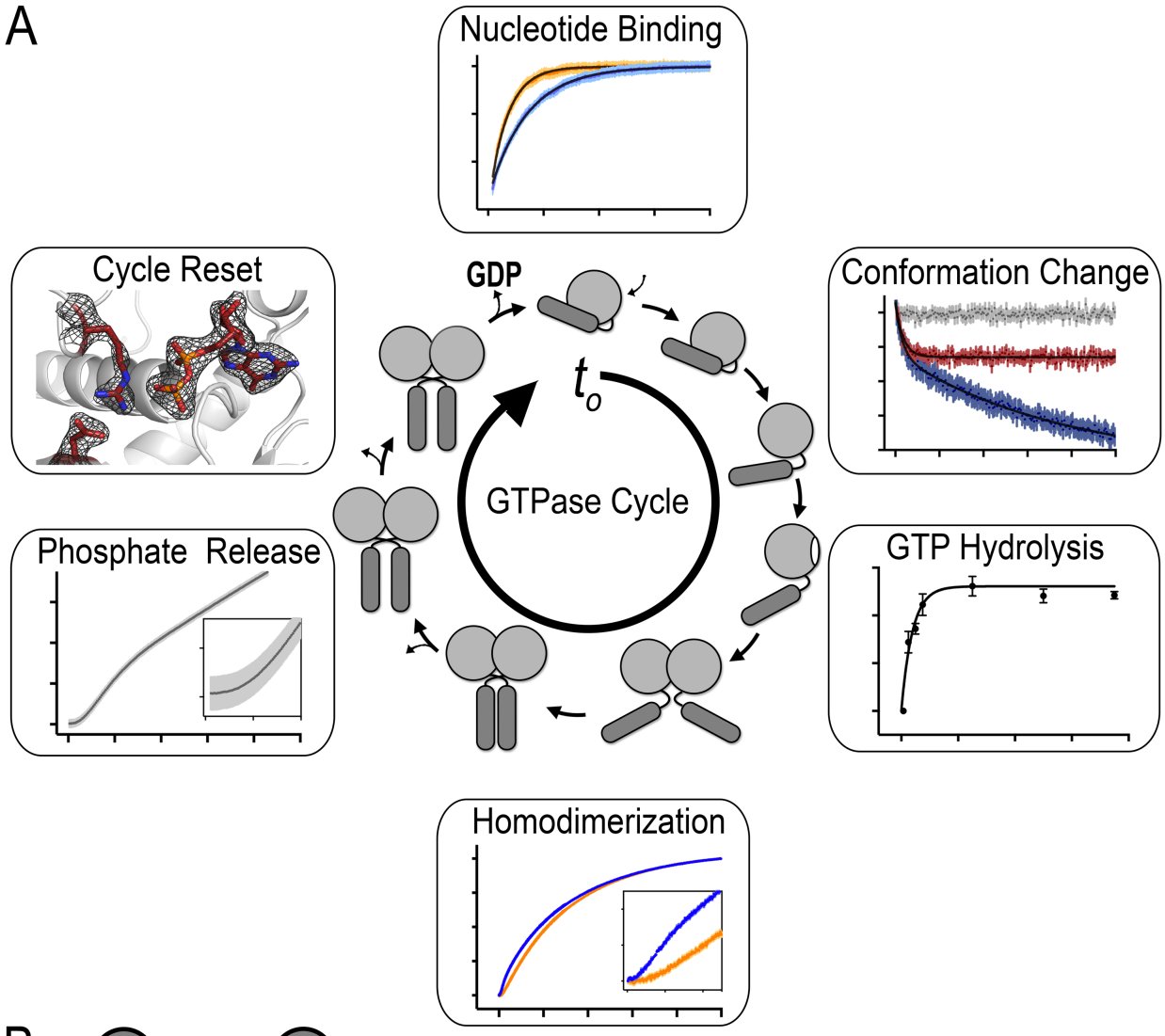
A
Nucleotide Binding
Conformation Change
GTP Hydrolysis
Homodimerization
Phosphate Release
Cycle Reset
GDP
$t_o$
GTPase Cycle

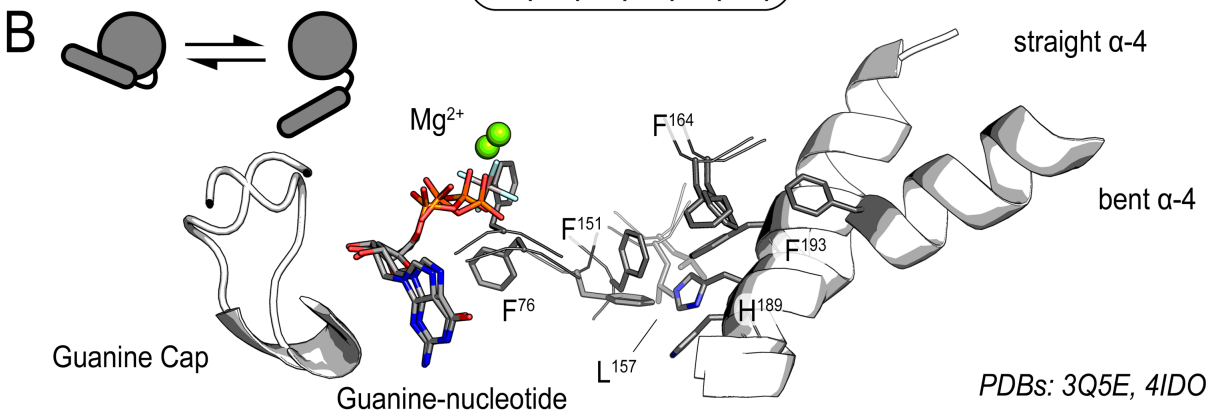
B
straight α-4
bent α-4
$Mg^{2+}$
$F^{164}$
$F^{151}$
$F^{193}$
$F^{76}$
$H^{189}$
$L^{157}$
Guanine Cap
Guanine-nucleotide
PDBs: 3Q5E, 4IDO

$F^{151}S$, is impaired in its ability to hydrolyze GTP but retains the capability to sample the high affinity homodimer that is characteristic of the transition state when bound to GDP•$AlF_x$. The conformational switching defect within the catalytic core of ATL in combination with structural insight from various crystal structures provided a novel allosteric coupling mechanism. This coupling occurs through a series of hydrophobic residues that connects the active-site to an inter-domain interface responsible for nucleotide loading (**Figure 4.1A and Chapter 3**).

## FUTURE DIRECTIONS

*Fusion between proper membranes requires a vectorial reaction.*

Membrane fusion can be defined as a the process where two non-identical membranes merge. Not surprisingly, this highly energy-dependent reaction requires enzymatic machineries for completion. The majority of the established fusion machineries have developed mechanisms to accomplish this reaction vectorially, which guarantees that fusion occurs between the proper membranes (commonly opposing membranes *in trans).* This requirement eliminates futile fusion cycles from occurring between unwanted *cis*-membranes. Directionality is established for SNARE-mediated fusion via distinct proteins localized on the target and vesicle membrane surfaces, and viral fusion requires receptor mediated interactions to enrich for interactions with the host membrane (Martens and McMahon, 2008). Since SNARE- and viral-mediated fusion both involve heterotypic interactions, a very straightforward mechanism exists for assuring that *trans*-fusion occurs (McNew et al., 2013). However, ATLs rely on homotypic oligomerization making it difficult to deduce analogous mechanisms from heterotypic-based fusion machineries. Consequently, the underlying mechanism of how ATLs initiate vectorial fusion remains to be determined. We hypothesize that N-terminal motifs that precede the GTPase domain of human ATLs contribute to higher-order oligomerization and enable a bias towards *trans*-interactions that enrich for vectorial fusion events.

*ATL's N-terminus may mediate higher-order oligomerization.*

The N-terminal motif hypothesis stems from a novel crystal structure of the hATL1 catalytic core fragment which is globally similar to previous structures where the G and middle domains are engaged to form the nucleotide-loading competent state (Byrnes and Sondermann, 2011; O'Donnell et al., 2017). The hallmark of this structure originates from the first thirty amino acids where for the first time, residues are resolved and form a structured β-hairpin motif. This β-hairpin protrudes from one ATL monomer and interacts with the ATL molecule in the adjoining unit cell. This interaction repeats through the crystal lattice forming a linear array of ATL molecules. If one were to hypothetically superimpose this array onto a membrane, the nucleotide binding sites and G domain dimerization interfaces uniformly face away from plane. An appealing model is that ATLs minimize the propensity for cis-fusion through linear arrays that inhibit fusion-based dimerization from occurring within the same membrane. Thus, homodimerization would be biased to occur with an opposing array of ATLs on a trans-membrane, akin to a 'zipper-like' mechanism (**Figure 4.2A**). Curiously, a novel crystal structure of the hATL3 isoform contains a helical N-terminal motif that is distinct in comparison to hATL1's β-hairpin motif (**Figure 4.2B**). If our model is correct, ATL isoforms having distinct N-terminal motifs could serve as a structural recognition sequence to prevent and/or promote oligomerization between the different atlastin isoforms or these motifs could mediate clustering of ATLs to promote avidity effects for *trans*-interactions with opposing membranes.

One caveat to our proposed model is that oligomerization beyond a dimer for ATLs has never been seen in solution (Bian et al., 2011; Byrnes et al., 2013; Byrnes and

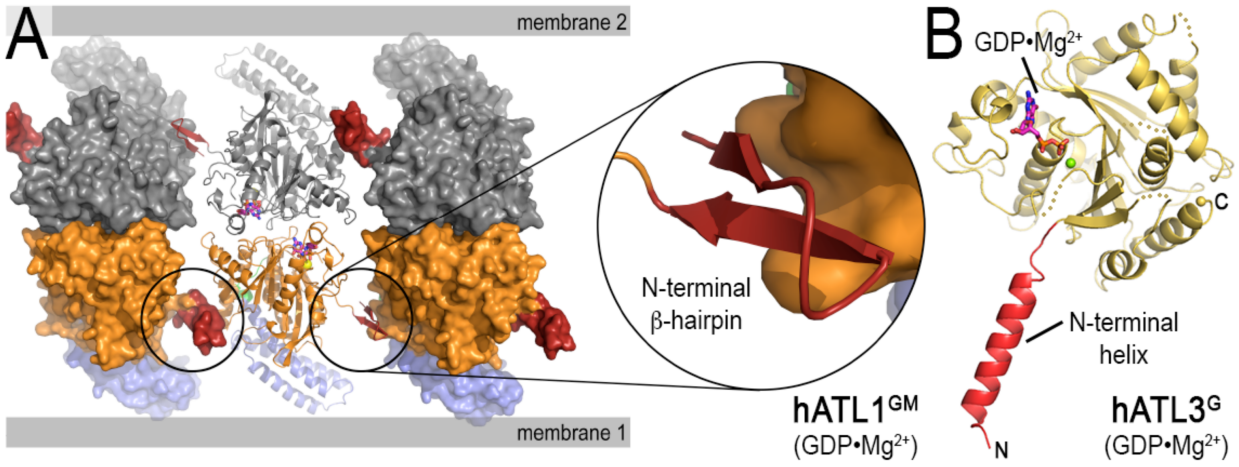


**Figure 4.2. First structural views of hATL's N-terminal motifs and probing its role their on ATL oligomerization. (A)** New 2Å-crystal structure of the catalytic core fragment. In the crystal, hATL1 protomers line up to form a zipper-like structure with an ordered, N-terminal motif (red) mediating lattice contacts (circle). One half of the 'zipper' is colored in gray, the other half in orange (G domain) and blue (M domain). The N-terminal motif also contains serine phosphorylation sites. (B) New 3Å-crystal structure of hATL3's G domain. The N-terminal motif and G domain were colored in red and yellow, respectively.

Sondermann, 2011; Morin-Leisk et al., 2011; O'Donnell et al., 2017). However, it is well established that transitioning from solution-based diffusion in three-dimensions to planar-based two-dimensional diffusion can have profound effects on enzyme kinetics and molecular interactions (Gureasko et al., 2008; Kholodenko et al., 2000). Restricting ATL diffusion to a two-dimensional plane, analogous to its native membrane environment, could bolster the weak interactions that we observe in the crystals, rendering them physiologically relevant.

*In vitro experiments with potential to elucidate higher-order oligomerization.*

To test this hypothesis, we designed experiments to assess if ATL's N-terminus contributes to quaternary structure formation on membrane surfaces using supported

lipid bilayers and liposomes. For this purpose, we will use the soluble ATL core fragment from the three human isoforms, with and without the N-terminal motifs. The catalytic core of ATL has proven to be a valuable proxy for understanding the full-length protein as it has a comparable GTPase activity, inhibits ATL-mediated fusion in a GTPase-dependent manner, and can tether membranes when anchored to liposomes (see below) (Liu et al., 2012).

We plan to conduct single-molecule imaging of ATLs on supported lipid bilayers using total internal reflection fluorescence (TIRF) microscopy following established protocols (Groves et al., 2008; Lillemeier et al., 2010; Nye and Groves, 2008). For detection, proteins will be labeled using the same strategies used for FRET studies in Chapters 2 and 3. We will tether ATL molecules to supported lipid bilayers through the protein's C-terminal $His_6$-tag and NiNTA containing lipids (NiDOGS) in a topology that mimics the native full-length protein (**Figure 4.3A**). Determination of the oligomeric state of ATL will be carried out by quantifying photobleaching steps, differences in diffusion coefficients, and two color co-localization. The first assay relies on tracking proteins and their intensities over time; as spontaneous photobleaching occurs, the bleach steps can be counted and correspond to the number of ATLs co-diffusing. If multiple bleach steps exist for a given diffusing particle, we can conclude that ATLs are forming higher-order oligomers and the removal of the N-terminus should eliminate the multiple bleach steps measured. The next approach would be determining diffusion coefficients of single particles with and without the N-terminal motifs. Since larger molecules diffuse more slowly, differences measured between the samples with and without the N-terminal motif should illuminate differences in the size of the oligomers. The last approach relies on

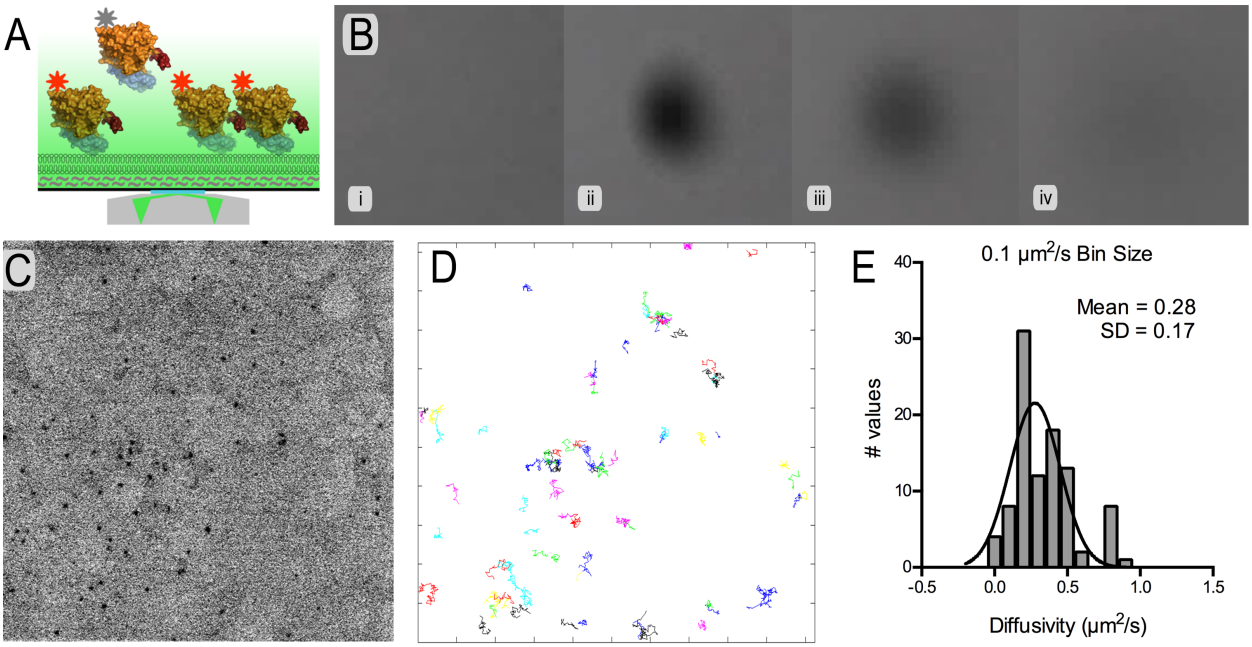


**Figure 4.3. Investigating ATL higher-order oligomerization on supported lipid bilayers (SLBs). (A)** TIRF microscopy only illuminates molecules in the evanescent field (close to the membrane). Multi-color, single-molecule tracking/colocalization and photobleaching experiments will report on the oligomeric state of the proteins. **(B)** Frames from a Fluorescence recovery after photobleaching video (i-iv) indicating that SLBs (containing rhodamine-PE as a fluorescent marker) are fluid and void of defects. **(C)** Successful anchoring of ATL-$His_6$ to SLBs via NiDOGS at concentrations amenable to single molecule tracking. **(D)** Single particle tracking trajectories establish that ATL-lipid conjugates are highly moble. **(E)** Quantification of diffusivity from panel D reveals a diffusion constant of 0.28 ± 0.17 $\mu M^2/s$ for ATL3.

co-localization of protein mixtures that have been labeled with different colored fluorophores. Separately labeling the same isoform with two colors provides a method for validating higher-order oligomerization, and co-localization of separately labeled isoforms will indicate if the higher-order oligomers are homotypic or heterotypic in ATL composition.

Preliminary data suggest that we are able to produce high-quality fluid supported bilayers devoid of gaps or holes in the bilayer; fluidity was measured via fluorescence recovery after photobleaching (FRAP) yielding a diffusivity constant of ~1 $\mu m^2$/sec which

is similar to published values (**Figure 4.3B**) (Rose et al., 2015). We were also successful in anchoring hATL3-$His_6$ to supported bilayers containing NiDOGS lipids at protein concentrations that are amenable for single molecule tracking (**Figure 4.3C**). Single-molecule tracking trajectories indicate that the anchored ATL molecules were highly mobile (**Figure 4.3D**). From the single molecule tracking trajectories, diffusivity constants for hATL3 was determined to be 0.28 ± 0.17 $\mu m^2$/sec which is 5-fold slower than analogous measurements made using a similar system with dmATL (**Figure 4.3E**) (Liu et al., 2015). We are currently working with on extracting particle intensities from single particle tracking data in order to determine the number of photo-bleaching steps that occur for each ATL particle as well as conducting the aforementioned experiments with all human ATL isoforms with and without their N-terminal motifs.

A secondary *in vitro* method for probing how ATL's N-terminus may impact higher-order oligomerization is vesicle tethering. Using a similar approach for anchoring ATLs via NiDOGS, we are able to detect increased solution turbidity when ATL containing proteoliposomes are tethered in a GTPase-dependent manner (**Figure 4.4A**). Our primary data indicate that hATL1's $His_6$-tagged catalytic core fragment targeted to NiDOGS-containing vesicles supports tethering in the presence of GTP, and more importantly, a variant lacking the N-terminal β-hairpin motif exhibits slower tethering kinetics (**Figure 4.4B**). This change in tethering kinetics is not due to differences in enzymatic activity as both wild-type and the N-terminal truncation have comparable GTP-hydrolysis rates while anchored to liposomes with $k_{cat}$ values of 2.6 and 2.8 $sec^{-1}$ respectively. In the future, we will use this assay to probe tethering kinetics for wild-type and N-terminal truncations of hATL2 and hATL3. These promising

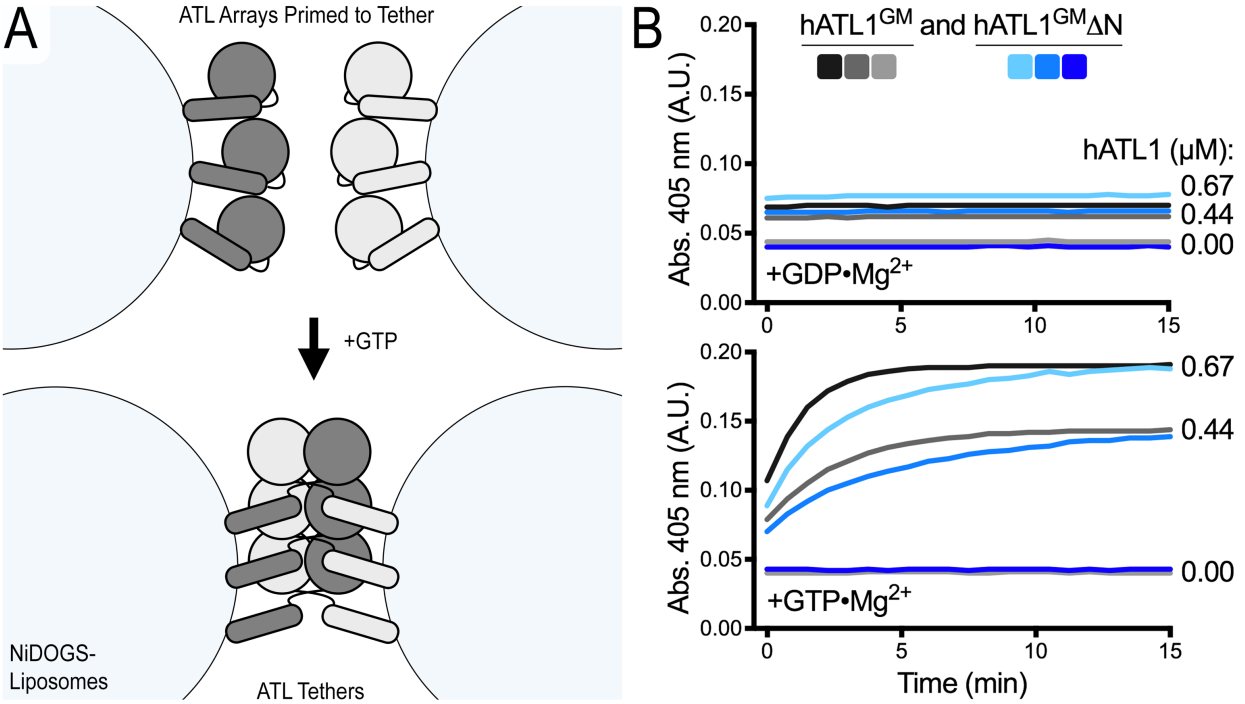


**Figure 4.4. The absence of ATL1 N-terminal β-hairpin decreases rate of GTP-dependent ATL tethering. (A)** Schematic model for how ATLs could tether liposomes *in trans*. **(B)** Tethering of vesicles (100 nm; DOPC/2% NiDOGS) was determined by measuring turbidity at 405 nm. His6-tagged, human ATL1 catalytic core fragments (GM) with or without N-terminal β-hairpin were pre-bound to vesicle and followed by addition of GDP (top) or GTP (bottom). Representative data of multiple biological replicates are shown. Note: GTPase activities were comparable for both proteins when anchored to liposomes ($k_{cat}$ of 2.63±0.01 and 2.84±0.01 $sec^{-1}$ for hATLGM and hATLGMΔN, respectively).

experiments have the potential to reveal the importance of the N-terminal motifs on ATL function, which together with the previously mentioned imaging studies may help elucidate mechanisms of higher-order oligomerization and/or avidity effects that assist in initiating vectorial fusion in ATLs.

*Validation of in vitro observations and the impact the N-terminal motif has on ER morphology.*

We adopted well-established cell culture systems (COS7 and HeLa) for validation of our *in vitro* studies regarding ATL's function in maintaining organelle morphology. (Morin-Leisk et al., 2011; Moss et al., 2011; Nixon-Abell et al., 2016) Organelle morphology has been shown to be compromised when dominant-negative alleles are exogenously expressed or when ATLs are pan-depleted using either siRNA knock-down or CRISPER/Cas9 mediated gene deletion (Rismanchi et al., 2008; G. Zhao et al., 2016). The characteristic exchange of three-way junctions for long unbranched tubules is a phenotype that the field has previously used extensively to score the severity of ATL mutants. Here we plan to investigate the role of ATL's structured N-terminal motif on ER morphology. Because ATL mutations (including those of HSP origin) are often dominant-negative, we first expressed constructs with and without the N-terminus in COS7 cells containing ATL to see if ER morphology was disrupted. Our preliminary data indicate that wild-type ATL1 localizes specifically to the ER as previously determined (Nixon-Abell et al., 2016; Rismanchi et al., 2008). The tubular ER network displaying the characteristic lace-like morphology is clearly visible in both cells exogenously expressing ATL and non-transfected cells stained with antibodies detecting ER-resident

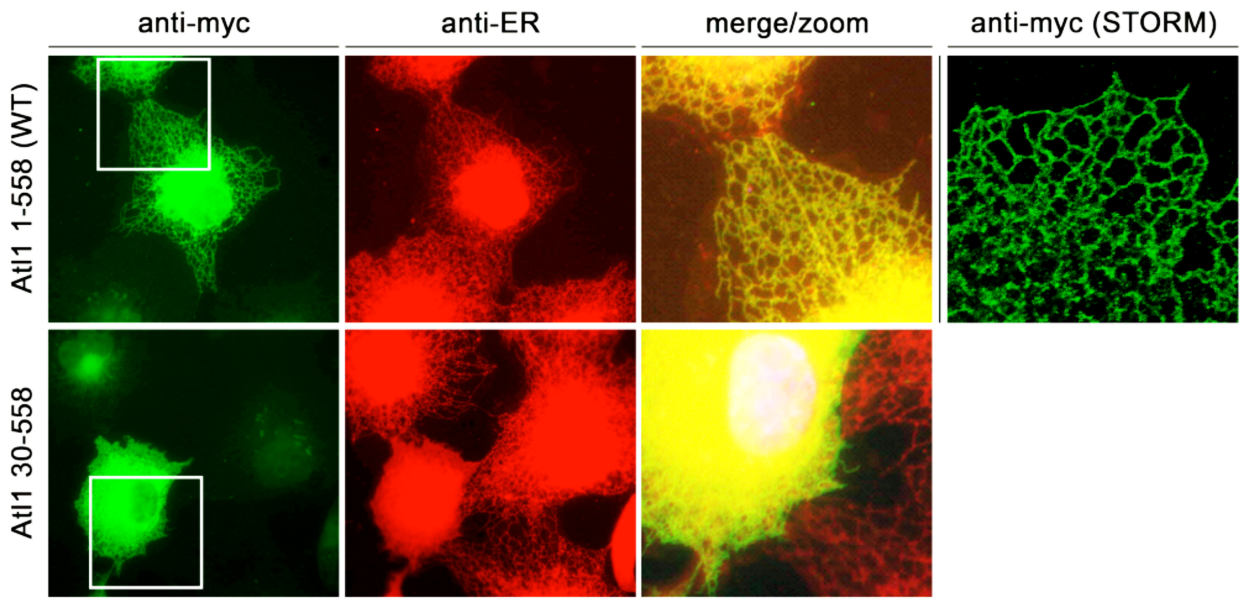


**Figure 4.5. ATL1 N-terminal deletion in cells.** Immuno-fluorescence staining of COS7 cells transfected with myc-tagged ATL variants (anti-ER: calnexin). Images were taken on a Zeiss AxioObserver inverted microscope (except for the TIRF-STORM image). Brightness/contrast were adjusted for better visualization.

proteins (ie: calnexin) (**Figure 4.5**). Unlike other dominant-negative mutants that produce fewer ER junctions, the N-terminal truncation produces an abnormal morphology that appears condensed and hyper-fused (**Figure 4.5**). We conducted a preliminary quantification of the reticular ER, determining it accounts for 79% of non-transfected cells, 64% for ATL1 expression, and 36% for hATL1 N-terminal truncation. More extensive characterization is underway, however, the observed ER appearance is a rather uninformative phenotype. From basic microscopy, it is challenging to determine if the aberrant ER architecture is due to hyper/hypo-fusion or a different perturbation. An alternative microscopy method to utilize is super-resolution microscopy (stochastic optical reconstruction microscopy, STORM) to obtain images that can be quantified more rigorously (Toomre and Bewersdorf, 2010). Preliminary results reveal well-

resolved, tubular ER structures, confirming the feasibility of the experiments. (**Figure 4.5**). Another approach to attaining a clearer phenotype would be to conduct imaging on cells devoid of atlastin. Recently, CRISPER/Cas9 was used to mediate a triple-deletion of ATLs in NIH3T3 cells (G. Zhao et al., 2016). ER morphology is disrupted in these cell lines and the exogenous expression of hATL1 rescues this phenotype (G. Zhao et al., 2016). We recently acquired these cell lines and are looking forward to testing how various ATL isoforms with and without N-terminal motifs rescue the proper architecture of the ER.

*Transcending ATL-centric mechanisms.*

We are encouraged by the preliminary support for our model regarding direction initiating mechanisms of ATL mediated fusion as discussed above and illustrated in Figure 4.2. All of the mechanisms that we have uncovered to date comprise forms of intrinsic ATL regulation and include conformational changes, ordering of oligomeric events, cycle resetting, allosteric coupling, and the potential for higher-order oligomerization. In the future, it will be important to explore external systems that regulate ATLs. As ATLs do not operate in isolation, the questions surrounding the importance of post-translational modifications and how ATLs communicate with other proteins remain vitally important for refining the global mechanisms for atlastin mediated membrane fusion.

*Post-translational Modifications:* Many DRPs are regulated by post-translational modifications (Anton et al., 2013; Graham et al., 2007; Leboucher et al., 2012), a fairly unexplored area for ATLs. Several shotgun proteomics screens have revealed post-

translational modifications of serine residues resident to ATL's N-terminal β-hairpin (p-S10/15/22/23) *in vivo* (Villén et al., 2007), yet the functional relevance of these modifications has not been established. To evaluate the effect of phosphorylation, both biophysical and cellular based platforms will be used. We will create Ser-to-Ala and Ser-to-Glu mutations, which would be predicted to prevent or mimic phosphorylation, respectively. In context to ER morphology, post-translational modifications could either have a negative effect on ATL function, causing a dominant-negative phenotype similar to other loss of function mutations, or a positive effect similar to that of the N-terminal truncation mutant. The same mutations can be recombinantly expressed and used for *in vitro* measurements on supported bilayers and liposomes. Unique post-translational modifications of ATL isoforms could confer additional regulation of ATL isoform clusters (e.g. as a "mixing"/"de-mixing" switch). These experiments are interesting in light of isoform-specific phenomena, which may require distinct populations (X. Hu et al., 2015; O'Donnell et al., 2017; Polisetty et al., 2012; Yan et al., 2015).

*ATLs operational landscape:* It is well established the dynamin related proteins require additional external factors to modulate function. The prototypical fission protein dynamin relies on Bar domain-containing and signaling proteins to provide spacial and temporal control of GTPase activity and the fission reaction (Daumke et al., 2014; Quan and Robinson, 2013). Mitochondrial fusion machinery, OPA1, relies on both homotypic interactions to stabilize the cristae via OPA1 tethers and heterotypic interactions between the OPA1 and cardiolipin for efficient inner mitochondrial fusion (Ban et al., 2017). An ATL-like protein, neurolastin, is known to interact with the nuclear transcription factor Plzf and with a ubiquitin-conjugating enzyme (Inoue et al., 1997;

Lomash et al., 2015). ATLs interact with the membrane-shaping reticulon and REEP proteins, protrudin, and the microtubule-severing protein spastin (Blackstone, 2012; Chang et al., 2013; Hashimoto et al., 2014; J. Hu et al., 2009). The known interactions concerning ATLs have been associated with the same neurological disorder, HSP, indicating their strong functional relationship. However, the identity of more subtle ATL interactions is incomplete leaving a limited understanding of mechanisms that regulate ATL's cellular function.

With minimal knowledge of ATLs molecular interactions and operational environment, an unbiased proteomic screen to identify novel protein interactions is essential. Unfortunately, proteomic identification of membrane protein interactions remains a challenging task due to disruption of cellular organelles via harsh detergents prior to affinity purification. To overcome this obstacle, we propose the use of a novel proximity-dependent biotinylation method. This method allows for labeling of the operational landscape surrounding your protein of interest while in its native environment within live cells. Once labeled, candidates are purified and subsequently identified with mass spectrometry. Specifically, the technique BioID relies on a mutant biotin ligase (BirA-$R^{118}G$ from *E. coli* denoted BirA*) that nonspecifically releases activated biotin for spontaneous modification of proximal lysine residues in the vicinity of ~100 Å (Roux et al., 2013; 2012). Expression of BirA*-ATL fusion proteins allows both direct and peripheral interactions to labeled and subsequently identified. The identified candidates could be subsequently verified *in vitro* using co-immunoprecipitation, SEC-MALS, or ITC and *in vivo* using co-localization and fluorescence lifetime imaging microscopies. With regard to cellular function, ATLs have been implicated in BMP

signaling, store-operated calcium entry, lipid droplet size, membrane protein partitioning to the inner nuclear membrane, and *Legionella pneumophila* related host/pathogen interactions (Fassier et al., 2010; Klemm et al., 2013; Li et al., 2017; Pawar et al., 2017; J. Zhao and Hedera, 2012; Steiner et al., 2017); however detailed mechanisms are yet to be determined. It will be interesting to uncover the identity of ATLs operational landscape to shed light on the aforementioned and novel processes.

The work established here provides blueprints and mechanisms that describe the inner-workings of the ATL mediated membrane fusion. It will be compelling to look back on these studies in the future to see how our foundational knowledge has assisted in establishing novel insight into membrane fusion, cell biology and in the long term, translational sciences.

## REFERENCES


Anton, F., Dittmar, G., Langer, T., Escobar-Henriques, M., 2013. Two deubiquitylases act on mitofusin and regulate mitochondrial fusion along independent pathways. Molecular Cell 49, 487–498. doi:10.1016/j.molcel.2012.12.003

Ban, T., Ishihara, T., Kohno, H., Saita, S., Ichimura, A., Maenaka, K., Oka, T., Mihara, K., Ishihara, N., 2017. Molecular basis of selective mitochondrial fusion by heterotypic action between OPA1 and cardiolipin. Nat. Cell Biol. 505, 335–14. doi:10.1038/ncb3560

Bian, X., Klemm, R.W., Liu, T.Y., Zhang, M., Sun, S., Sui, X., Liu, X., Rapoport, T.A., Hu, J., 2011. Structures of the atlastin GTPase provide insight into homotypic fusion of endoplasmic reticulum membranes. Proc. Natl. Acad. Sci. U.S.A. 108, 3976–3981. doi:10.1073/pnas.1101643108

Blackstone, C., 2012. Cellular pathways of hereditary spastic paraplegia. Annu. Rev. Neurosci. 35, 25–47. doi:10.1146/annurev-neuro-062111-150400

Byrnes, L.J., Singh, A., Szeto, K., Benvin, N.M., O'Donnell, J.P., Zipfel, W.R., Sondermann, H., 2013. Structural basis for conformational switching and GTP loading of the large G protein atlastin. EMBO J. 32, 369–384. doi:10.1038/emboj.2012.353

Byrnes, L.J., Sondermann, H., 2011. Structural basis for the nucleotide-dependent dimerization of the large G protein atlastin-1/SPG3A. Proc. Natl. Acad. Sci. U.S.A. 108, 2216–2221. doi:10.1073/pnas.1012792108

Chang, J., Lee, S., Blackstone, C., 2013. Protrudin binds atlastins and endoplasmic reticulum-shaping proteins and regulates network formation. Proc. Natl. Acad. Sci. U.S.A. 110, 14954–14959. doi:10.1073/pnas.1307391110

Daumke, O., Roux, A., Haucke, V., 2014. BAR domain scaffolds in dynamin-mediated membrane fission. Cell 156, 882–892. doi:10.1016/j.cell.2014.02.017

Fassier, C., Hutt, J.A., Scholpp, S., Lumsden, A., Giros, B., Nothias, F., Schneider-Maunoury, S., Houart, C., Hazan, J., 2010. Zebrafish atlastin controls motility and

spinal motor axon architecture via inhibition of the BMP pathway. Nat Neurosci 13, 1380–1387. doi:10.1038/nn.2662

Graham, M.E., Anggono, V., Bache, N., Larsen, M.R., Craft, G.E., Robinson, P.J., 2007. The in Vivo Phosphorylation Sites of Rat Brain Dynamin I. J. Biol. Chem. 282, 14695–14707. doi:10.1074/jbc.M609713200

Groves, J.T., Parthasarathy, R., Forstner, M.B., 2008. Fluorescence imaging of membrane dynamics. Annu Rev Biomed Eng 10, 311–338. doi:10.1146/annurev.bioeng.10.061807.160431

Gureasko, J., Galush, W.J., Boykevisch, S., Sondermann, H., Bar-Sagi, D., Groves, J.T., Kuriyan, J., 2008. Membrane-dependent signal integration by the Ras activator Son of sevenless. Nat Struct Mol Biol 15, 452–461. doi:10.1038/nsmb.1418

Hashimoto, Y., Shirane, M., Matsuzaki, F., Saita, S., Ohnishi, T., Nakayama, K.I., 2014. Protrudin Regulates Endoplasmic Reticulum Morphology and Function Associated with the Pathogenesis of Hereditary Spastic Paraplegia. Journal of Biological Chemistry. doi:10.1074/jbc.M113.528687

Hu, J., Shibata, Y., Zhu, P.-P., Voss, C., Rismanchi, N., Prinz, W.A., Rapoport, T.A., Blackstone, C., 2009. A Class of Dynamin-like GTPases Involved in the Generation of the Tubular ER Network. Cell 138, 549–561. doi:10.1016/j.cell.2009.05.025

Hu, X., Wu, F., Sun, S., Yu, W., Hu, J., 2015. Human atlastin GTPases mediate differentiated fusion of endoplasmic reticulum membranes. Protein Cell 6, 307–311. doi:10.1007/s13238-015-0139-3

Inoue, S., Orimo, A., Saito, T., Ikeda, K., Sakata, K., Hosoi, T., Orimo, H., Ouchi, Y., Muramatsu, M., 1997. A novel RING finger protein, BFP, predominantly expressed in the brain. Biochemical and Biophysical Research Communications 240, 8–14. doi:10.1006/bbrc.1997.7589

Kholodenko, B.N., Hoek, J.B., Westerhoff, H.V., 2000. Why cytoplasmic signalling proteins should be recruited to cell membranes. Trends in Cell Biology 10, 173–178.

Klemm, R.W., Norton, J.P., Cole, R.A., Li, C.S., Park, S.H., Crane, M.M., Li, L., Jin, D., Boye-Doe, A., Liu, T.Y., Shibata, Y., Lu, H., Rapoport, T.A., Farese, R.V., Blackstone,

C., Guo, Y., Mak, H.Y., 2013. A Conserved Role for Atlastin GTPases in Regulating Lipid Droplet Size. Cell Rep 3, 1465–1475. doi:10.1016/j.celrep.2013.04.015

Leboucher, G.P., Tsai, Y.C., Yang, M., Shaw, K.C., Zhou, M., Veenstra, T.D., Glickman, M.H., Weissman, A.M., 2012. Stress-Induced Phosphorylation and Proteasomal Degradation of Mitofusin 2 Facilitates Mitochondrial Fragmentation and Apoptosis. Molecular Cell 47, 547–557. doi:10.1016/j.molcel.2012.05.041

Li, J., Yan, B., Si, H., Peng, X., Zhang, S.L., Hu, J., 2017. Atlastin regulates store-operated calcium entry for nerve growth factor-induced neurite outgrowth. Sci Rep 7, 43490. doi:10.1038/srep43490

Lillemeier, B.F., Mörtelmaier, M.A., Forstner, M.B., Huppa, J.B., Groves, J.T., Davis, M.M., 2010. TCR and Lat are expressed on separate protein islands on T cell membranes and concatenate during activation. Nat. Immunol. 11, 90–96. doi: 10.1038/ni.1832

Liu, T.Y., Bian, X., Romano, F.B., Shemesh, T., Rapoport, T.A., Hu, J., 2015. Cis and trans interactions between atlastin molecules during membrane fusion. Proc. Natl. Acad. Sci. U.S.A. 112, E1851–60. doi:10.1073/pnas.1504368112

Liu, T.Y., Bian, X., Sun, S., Hu, X., Klemm, R.W., Prinz, W.A., Rapoport, T.A., Hu, J., 2012. Lipid interaction of the C terminus and association of the transmembrane segments facilitate atlastin-mediated homotypic endoplasmic reticulum fusion. Proc. Natl. Acad. Sci. U.S.A. 109, E2146–54. doi:10.1073/pnas.1208385109

Lomash, R.M., Gu, X., Youle, R.J., Lu, W., Roche, K.W., 2015. Neurolastin, a Dynamin Family GTPase, Regulates Excitatory Synapses and Spine Density. Cell Rep 12, 743–751. doi:10.1016/j.celrep.2015.06.064

Martens, S., McMahon, H.T., 2008. Mechanisms of membrane fusion: disparate players and common principles. Nat Rev Mol Cell Biol 9, 543–556. doi:10.1038/nrm2417

McNew, J.A., Sondermann, H., Lee, T., Stern, M., Brandizzi, F., 2013. GTP-Dependent Membrane Fusion. Annu. Rev. Cell Dev. Biol. 29, 529–550. doi:10.1146/annurev-cellbio-101512-122328

Morin-Leisk, J., Saini, S.G., Meng, X., Makhov, A.M., Zhang, P., Lee, T.H., 2011. An intramolecular salt bridge drives the soluble domain of GTP-bound atlastin into the postfusion conformation. The Journal of Cell Biology 195, 605–615. doi:10.1083/jcb.201105006

Moss, T.J., Andreazza, C., Verma, A., Daga, A., McNew, J.A., 2011. Membrane fusion by the GTPase atlastin requires a conserved C-terminal cytoplasmic tail and dimerization through the middle domain. Proc. Natl. Acad. Sci. U.S.A. 108, 11133–11138. doi:10.1073/pnas.1105056108

Nixon-Abell, J., Obara, C.J., Weigel, A.V., Li, D., Legant, W.R., Xu, C.S., Pasolli, H.A., Harvey, K., Hess, H.F., Betzig, E., Blackstone, C., Lippincott-Schwartz, J., 2016. Increased spatiotemporal resolution reveals highly dynamic dense tubular matrices in the peripheral ER. Science 354, aaf3928–aaf3928. doi:10.1126/science.aaf3928

Nye, J.A., Groves, J.T., 2008. Kinetic control of histidine-tagged protein surface density on supported lipid bilayers. Langmuir 24, 4145–4149. doi:10.1021/la703788h

O'Donnell, J.P., Cooley, R.B., Kelly, C.M., Miller, K., Andersen, O.S., Rusinova, R., Sondermann, H., 2017. Timing and Reset Mechanism of GTP Hydrolysis- Driven Conformational Changes of Atlastin. Structure 1–29. doi:10.1016/j.str.2017.05.007

Pawar, S., Ungricht, R., Tiefenboeck, P., Leroux, J.-C., Kutay, U., 2017. Efficient protein targeting to the inner nuclear membrane requires atlastin-dependent maintenance of ER topology. eLife 6. doi:eLife 2017;6:e28202 / 10.7554/eLife.28202

Polisetty, R.V., Gautam, P., Sharma, R., Harsha, H.C., Nair, S.C., Gupta, M.K., Uppin, M.S., Challa, S., Puligopu, A.K., Ankathi, P., Purohit, A.K., Chandak, G.R., Pandey, A., Sirdeshmukh, R., 2012. LC-MS/MS Analysis of Differentially Expressed Glioblastoma Membrane Proteome Reveals Altered Calcium Signaling and Other Protein Groups of Regulatory Functions 11, M111.013565–M111.013565. doi:10.1074/mcp.M111.013565

Quan, A., Robinson, P.J., 2013. Syndapin--a membrane remodelling and endocytic F-BAR protein. FEBS J. 280, 5198–5212. doi:10.1111/febs.12343

Rismanchi, N., Soderblom, C., Stadler, J., Zhu, P.P., Blackstone, C., 2008. Atlastin GTPases are required for Golgi apparatus and ER morphogenesis. Human Molecular Genetics 17, 1591–1604. doi:10.1093/hmg/ddn046

Rose, M., Hirmiz, N., Moran-Mirabal, J., Fradin, C., 2015. Lipid Diffusion in Supported Lipid Bilayers: A Comparison between Line-Scanning Fluorescence Correlation Spectroscopy and Single-Particle Tracking. Membranes 5, 702–721. doi:10.3390/membranes5040702

Roux, K.J., Kim, D.I., Burke, B., 2013. BioID: A Screen for Protein-Protein Interactions, Current protocols in protein science. John Wiley & Sons, Inc. doi:10.1002/0471140864.ps1923s74

Roux, K.J., Kim, D.I., Raida, M., Burke, B., 2012. A promiscuous biotin ligase fusion protein identifies proximal and interacting proteins in mammalian cells. The Journal of Cell Biology 196, 801–810. doi:10.1083/jcb.201112098

Steiner, B., Swart, A.L., Welin, A., Weber, S., Personnic, N., Kaech, A., Freyre, C., Ziegler, U., Klemm, R.W., Hilbi, H., 2017. ER remodeling by the large GTPase atlastin promotes vacuolar growth of Legionella pneumophila. EMBO Rep. 1–20. doi:10.15252/embr.201743903

Toomre, D., Bewersdorf, J., 2010. A new wave of cellular imaging. Annu. Rev. Cell Dev. Biol. 26, 285–314. doi:10.1146/annurev-cellbio-100109-104048

Villén, J., Beausoleil, S.A., Gerber, S.A., Gygi, S.P., 2007. Large-scale phosphorylation analysis of mouse liver. Proc Natl Acad Sci USA 104, 1488–1493. doi:10.1073/pnas.0609836104

Yan, L., Sun, S., Wang, W., Shi, J., Hu, X., Wang, S., Su, D., Rao, Z., Hu, J., Lou, Z., 2015. Structures of the yeast dynamin-like GTPase Sey1p provide insight into homotypic ER fusion. The Journal of Cell Biology 210, 961–972. doi:10.1083/jcb.201502078

Zhao, G., Zhu, P.-P., Renvoisé, B., Maldonado-Báez, L., Park, S.H., Blackstone, C., 2016. Mammalian knock out cells reveal prominent roles for atlastin GTPases in ER network morphology. Experimental Cell Research. doi:10.1016/j.yexcr.2016.09.015

Zhao, J., Hedera, P., 2012. Hereditary spastic paraplegia-causing mutations in atlastin-1 interfere with BMPRII trafficking. Mol. Cell. Neurosci. doi:10.1016/j.mcn.2012.10.005

# APPENDIX A

# DISRUPTED HYDROGEN BOND NETWORK IMPAIRS ATPASE ACTIVITY IN AN HSC70 CYSTEINE MUTANT [#]

## ABSTRACT

Enzyme activity relies on proper active-site geometry. Within an enzyme active-site, optimal positioning and orientation of certain amino acids facilitates substrate binding and catalysis. Often these essential active-site residues are among the most highly conserved within the enzyme. The ATPase domain of 70-kilodalton heat shock protein (Hsp70) family members exhibits some of the highest evolutionary and structural conservation known. This conservation not only includes residues responsible for substrate binding and catalysis, but can be extended to residues globally located within the substrate-binding pocket. Arguably for Hsp70 proteins, the most intriguing of these conserved residues is a cysteine in close proximity, but not in contact with the nucleotide substrate. Prior studies focused on several Hsp70 family members suggest that, while this cysteine is not required for Hsp70 ATPase activity, select changes to this residue (through amino acid substitution) can dramatically alter ATP hydrolysis. Post-translational modification of this cysteine has also been reported for several Hsp70s, and modification has been demonstrated to limit ATP hydrolysis. To better understand the underlying mechanism for how perturbation of this non-catalytic residue modulates Hsp70 function, we solved the structure for a cysteine-to-tryptophan mutation in the constitutively-expressed mammalian Hsp70 family member Hsc70. Our work reveals that the steric hindrance produced by a cysteine-to-tryptophan mutation disrupts the

hydrogen-bond network within the active-site and also results in a loss of proper catalytic magnesium coordination. We propose that a similarly altered active-site is likely observed upon post-translational oxidation. We speculate as to how the subtle changes we observed in the hydrogen-bonding network may relate to the previously reported observation that cysteine oxidation can influence Hsp70 inter-domain communication.

---

# The following sections comprise a forthcoming manuscript. Contributors include John P. O'Donnell, Heather M. Marsh, Holger Sondermann, and Carolyn S. Sevier.

## INTRODUCTION

The Hsp70 family member proteins are a class of molecular chaperones that mediate various protein folding processes and are evolutionarily present from archaea to eukaryotes (Lindquist and Craig, 1988). Functionally, these molecular chaperones fulfill a range of roles including nascent polypeptide folding, refolding of destabilized polypeptides, stabilizing mature proteins, clearance of aggregated proteins, and transport of proteins across organelle membranes (Cyr and Neupert, 1996; Frydman et al., 1994; Hjerpe et al., 2016; Mashaghi et al., 2016; Sharma et al., 2010). The conserved protein folding activity of Hsp70 family members relies on two domains; a nucleotide-binding domain (NBD) which is connected to a substrate-binding domain (SBD) via flexible linker. These core components are regulated though the binding and hydrolysis of ATP (Daugaard et al., 2007; Mayer and Bukau, 2005). Mechanistically, the NBD and the SBD are bidirectionally coupled (Mayer, 2013). Peptide binding to the SBD stimulates ATP-hydrolysis within the NBD. When the NBD binds ATP, the SBD assumes an open conformation and is partially associated with the NBD. This open-state confers fast on/off rates and low affinity for substrate. Upon ATP-hydrolysis, a closing of the SBD occurs which decreases the off rates and increases the affinity for substrate (Mayer, 2013; Young, 2010). Numerous means of allosteric inter-domain communication have been proposed and include: a nucleotide sensing proline switch (Vogel et al., 2006a), linker-NBD electrostatic interactions (Jiang et al., 2005; Vogel et al., 2006b), and sub-domain conformational changes of the NBD (Bhattacharya et al., 2009; Ung et al., 2013).

One striking feature of Hsp70s is their high degree of active site conservation between family members. Evolutionary tracing of over 1600 Hsp70 NBDs indicates that the key residues reported for enzymatic activity exhibit a robust conservation ranking and low frequency mode analysis of the same residues indicate they are spatially immobile (Liu et al., 2010). This suggests that in addition to the high degree of evolutionary conservation, the active-sites of Hsp70s adopt a very specific set of geometries required for proper activity. This notion is corroborated by the numerous crystal structures of Hsp70 members deposited in the Protein Data Bank whose active site geometries are nearly indistinguishable. Comparing the nucleotide binding site of twenty structures from the Protein Data Bank to wild-type Hsc70 (*structure from this study*) illustrates a high degree of structural similarity with an average RMSD of 0.32 ± 0.07 Å and range between 0.21 and 0.48 Å (**Figure A.1A**).

Another feature of Hsp70 family members is a conserved active-site cysteine that is found in many bacterial, plant, and eukaryotic Hsp70 family members **(Figure A.1B)**. Evolutionarily, cysteine residues exhibit unusual patterns of conservation with some of the highest and lowest mutational rates (Marino and Gladyshev, 2010). This argues that when conserved, cysteines tend to exhibit niche functions that only the unique physiochemical properties of a thiol side chain can fulfill. In line with these assumptions, the Hsp70 family members active-site cysteine can be modified and subsequently change enzymatic function (Carbone et al., 2004; Chang et al., 2010; Chirico et al., 1998; Hermawan and Chirico, 1999; Miyata et al., 2013; 2012; Wang et al., 2014; Wang and Sevier, 2016; H. Zhang et al., 2016).

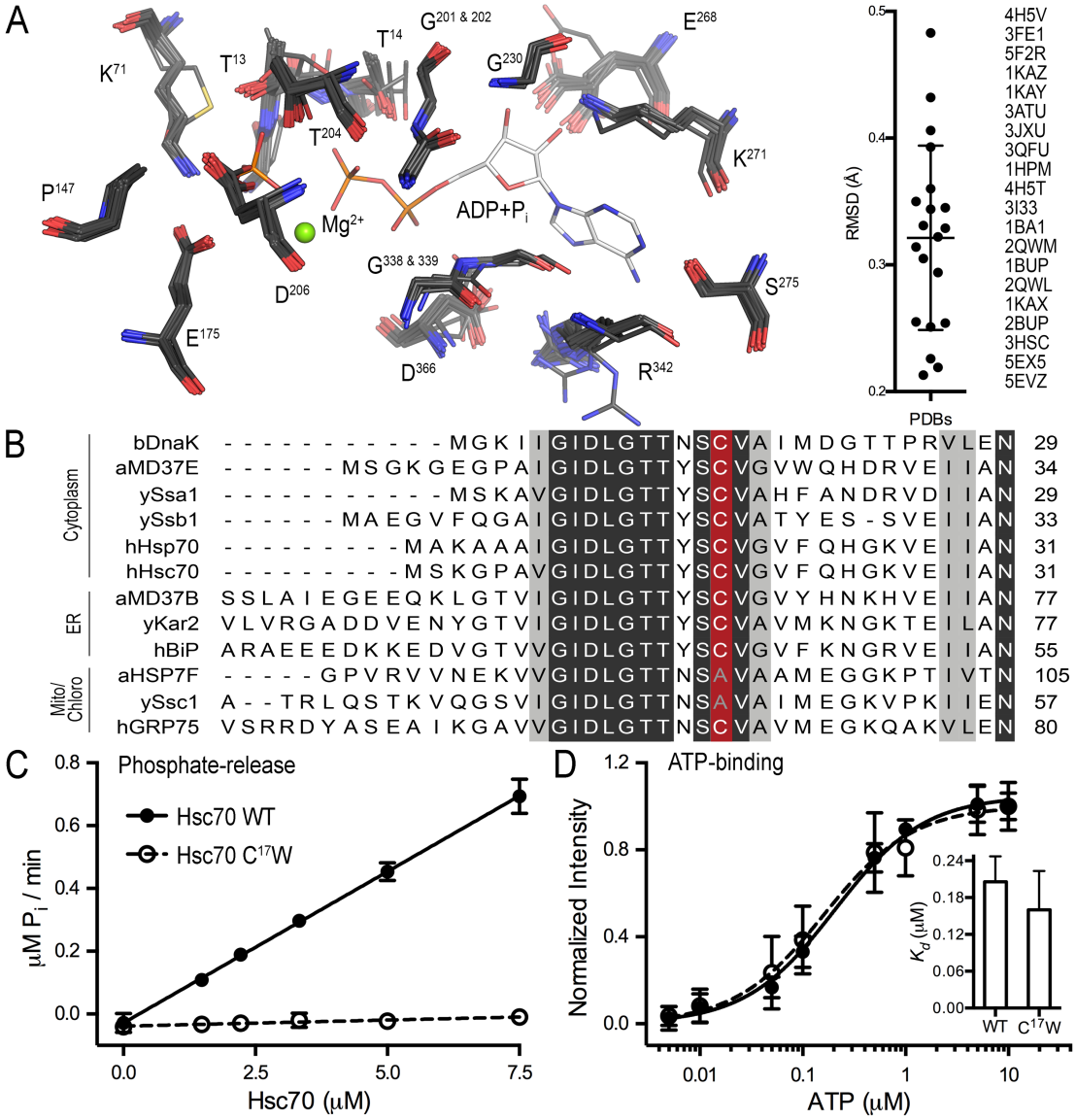


**Figure A.1. Active-site cysteine mutation in Hsc70 impedes ATPase activity but not binding. (A)** Hsp70 family structural overlay of residues within 4 Å of adenosine-nucleotides with RMSD calculations made between various Hsp70 members and the wild-type Hsc70 structure from this study (Arakawa et al., 2011; Flaherty et al., 1990; Hughes et al., 2016; Jiang et al., 2007; O'Brien et al., 1996; Sousa and McKay, 1998; Wilbanks and McKay, 1998; 1995; Wisniewska et al., 2010; Yan et al., 2011; Z. Zhang et al., 2015). **(B)** Sequence alignment of bacterial, plant, and eukaryotic Hsp70s originating from various organelles are colored as following: conserved active-site cysteine (red), fully conserved residues (black), and similar side chain identity (gray). **(C)** Phosphate-release kinetics of Hsc70 wild-type and C$^{17}$W. **(D)** ATP-binding curve for Hsc70 wild-type and C$^{17}$W; inset shows $K_d$ values. Graphs showing means and standard deviation (SD) are plotted from a minimum of two biological replicates with three technical repeats each.

One such cysteine modification has recently been shown to control inter-domain communication and is required for maintaining cellular homeostasis during redox stress (Wang et al., 2014; Wang and Sevier, 2016) The endoplasmic reticulum (ER) is site of oxidative protein folding and incurs a large flux of reactive oxygen species during the formation of disulfide bonds (Sevier et al., 2007; Tu and Weissman, 2004). Upon stress, the yeast ER resident Hsp70 chaperone Kar2 (also known as HSPA5, GRP78, and BiP in humans), has been shown to be post-translationally modified at the active-site cysteine. Reversible modification of this cysteine through sulfenylation and glutathionylation has been shown to increase the ability of BiP to prevent protein aggregation (Wang et al., 2014; Wang and Sevier, 2016). In contrast to the bidirectional allostery described for the unmodified enzyme, these post-translational modifications obstruct the ATPase function, thus, decoupling the classic mechanism of inter-domain communication. This allosteric decoupling has been described for other chaperones including Hsp70 when bound to the small molecule YM-08 and DnaK when mutated; in both cases, ATPase activity is impeded while binding to misfolded proteins and aggregation prevention is promoted (Chang et al., 2010; Miyata et al., 2013). There are additional biochemical reports of cysteine modifications modulating function of Hsp70s, however, their mechanisms remain to be determined (Carbone et al., 2004; Chirico et al., 1998; Hermawan and Chirico, 1999; Miyata et al., 2012; Winter et al., 2005; H. Zhang et al., 2016).

Due to the high degree of sequence conservation and a common trend of active-site cysteine modifications among Hsp70s, we set out to structurally determine general mechanisms of how perturbation of the active-site can change enzymatic function.

Using Hsc70 as a model, we introduced a cysteine-to-tryptophan mutation in the active site. Targeting this location is beneficial because it is relevant to numerous Hsp70 family members and allows us to generalize mechanisms involved in activity modulation. In addition, this genetic-mimetic has proved to be a valuable proxy for understanding active-site cysteine oxidation in yeast BiP (Kar2p) as expression of $C^{63}W$ rescues growth defects during redox stress in strains devoid of their active-site cysteine (Wang et al., 2014). Beyond yeast, proteomic approaches have verified that the active-site cysteine in human Hsc70 can be sulfinylated and sulfonylated *in vivo* (Lee et al., 2013). Here we describe the structural basis for a disrupted hydrogen-bond network in the active-site and loss of the catalytic magnesium coordination. We propose that these perturbations cause the loss of ATPase activity reinforcing the importance of the active-site architecture of Hsp70 family members as well as providing clues into decoupling allostery in cases of post-translational modification.

## RESULTS

*Hsc70 $C^{17}W$ mutation impairs ATP-hydrolysis but not binding.*

First, we determined turnover number ($k_{cat}$) of ATP-hydrolysis measured by phosphate release kinetics for the near full-length Hsc70 protein (5-554). The $k_{cat}$ value for wild-type Hsc70 was determined to be 0.096 ± 0.002 $min^{-1}$ which is in agreement to published reports and Hsc70 $C^{17}W$ exhibits severely impaired catalytic activity ($k_{cat}$ = 0.004 ± 0.001 $min^{-1}$) (Sadis and Hightower, 1992) **(Figure A.1C)**. Loss of ATPase activity is in agreement with previous studies interrogating active-site cysteine mutations that comprised large amino acid substitutions such as Hsc70 cysteine-to-lysine, and BiP cysteine-to-tryptophan mutations resulted in the inability to hydrolyze ATP (Wang et al., 2014; Wilbanks and McKay, 1998; Xu et al., 2016). However, not all Hsp70s have an active-site cysteine which argues that it is not required for catalysis (**Figure A.1B**). This idea is supported by the BiP cysteine-to-alaine mutation which is a functioning ATPase (Wang et al., 2014). Therefore, we hypothesized that the large side chain of tryptophan was effecting ATP-hydrolysis through a change in nucleotide affinity. To test this, we conducted a differential radial capillary action of ligand assay (DRaCALA) using $^{32}$P-ATP and Hsc70 that was devoid of bound nucleotide (Roelofs et al., 2011). Spotting a mixture of protein/$^{32}$P-ATP of varying concentrations onto nitrocellulose enables immobilization of protein while free ligand can diffuse radially through capillary action. Quantification of the amounts of free and protein bound ligand allows for determination of binding constants (Roelofs et al., 2011). Dissociation constants ($K_d$) for ATP-binding to wild-type and $C^{17}W$ indicate comparable affinities of 0.21 ± 0.04 and 0.16 ± 0.06 μM respectively **(Figure A.1D)**. The $K_d$ values obtained from our DRaCALA experiments

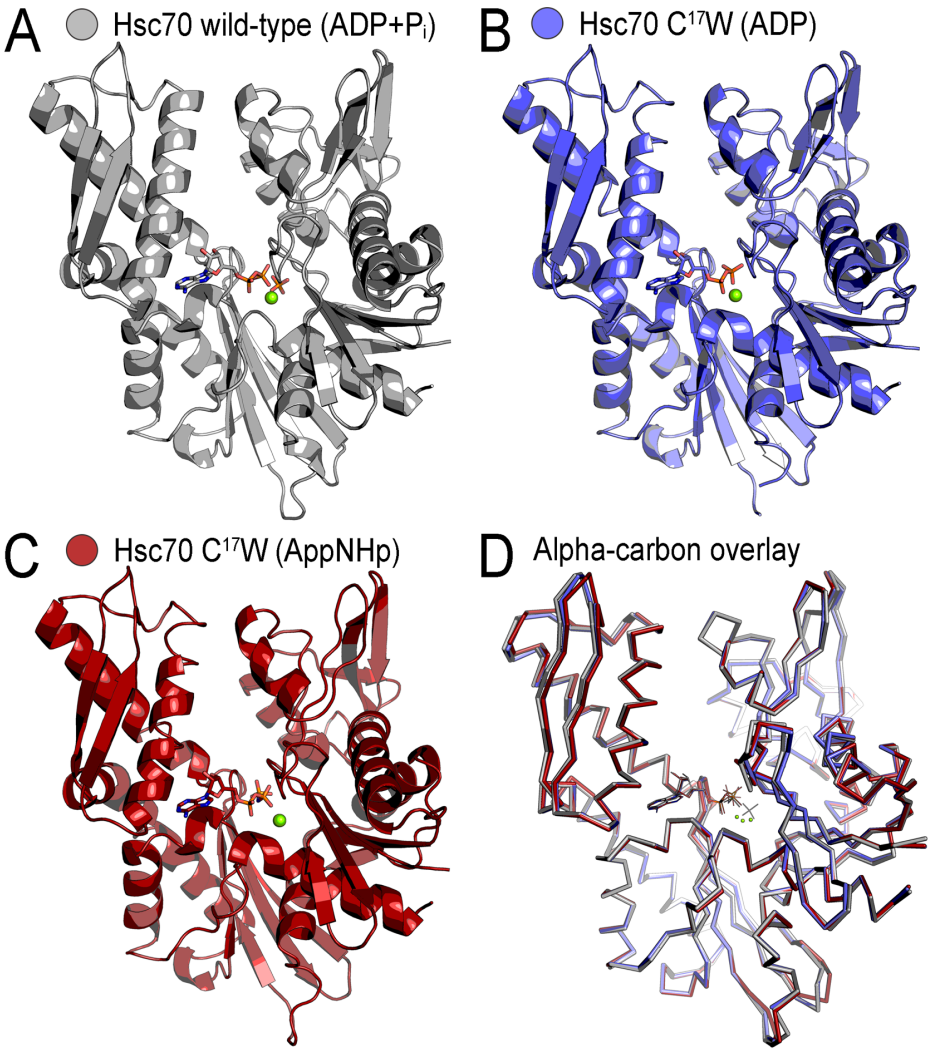


**Figure A.2. Structures Hsc70 wild-type and C$^{17}$W bound to adenosine nucleotides.** Crustal structures of Hsc70 **(A)** wild-type bound to $Mg^{2+}$•ADP+$P_i$, **(B)** C$^{17}$W bound to $Mg^{2+}$•ADP, and **(C)** C$^{17}$W bound to AppNHp. **(D)** Alpha-carbon overlay depicts high degree of similarity between structures.

share values of published results for the wild-type protein (Buxbaum and Woodman, 1996; O'Brien and McKay, 1995; Sullivan et al., 2001; Wei and Hendershot, 1995).

*Crystal structures of Hsc70 wild-type and $C^{17}W$ reveals a mechanism for loss of ATPase activity.*

We determined three crystal structures of the NBD fragment (residues 5-381) of Hsc70 **(Figure A.2)**. The wild-type protein bound to $Mg^{2+}$•ADP+$P_i$ diffracted X-rays to 2.3 Å **(Figure A.2A),** and $C^{17}W$ proteins bound to $Mg^{2+}$•ADP **(Figure A.2B)** and $Mg^{2+}$•AppNHp **(Figure A.2C)** diffracted X-rays to 1.8 Å and 1.9 Å respectively. All three structures are in space group $P2_1$ with two molecules in the asymmetric unit **(Table A. 1)**. Globally, the three structures closely resemble one another as depicted by the alpha-carbon backbone overlay; structures have root mean square values of 0.41 for both $C^{17}W$ $Mg^{2+}$•ADP and $C^{17}W$ $Mg^{2+}$•AppNHp when compared to wild-type **(Figure A.2D)**.

Despite global similarities, analysis of the active-site reveals defects in magnesium-nucleotide coordination in the $C^{17}W$ mutants. Initial analysis of the post-hydrolysis wild-type $Mg^{2+}$•ADP+$P_i$ structure indicates a strong correlation of active-site geometries to previously published structures (Flaherty et al., 1990; Hughes et al., 2016; Sousa and McKay, 1998; Wilbanks and McKay, 1995; Wisniewska et al., 2010; Z. Zhang et al., 2015). A magnesium ion induces the formation of a bidentate complex with the β-phosphate of ADP and the hydrolyzed ɣ-phosphate. The bidentate complex is further stabilized through water molecules which are positioned by $D^{10}$, $K^{71}$, $E^{175}$, $D^{199}$ (Flaherty et al., 1994) **(Figure A.3A)**. Location of $K^{71}$ which is believed to facilitate the nucleophilic attack via positioning a water molecule in line with the ɣ-phosphate is also

| Table A.1: X-ray data collection and refinement statistics. | | | |
|---|---|---|---|
| | Hsc70 wild-type $Mg^{2+}$•ADP+$P_i$ (Residues 5-381) | Hsc70 $C^{17}W$ $Mg^{2+}$•AppNHp (Residues 5-381) | Hsc70 $C^{17}W$ $Mg^{2+}$•ADP (Residues 5-381) |
| **Data Collection** | | | |
| X-ray source | CHESS | CHESS | CHESS |
| Wavelength | 0.977 | 0.977 | 0.977 |
| Space group | P 1 21 1 | P 1 21 1 | P 1 21 1 |
| Unit cell | | | |
| a, b, c (Å) | 73.8, 79.2, 76.3 | 73.8, 78.3, 77.9 | 73.4, 77.6, 75.5 |
| α, β, γ (°) | 90, 101.4, 90 | 90, 101.4, 90 | 90, 101.2, 90 |
| Resolution (Å)[a] | 39.6 - 2.3 | 40.53 - 1.9 | 37.05 - 1.8 |
| | (2.382 - 2.3) | (1.968 - 1.9) | (1.864 - 1.8) |
| Number of Reflections | | | |
| Total | 70363 (7569) | 130588 (11452) | 151942 (14639) |
| Unique | 35280 (3823) | 66371 (6301) | 76539 (7525) |
| Completeness (%) | 91.52 (97.05) | 99.41 (95.21) | 99.20 (98.34) |
| Multiplicity | 2.0 (2.0) | 2.0 (1.8) | 2.0 (1.9) |
| I/σ(I) | 11.97 (2.20) | 10.55 (1.73) | 8.33 (1.98) |
| $R_{meas}$ (%) | 8.1 | 9.8 | 10.1 |
| $R_{merge}$ (%) | 5.8 | 7.0 | 7.2 |
| CC1/2 | 0.995 (0.84) | 0.994 (0.623) | 0.993 (0.724) |
| CC* | 1.00 (0.96) | 0.998 (0.876) | 0.998 (0.916) |
| **Refinement** | | | |
| $R_{work}$ / $R_{free}$ (%) | 19.6 / 24.7 | 18.1 / 22.9 | 19.0 / 22.9 |
| rms deviations | | | |
| Bond length (Å) | 0.003 | 0.006 | 0.007 |
| Bond angles (°) | 0.93 | 1.12 | 1.21 |
| No. of atoms | | | |
| Protein | 5743 | 5885 | 5860 |
| Ligands | 76 | 64 | 56 |
| Water | 367 | 865 | 828 |
| Ave. B-factors (Å$^2$) | | | |
| Protein (total) | 26.9 | 19.5 | 20.1 |
| Ligands | 24.4 | 13.5 | 9.9 |
| Water | 25.6 | 29.3 | 29.5 |
| Ramachandran (%) | | | |
| Favored | 97.9 | 98.8 | 98.7 |
| Outliers | 0 | 0 | 0 |

(a) Values in brackets are fore the highest resolution bin.

maintained (O'Brien et al., 1996) **(Figure A.3A)**. This same active-site configuration is present in the pre-hydrolysis state of GRP78 bound to the non-hydrolyzable analog $Mg^{2+}$•AppCHp, which reinforces the high degree active-site conservation between Hsp70 members (PDB: 5F2R) (Hughes et al., 2016) **(Figure A.3B)**.

The major difference between wild-type and $C^{17}W$ structures is the location of the magnesium ion. The structural basis for displacing the magnesium ion is contingent on a water molecule (denoted $H_20^{‡}$) that hydrogen-bonds with the backbone carbonyl of $D^{366}$, carboxylic acid of $D^{10}$, α-phosphate of the nucleotide, and an additional water molecule in wild-type structures (**Figure A.3A and A.3B**). The tryptophan mutation introduces a steric hindrance in the vicinity of the $H_20^{‡}$ molecule which is absent in both $C^{17}W$ $Mg^{2+}$•ADP and $C^{17}W$ $Mg^{2+}$•AppNHp structures (**Figure A.3C and A.3D**). Without $H_20^{‡}$ , the canonical hydrogen-bonding network in the active-site is disrupted. To achieve proper magnesium coordination in the $C^{17}W$ $Mg^{2+}$•ADP structure, the magnesium gains a direct interaction with the α-phosphate of ADP which causes the ion to recede from the catalytic residues (**Figure A.3C**). The $C^{17}W$ $Mg^{2+}$•AppNHp accommodates active-site changes through direct engagement between the carboxylic acid moiety of $D^{10}$ and magnesium instead of $D^{10}$ stabilized water (or potassium; *see Discussion*) molecules to coordinate magnesium as seen in other structures (**Figure A.3D**).

Additionally, a critical water-bridge hydrogen bond is lost between the $Mg^{2+}$•nucleotide and residues $E^{175}$, $K^{71}$, and D199 (the water is denoted $H_20^{*}$) (**Figure A.3**). This water-bridged hydrogen bond has been proposed to be required for inter-domain allostery by the sensing of the nucleotide-bound state of the NBD which is relayed to the SBD via proline switch mechanism (Vogel et al., 2006a).

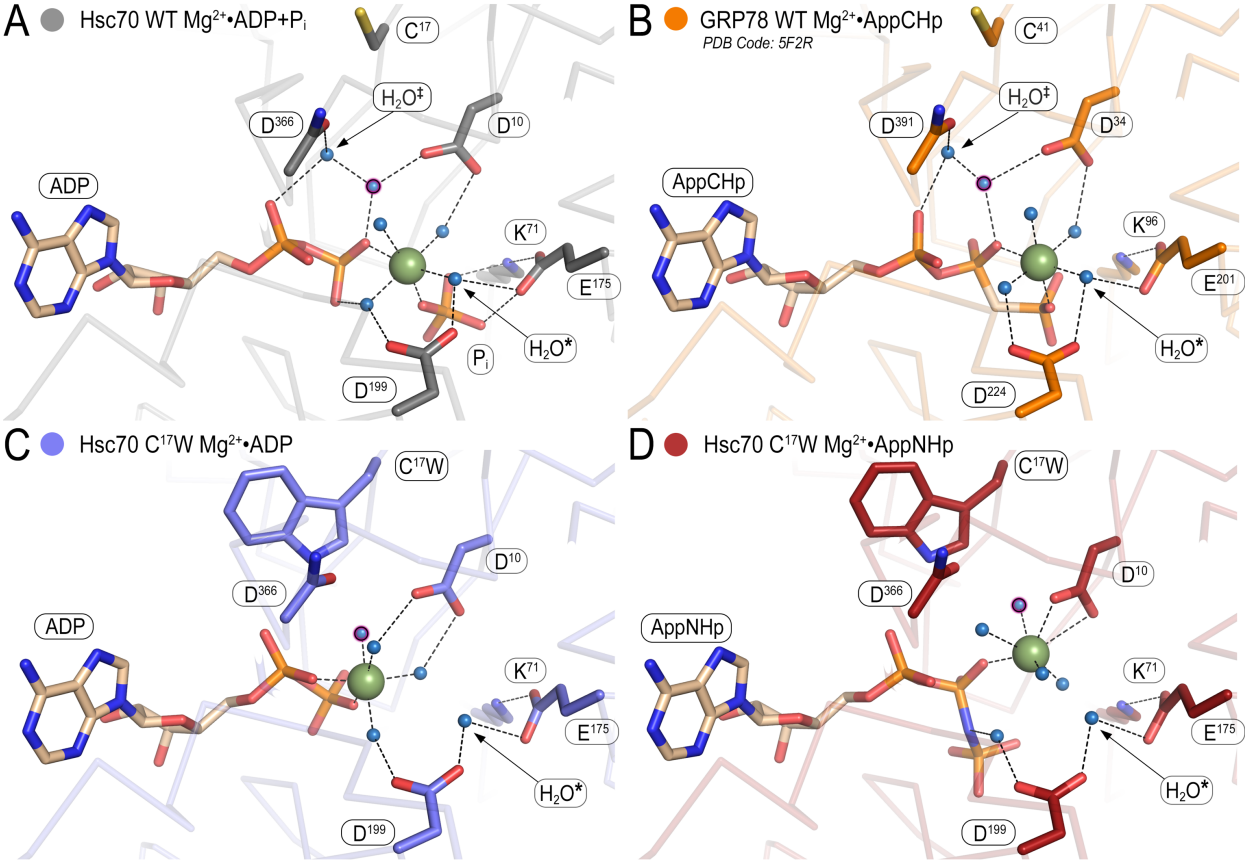


**Figure A.3. Structures of wild-type and mutant Hsc70 depict a disrupted hydrogen bond network and defected magnesium-nucleotide coordination. (A)** Hsc70 wild-type active-site representing the post-hydrolysis state bound to ADP+$P_i$ (*gray*) has all canonical residues and water molecules making proper contacts. **(B)** For comparison, the pre-hydrolysis state of GRP78 (*PDB: 5F2R; orange*) displays analogous active site geometries to that of the wild-type structure from this study. **(C)** Hsc70 $C^{17}W$ bound to ADP (*slate*) looses $Mg^{2+}$ coordination via $H_2O^*$ and the steric hindrance of the introduced tryptophan mutation displaces $H_2O^‡$ which is absent from the active-site. **(D)** Hsc70 $C^{17}W$ bound to AppNHp (*dark red*) displays a similarly compromised active site configuration to the ADP bound structure. Additionally, the $Mg^{2+}$ coordination is further defected and directly interacts with $D^{10}$.

Crystal structures of Hsp70 family members were compared to determine if the displacement of the magnesium ion in our mutant structures was a unique active-site configuration. Wild-type and mutant Hsp70 member structures from bacteria and eukaryotes that are bound to ligand (ADP, ATP, ADP+$P_i$, AppCHp, ADP•$VO_4$, $P_i$, or 7-deazaATP) and a magnesium were selected for analysis. The structures were aligned to the Hsc70 wild-type $Mg^{2+}$•ADP+$P_i$ structure from this study. The 25 aligned crystal structures (including the three from this study) exhibited a high degree of similarity compared to our wild-type structure with a range of RMSD values for eukaryotes being 0.34 - 0.70 Å and an RMSD value for DnaK = 3.3 Å (**Figure A.4A**). Inspection of the $Mg^{2+}$•nucleotides from the aligned structures indicates a strong preponderance for magnesium ions to reside in the same location with only the magnesiums from our $C^{17}W$ structures deviating from the group (**Figure A.4B**). Magnesium displacement was calculated by measuring the distance between the magnesium ions using our wild-type structure as the reference which gives a mean displacement of 0.27 ± 0.03 Å for magnesiums located within the cluster (**Figure A.4C)**. The magnesium ions in the $C^{17}W$ mutants were significantly displaced by a distance of 2.1 and 1.9 Å for $Mg^{2+}$•AppNHp and $Mg^{2+}$•ADP structures respectively (**Figure A.4C**).

*Magnesium is required for nucleotide sensing in wild-type but not $C^{17}W$.*

Since the change in catalytic magnesium location was distinct for the $C^{17}W$ mutant crystal structures, we assessed the ability of nucleotide and/or magnesium to confer temperature dependent stability in the near full-length protein using an established fluorescence-based thermal shift assay (Lo et al., 2004). Nucleotide-

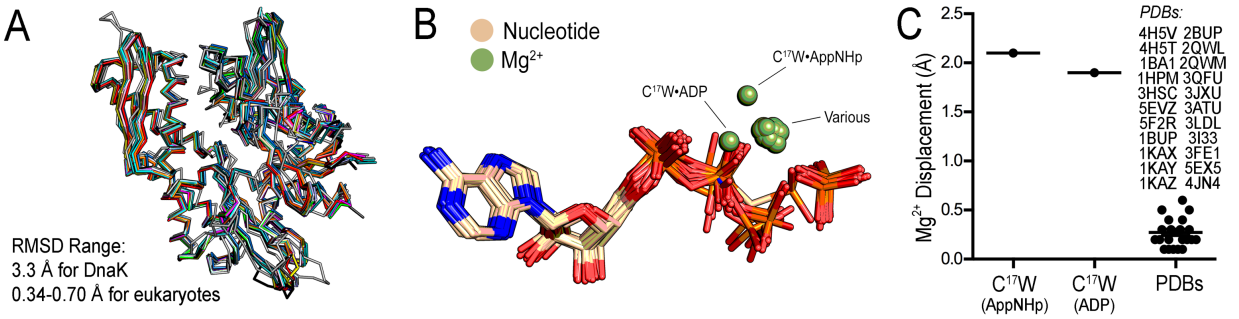


**Figure A.4. The Hsc70 C$^{17}$W mutation causes a significant displacement of the catalytic magnesium ion. (A)** Structural overlay of twenty-five Hsp70 family members indicates the high-degree of similarity amongst proteins (Arakawa et al., 2011; Flaherty et al., 1990; Hughes et al., 2016; Jiang et al., 2007; Macias et al., 2011; O'Brien et al., 1996; Qi et al., 2013; Sousa and McKay, 1998; Wilbanks and McKay, 1998; 1995; Wisniewska et al., 2010; Yan et al., 2011; Z. Zhang et al., 2015). **(B)** Ligand overlays from the same structure depict indistinguishable magnesium locations for the aligned Hsp70 members. The only two magnesiums that deviate belong to the C$^{17}$W structures. **(C)** Quantification of the measured magnesium displacement distances; mean and SD are displayed.

dependent stability was first tested in the presence of magnesium for wild-type Hsc70. Addition of either ADP or ATP in the presence of magnesium increased the $T_m$ value of the wild-type protein by more than 10ºC and a nucleotide specific stabilization effect was seen when comparing $Mg^{2+}$•ATP and $Mg^{2+}$•ADP with a $\Delta T_m$ = 3ºC (**Figure A.5A; left**). Interestingly, both ADP and ATP stabilize the wild-type protein when magnesium is omitted, but the nucleotide specific stabilization effect was lost (**Figure A.5A; center**). This suggests that the magnesium is required for sensing differences between ADP and ATP (**Figure A.5A; right**). Based on magnesium displacement and loss of coordination, we would predict magnesium would not elicit the same nucleotide recognition as seen for wild-type. Similarly, both ADP and ATP in the presence of magnesium stabilized the C$^{17}$W protein by $\Delta T_m$ of 13.4 and 15 ºC for ADP and ATP respectively when compared

to the apo protein (**Figure A.5B; left**). When magnesium is omitted, the protein can still discriminate between the bound nucleotide species, but the ADP bound state displays a stronger stability than ATP (**Figure A.5B; center**). In contrast to wild-type protein, a significant thermal shift exists for $C^{17}W$ protein both with the addition or omission of magnesium; however, nucleotide-specific stability does not correlate with presence of magnesium (**Figure A.5B; right**). The global stability is $C^{17}W$ is also substantially decreased when compared to the wild-type protein (**Figure A.5**).

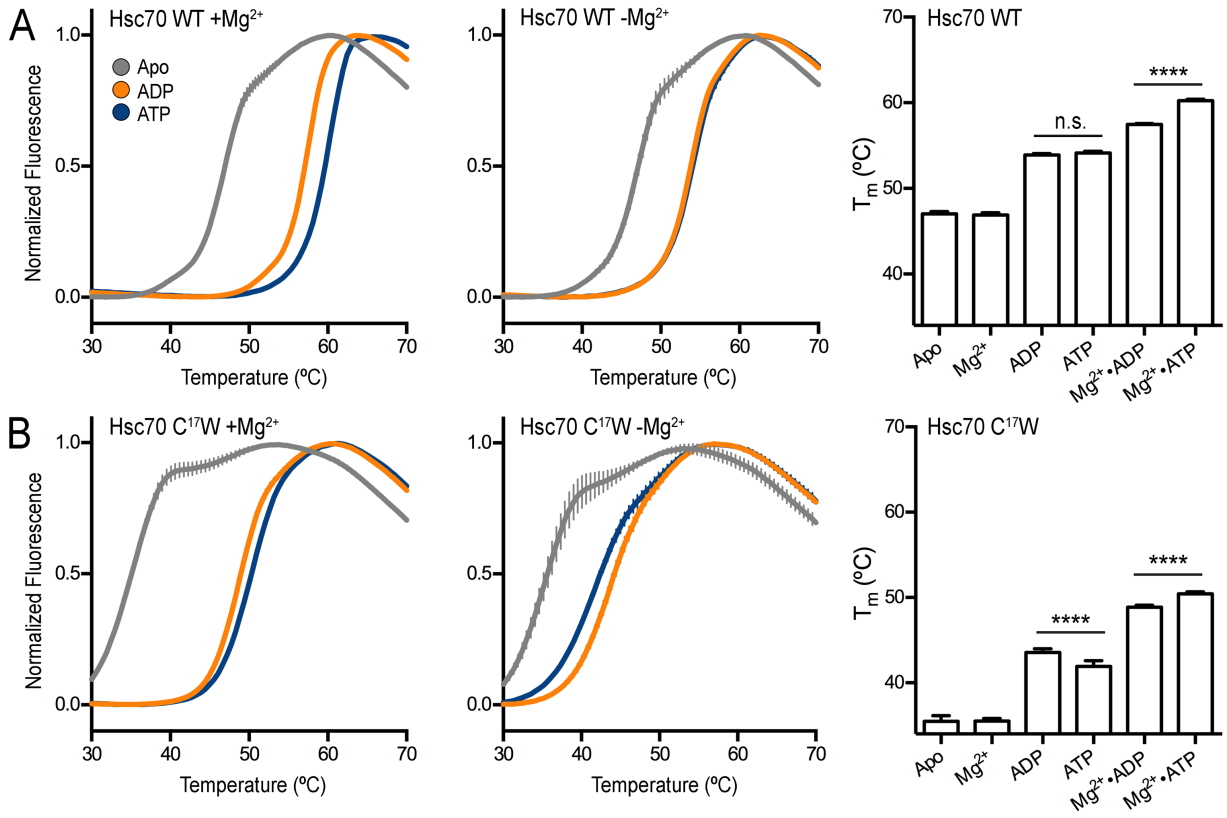


**Figure A.5. Thermal stability assay indicates magnesium is required for nucleotide identification in the wild-type but not C$^{17}$W proteins. (A)** Thermal melting data for Hsc70 wild-type in the apo, ADP-, or ATP-bound states with or without magnesium. The presence of magnesium enables ADP and ATP to be differentiated (*left*). Samples lacking magnesium but are bound to nucleotide are stably equivalent (*center*). $T_m$ values determined from the second derivative are displayed at right. **(B)** Thermal melting data for Hsc70 C$^{17}$W under the same experimental conditions as wild-type. With or without magnesium (*left and center respectively*), mutant protein exhibits differential stabilities depending on the nucleotide bound; $T_m$ values are displayed on right. Graphs showing means and SD are plotted from a minimum of two biological replicates with three technical repeats each.

## DISCUSSION

Here, we establish the structural basis for impaired ATPase activity of Hsc70 upon introducing steric hindrance positionally located at a conserved active-site cysteine (**Figures A.1-A.6**). We propose that steric hindrance disrupts a hydrogen-bond network in the active-site and loss of catalytic magnesium coordination both contribute to impaired ATPase activity. There is ample evidence that the active-site architecture of Hsp70s are highly conserved and strict geometric guidelines are required for activity (Flaherty et al., 1994; Liu et al., 2010; O'Brien et al., 1996; Wilbanks et al., 1994) (**Figures A.1 and A.4**). Our study indicates that slight perturbations to the active-site results in structural changes leading to loss of function phenotypes. Disruption of a hydrogen-bonding network and loss of catalytic magnesium coordination both may be mechanistically generalizable to account for other active-site defects and post-translational modifications.

Mechanistically, we conclude that the loss of ATPase activity is not due to the inability to bind nucleotide as the $K_d$ of ATP for wild-type and $C^{17}W$ proteins are equivalent (**Figure A.1D**). Additionally, two independent structures of Hsc70 $C^{17}W$ clearly depict densities for $Mg^{2+}$•ADP and $Mg^{2+}$•AppNHp (**Figure A.3C and A.3D**). Based on a comparative analysis of wild-type and mutant crystal structures, we propose that a water molecule (denoted $H_20^{‡}$) is missing from the $C^{17}W$ mutant proteins and is a result of steric hindrance that is imposed by the tryptophan residue. This perturbation disrupts a conserved hydrogen-bond network in the active-site (**Figure A.4A**) (Hughes et al., 2016; Mayer, 2013; O'Brien et al., 1996). The disruption of the hydrogen-bond

network causes a 2 Å displacement of the catalytic magnesium and loss of proper coordination that is required for ATP-hydrolysis (**Figure A.3C, A.3D, A.4B, and A.4C)**.

It is important to note that there are two potassium binding sites that have been characterized in the active-site of Hsc70 by calculating anomalous difference Fourier maps (Wilbanks and McKay, 1995). Despite having positive electron density at the same position that has previously been assigned to potassium ions, we were unable to unambiguously determine if potassium ions were present in our structures. Nonetheless, we modeled water molecules to the the corresponding density and denoted them with a pink halos in **Figure A.3**. One of the characterized potassium binding sites stabilizes components of the disrupted hydrogen-bond network in our mutant structures. In the $Mg^{2+}$•ADP structure the corresponding water molecule remains in the same location as the wild-type structure; however, in the $Mg^{2+}$•AppNHp structure this corresponding water molecule shifts 1.1 Å toward the carboxylic acid of $D^{10}$ (**Figure A.3C and A.3D**).

Because $C^{17}$ is in close proximity to the potassium binding site, authors in a previous study attempted to replace the active-site potassium by the ε-amino group of lysine through a $C^{17}K$ mutation (Wilbanks and McKay, 1998). Hypothetically, the $C^{17}K$ mutation would structurally resemble the active-site of actin where the ε-amino of $K^{17}$ occupies the potassium binding site of Hsc70 (Kabsch et al., 1990). Authors did not achieve a functional replacement with the $C^{17}K$ mutant as a strong loss of ATPase activity was observed. However, authors infer from the $C^{17}K$ crystal structure that impaired catalytic capacity of the mutant emphasizes the sensitivity of Hsc70 catalytic site to subtle perturbations (Wilbanks and McKay, 1998). This interpretation is akin to

our observations, but the active-site of $C^{17}W$ is more severely compromised than the other Hsp70 structures analyzed in this study.

An additional structural difference between wild-type and $C^{17}W$ proteins is the loss of a critical water-bridge hydrogen bond. The compromised interaction between $H_2O$*, $Mg^{2+}$•nucleotide and residues $E^{175}$, and $K^{71}$ has been proposed to change the SBD conformation by inducing a positional shift in the peptide backbone which is relayed through an arginine residue to elicit an change in SBD conformation. Authors hypothesize that changing alpha-carbon backbone is largely responsible for overcoming the energy barrier for allostery because a introduction of backbone flexibility via glycine mutation exhibits a drastic reduction in enthalpy of activation and that this mechanism is bidirectional (Vogel et al., 2006a).

Thermal shift data for the near full-length protein supports the hypothesis that the $C^{17}W$ mutants loose proper magnesium localization with the obvious outcome being ATP-hydrolysis impairment; however, more subtle mechanisms such as nucleotide sensing may also be compromised. Wild-type Hsc70 requires the $Mg^{2+}$•nucleotide adduct to differentiate between ADP or ATP; without magnesium, the nucleotide specific stability is lost (**Figure A.5A**). Hsc70 $C^{17}W$ can differentiate between bound ADP and ATP with or without magnesium present which is most likely due aberrant nucleotide coordination in the active site (**Figure A.5B**). The global thermo-stability of $C^{17}W$ is also largely compromised when compared to the wild-type structure (**Figure A.5**). Despite wild-type and mutant structures being very similar (RMSD = 0.41 Å), the static structures do not inform us about the change in dynamics caused by perturbing the active-site. This may be one explanation why other hydrolysis deficient mutations are

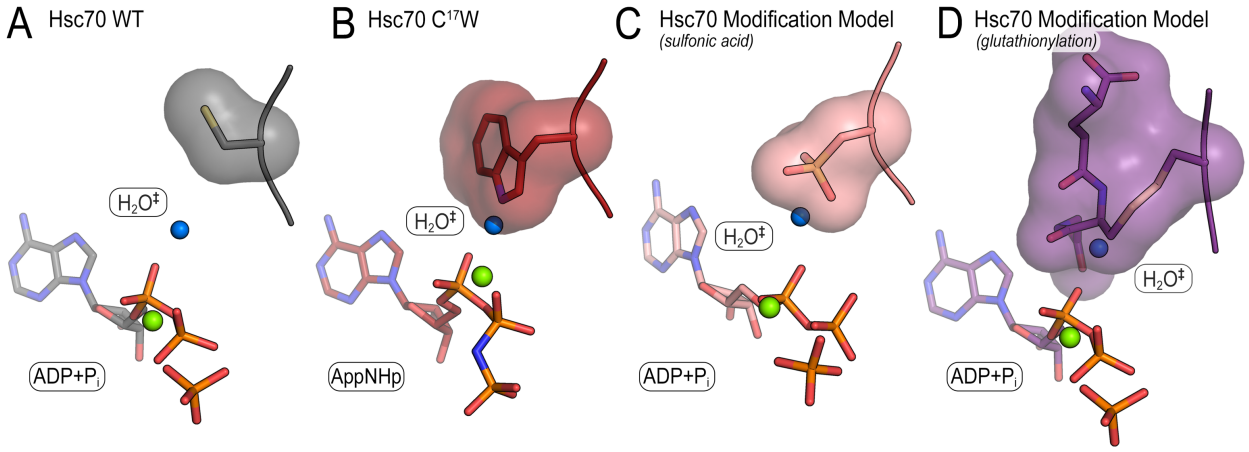


**Figure A.6. Hypothetical models of sulfonic acid and glutathione cysteine modifications for size and orientation comparisons. (A)** Hsc70 wild-type structure from this study displaying $H_2O‡$ and the solvent-excluded surface of $C^{17}$. This structure was used in the sulfonic acid and glutathione modeling. **(B)** Hsc70 $C^{17}W$ structure bound to AppNHp showing the solvent-excluded surface of $C^{17}W$ and the overlapping location of $H_2O‡$ from the wild-type structure. **(C)** Solvent-excluded surface of sulfonic acid modeled onto $C^{17}$ displays a similar size to $C^{17}W$ and also comes in close contact to $H_2O‡$. **(D)** Solvent-excluded surface of glutathione modeled onto $C^{17}$ occupies a much larger space in the active site when compared to tryptophan and sulfonic acid. Glutathione fully displaces $H_2O‡$.

unlike $C^{17}W$ and do not rescue stress protection phenotypes seen *in vivo* (Wang et al., 2014; Xu et al., 2016).

Introducing the $C^{17}W$ mutation caused numerous structural changes that could potentially be linked to disrupting allosteric inter-domain communication. The specific site of perturbation we chose corresponds to a highly conserved active-site cysteine and is of particular interest due to its ability to be post-translationally modified *in vivo* (**Figure A.1B**) (Lee et al., 2013). There are numerous accounts of Hsp70 family members acquiring modifications at the active-site cysteine of interest and modulating function; thus, we propose that the molecular basis presented here may be a more general

mechanism that can be extended to analogous systems (Carbone et al., 2004; Chang et al., 2010; Chirico et al., 1998; Hermawan and Chirico, 1999; Miyata et al., 2013; 2012; Wang et al., 2014; Wang and Sevier, 2016; H. Zhang et al., 2016). Hsc70 has been shown to be dose dependently modified by hydrogen peroxide to form sulfinic and sulfonic acids with 10- to 100-fold enrichments (Lee et al., 2013). In contrast to proteomic evidence, it has been reported that Hsc70 cannot be modified by the redox-active compound methylene blue *in vitro* and authors conclude that Hsc70 cannot undergo redox-modifications (Miyata et al., 2012). One explanation for the inability for Hsc70 to be modified by methylene blue *in vitro* is the large overall size of the molecule in comparison to hydrogen peroxide, methylene blue not being an endogenous source of cysteine modification, and majority of post-translational modifications require an enzyme to catalyze the modification addition.

Because the cysteine-to-tryptophan mutation is a valuable proxy for understanding oxidation, we wanted to speculate if cysteine oxidation could elicit a similar perturbation to the active-site. In order to compare perturbations that post-translational modifications may induce, we modeled both sulfonic acid and glutathione into the wild-type structure from this study positionally at $C^{17}$ (**Figure A.6**). Simulated annealing and geometry minimizations provide a hypothetical guide for comparing the relative sizes of $C^{17}$, $C^{17}W$, sulfonic acid and glutathione and the positions they may adopt. Displaying solvent-excluded surfaces of cysteine and tryptophan illustrates the size differences between wild-type and mutant structures from this study, and when compared to sulfonic acid, we detect a similar size and position to that of $C^{17}W$ (**Figure A.6A-A.6C**). It is also evident that sulfonic acid is able to partially occupy the location of

H20‡ found in the wild-type structure (**Figure A.6C**). The glutathione model imparts a more severe perturbation due to the modification being much larger than both $C^{17}W$ and sulfonic acid and occupies a large portion of the active-site (**Figure A.6D**). Though a direct link between cysteine oxidation and allosteric disruption have yet to be determined mechanistically, it is appealing to speculate how the structural basis determined using a cysteine-to-tryptophan mutation as a proxy could inform mechanisms of post-translational modifications.

## MATERIALS AND METHODS

*Protein Expression and Purification.*

Hsc70 NBD (5-381) and near full-length (5-554) were constructed by cloning sequences into pET-28a (EMD Millipore, Billerica, MA). The $C^{17}W$ point mutations were generated using QuikChange mutagenesis (Agilent Technologies, Santa Clara, CA) and verified by sequencing. Proteins were expressed in *E. coli* BL21DE3 at 18ºC and cells were harvested via centrifugation, resuspended, and sonicated in $Ni^{2+}$-NTA A buffer (25 mM Tris pH 8.4, 500 KCl, 20 mM Imidazole). Soluble fractions were isolated by centrifugation at 38,000 x g for 1 hour and the hexahistidine-tagged proteins were enriched on $Ni^{2+}$-NTA matrix and eluted in $Ni^{2+}$-NTA A buffer supplemented with imidazole to a final concentration of 500 mM. Excess imidazole was removed using a HiPrep 26/10 desalting column (GE Healthcare, UK) that was pre-equilibrated with 25 mM Tris pH 7.5, 50 mM KCl, 10 mM EDTA and samples were incubated at 4ºC for 12 hours. Apo protein was enriched on a HiTrap Blue HP column (GE Healthcare, UK) and eluted in a gradient from 50 - 1000 mM KCl. The sample was supplemented with 10% glycerol, concentrated, and subjected to gel filtration on a GE S200 16/60 liquid chromatography column (GE Healthcare, UK) equilibrated with 25 mM HEPES pH 7.5, 300 mM KCl,10% glycerol. Monomer fractions were kept separate and frozen for all biochemical assays while all protein was pooled and concentrated for crystallography.

*ATPase Kinetics.*

Enzchek phosphate detection kit was used as described by manufacturer (Moleular Probes, Eugene, OR) with the exception of using a final reaction that

contained 25 mM HEPES pH 7.5, 150 mM KCl, 2 mM $MgCl_2$, and 5% glycerol. The data were collected from 100 µL reactions in half area 96-well plates (Corning Inc, Corning, NY) using a BioTek Synergy II plate reader with an absorbance 360 nm. ATPase activity was assayed at a range of protein concentrations in a reaction containing 1 mM ATP (Sigma, St. Louis, MO) at 25ºC. Raw data were converted to µM phosphate with a standard curve and the initial 10% of substrate conversion was fit to a linear regression to obtain the rate (µM $P_i$ / min). Rate was plotted as a function of enzyme concentration in units of µM and the slope of the linear regression is defined as the turnover number ($k_{cat}$ = V / [Enzyme]).

*Differential Radial Capillary Action of Ligand Assay.*

Ligand $K_d$ determination was conducted as previously described (Roelofs et al., 2011). In brief, varying concentrations of Hsc70 (0.005 - 10 µM) was incubated with 5 nM $^{32}$P-ATP for 10 minutes and 4 uL were spotted onto nitrocellulose. Ligand diffusion signal was imaged on a phospho-imager and signal intensities were quantitated using ImageJ (Schneider et al., 2012). Data were normalized between 0 and 1 and and were fit to a saturation-binding model ($Y = Y_{max}*X/(K_d + X)$) to calculate the dissociation constant of ATP.

*Hsc70 Crystallization, Structure Determination, and Modification Modeling.*

Hsc70 wild-type and $C^{17}W$ crystals were obtained from the NBD fragment comprising residues 5-381 through sitting drop vapor diffusion. Protein (10-30 mg/ml) was incubated with 5 mM nucleotide and 5 mM $MgCl_2$ for 20 minutes at 25ºC, mixed

with an equal volume of reservoir solution, and incubated at 20ºC where crystals developed within 12 hours in a reservoir solution of 0.2 M sodium chloride, 0.1 M Tris pH 8.5, 25% w/v polyethylene glycol 3,350 (Hampton Research, Aliso Viejo, CA). Crystals were subsequently optimized via hanging drop vapor diffusion yielding crystals suitable for diffraction experiments in 0.2 M sodium chloride, 0.1 M Tris pH 9, 24% w/v polyethylene glycol 3,350 for wild-type Hsc70 and 0.2 M sodium chloride, 0.1 M Tris pH 7.4, 26% w/v polyethylene glycol 3,350 for Hsc70 $C^{17}W$. Upon harvesting, crystals were soaked in the previously mentioned conditions supplemented with 25% glycerol as a cryoprotectant for 5 minutes and frozen in liquid nitrogen.

X-ray diffraction data were collected at the Cornell High Energy Synchrotron Source (CHESS). Data processing and scaling was completed with X-ray Detector Software (XDS) and CCP4 software suite (Kabsch, 2010; Winn et al., 2011). Phases were attained through molecular replacement methods using PHENIX software package and the coordinates of Hsc70 (PDB 4H5R) as a search model (Adams et al., 2010; Z. Zhang et al., 2015). Refinements were conducted in PHENIX and COOT for producing the final model (Adams et al., 2010; Emsley and Cowtan, 2004). Data collection and model statistics are summarized in Table A.1. Figure illustrations, RMSD calculations, and distance measurements were made in Pymol (Version 1.8.4, Schrödinger, LLC). The previously mentioned software packages were accessed through SBGrid (www.sbgrid.org; (Morin et al., 2013)).

Modeling of sulfonic acid and glutathione was achieve by replacing $C^{17}$ in the the wild-type structure from this study with the corresponding modification using COOT,

creating a structure factor model with phenix.fmodel, and conducting simulated annealing and geometry minimizations using PHENIX to attain the final models.

*Thermal Shift Assay.*

A fluorescence-based thermal shift assay using SPYRO Orange (Invitrogen, Carlsad, CA) was used to generate protein melting curves and calculate $T_m$ values (Lo et al., 2004). The reaction contains 2 μM Hsc70, 2 mM nucleotide, 4 mM MgCl2, and 5x SYPRO Orange in 25 mM HEPES pH 7.5, 300 mM KCl, 10% glycerol. A 20 μL reaction was read in a MicroAmp 384 well plate (Applied Biosystems, Foster City, CA) using a ViiA 7 Real-Time PCR System (Applied Biosystems, Foster City, CA). The protocol was initiated with a 5 minute incubation at 10ºC followed by increasing the temperature to 95ºC at the rate of 0.03ºC / sec; excitation and emission wavelengths were 470 ± 15 and 586 ± 10 nm respectively. $T_m$ values are defined by calculating the temperature where the second derivative of the thermal unfolding curve is equal to zero using GraphPad Prism (GraphPad, La Jolla, CA).

*Quantification and Statistical Analysis.*

Data fitting including baseline corrections, normalization, calculation of mean and standard deviation, and statistical tests were conducted using GraphPad Prism (version 6.0h). The number of biological and technical replicates as well as the entity plotted are indicated in the figure legends. Data baseline correction and normalization, where applied, were indicated in the corresponding method section and in the axis labels. No explicit power analysis was used.

## REFERENCES


Adams, P.D., Afonine, P.V., Bunkoczi, G., Chen, V.B., Davis, I.W., Echols, N., Headd, J.J., Hung, L.W., Kapral, G.J., Grosse-Kunstleve, R.W., McCoy, A.J., Moriarty, N.W., Oeffner, R., Read, R.J., Richardson, D.C., Richardson, J.S., Terwilliger, T.C., Zwart, P.H., 2010. PHENIX: a comprehensive Python-based system for macromolecular structure solution. Acta Cryst (2010). D66, 213-221 [doi:10.1107/S0907444909052925] 66, 1–9. doi:10.1107/S0907444909052925

Arakawa, A., Handa, N., Shirouzu, M., Yokoyama, S., 2011. Biochemical and structural studies on the high affinity of Hsp70 for ADP. Protein Sci. 20, 1367–1379. doi:10.1002/pro.663

Bhattacharya, A., Kurochkin, A.V., Yip, G.N.B., Zhang, Y., Bertelsen, E.B., Zuiderweg, E.R.P., 2009. Allostery in Hsp70 Chaperones Is Transduced by Subdomain Rotations. Journal of Molecular Biology 388, 475–490. doi:10.1016/j.jmb.2009.01.062

Buxbaum, E., Woodman, P.G., 1996. Binding of ATP and ATP analogues to the uncoating ATPase Hsc70 (70 kDa heat-shock cognate protein). Biochem. J. 318 ( Pt 3), 923–929.

Carbone, D.L., Doorn, J.A., Kiebler, Z., Sampey, B.P., Petersen, D.R., 2004. Inhibition of Hsp72-Mediated Protein Refolding by 4-Hydroxy-2-nonenal. Chem. Res. Toxicol. 17, 1459–1467. doi:10.1021/tx049838g

Chang, L., Thompson, A.D., Ung, P., Carlson, H.A., Gestwicki, J.E., 2010. Mutagenesis reveals the complex relationships between ATPase rate and the chaperone activities of Escherichia coli heat shock protein 70 (Hsp70/DnaK). Journal of Biological Chemistry 285, 21282–21291. doi:10.1074/jbc.M110.124149

Chirico, W.J., Markey, M.L., Fink, A.L., 1998. Conformational changes of an Hsp70 molecular chaperone induced by nucleotides, polypeptides, and N-ethylmaleimide. Biochemistry 37, 13862–13870. doi:10.1021/bi980597j

Cyr, D.M., Neupert, W., 1996. Roles for hsp70 in protein translocation across membranes of organelles, in: Stress-Inducible Cellular Responses. Birkhäuser Basel, Basel, pp. 25–40. doi:10.1007/978-3-0348-9088-5_3

Daugaard, M., Rohde, M., Jäättelä, M., 2007. The heat shock protein 70 family: Highly homologous proteins with overlapping and distinct functions. FEBS Letters 581, 3702–3710. doi:10.1016/j.febslet.2007.05.039

Emsley, P., Cowtan, K., 2004. Coot: model-building tools for molecular graphics. Acta Crystallogr. D Biol. Crystallogr. 60, 2126–2132. doi:10.1107/S0907444904019158

Flaherty, K.M., DeLuca-Flaherty, C., McKay, D.B., 1990. Three-Dimensional Structure of the ATPase Fragment of a 70K Heat-Shock Cognate Protein - ProQuest. Nature.

Flaherty, K.M., Wilbanks, S.M., DeLuca-Flaherty, C., McKay, D.B., 1994. Structural basis of the 70-kilodalton heat shock cognate protein ATP hydrolytic activity. II. Structure of the active site with ADP or ATP bound to wild type and mutant ATPase fragment. J. Biol. Chem. 269, 12899–12907.

Frydman, J., Nimmesgern, E., Ohtsuka, K., Hartl, F.U., 1994. Folding of nascent polypeptide chains in a high molecular mass assembly with molecular chaperones. Nature 370, 111–117. doi:10.1038/370111a0

Hermawan, A., Chirico, W.J., 1999. N-Ethylmaleimide-modified Hsp70 inhibits protein folding. Arch. Biochem. Biophys. 369, 157–162. doi:10.1006/abbi.1999.1354

Hjerpe, R., Bett, J.S., Keuss, M.J., Solovyova, A., McWilliams, T.G., Johnson, C., Sahu, I., Varghese, J., Wood, N., Wightman, M., Osborne, G., Bates, G.P., Glickman, M.H., Trost, M., Knebel, A., Marchesi, F., Kurz, T., 2016. UBQLN2 Mediates Autophagy-Independent Protein Aggregate Clearance by the Proteasome. Cell 166, 935–949. doi:10.1016/j.cell.2016.07.001

Hughes, S.J., Antoshchenko, T., Chen, Y., Lu, H., Pizarro, J.C., Park, H.-W., 2016. Probing the ATP Site of GRP78 with Nucleotide Triphosphate Analogs. PLoS ONE 11, e0154862–17. doi:10.1371/journal.pone.0154862

Jiang, J., Maes, E.G., Taylor, A.B., Wang, L., Hinck, A.P., Lafer, E.M., Sousa, R., 2007. Structural Basis of J Cochaperone Binding and Regulation of Hsp70. Molecular Cell 28, 422–433. doi:10.1016/j.molcel.2007.08.022

Jiang, J., Prasad, K., Lafer, E.M., Sousa, R., 2005. Structural basis of interdomain communication in the Hsc70 chaperone. Molecular Cell 20, 513–524. doi:10.1016/j.molcel.2005.09.028

Kabsch, W., Mannherz, H.G., Suck, D., Pai, E.F., Holmes, K.C., 1990. Atomic structure of the actin:DNase I complex. Nature 347, 37–44. doi:10.1038/347037a0

Kabsch, W., 2010. XDS. Acta Cryst (2010). D66, 125-132. [doi:10.1107/S0907444909047337] 66, 1–8. doi:10.1107/S0907444909047337

Lee, C.-F., Paull, T.T., Person, M.D., 2013. Proteome-wide Detection and Quantitative Analysis of Irreversible Cysteine Oxidation Using Long Column UPLC-pSRM. J. Proteome Res. 12, 4302–4315. doi:10.1021/pr400201d

Lindquist, S., Craig, E.A., 1988. The heat-shock proteins. Annu. Rev. Genet. 22, 631–677. doi:10.1146/annurev.ge.22.120188.003215

Liu, Y., Gierasch, L.M., Bahar, I., 2010. Role of Hsp70 ATPase Domain Intrinsic Dynamics and Sequence Evolution in Enabling its Functional Interactions with NEFs. PLoS Comp Biol 6, e1000931–15. doi:10.1371/journal.pcbi.1000931

Lo, M.-C., Aulabaugh, A., Jin, G., Cowling, R., Bard, J., Malamas, M., Ellestad, G., 2004. Evaluation of fluorescence-based thermal shift assays for hit identification in drug discovery. Analytical Biochemistry 332, 153–159. doi:10.1016/j.ab.2004.04.031

Macias, A.T., Williamson, D.S., Allen, N., Borgognoni, J., Clay, A., Daniels, Z., Dokurno, P., Drysdale, M.J., Francis, G.L., Graham, C.J., Howes, R., Matassova, N., Murray, J.B., Parsons, R., Shaw, T., Surgenor, A.E., Terry, L., Wang, Y., Wood, M., Massey, A.J., 2011. Adenosine-Derived Inhibitors of 78 kDa Glucose Regulated Protein (Grp78) ATPase: Insights into Isoform Selectivity. Journal of medicinal …. doi:10.1021/jm101625x

Marino, S.M., Gladyshev, V.N., 2010. Cysteine function governs its conservation and degeneration and restricts its utilization on protein surfaces. Journal of Molecular Biology 404, 902–916. doi:10.1016/j.jmb.2010.09.027

Mashaghi, A., Bezrukavnikov, S., Minde, D.P., Wentink, A.S., Kityk, R., Zachmann-Brand, B., Mayer, M.P., Kramer, G., Bukau, B., Tans, S.J., 2016. Alternative modes of client binding enable functional plasticity of Hsp70. Nature Publishing Group 539, 448–451. doi:10.1038/nature20137

Mayer, M.P., 2013. Hsp70 chaperone dynamics and molecular mechanism. Trends in Biochemical Sciences 38, 507–514. doi:10.1016/j.tibs.2013.08.001

Mayer, M.P., Bukau, B., 2005. Hsp70 chaperones: Cellular functions and molecular mechanism. Cell. Mol. Life Sci. 62, 670–684. doi:10.1007/s00018-004-4464-6

Miyata, Y., Li, X., Lee, H.-F., Jinwal, U.K., Srinivasan, S.R., Seguin, S.P., Young, Z.T., Brodsky, J.L., Dickey, C.A., Sun, D., Gestwicki, J.E., 2013. Synthesis and Initial Evaluation of YM-08, a Blood-Brain Barrier Permeable Derivative of the Heat Shock Protein 70 (Hsp70) Inhibitor MKT-077, Which Reduces Tau Levels. ACS Chem. Neurosci. 4, 930–939. doi:10.1021/cn300210g

Miyata, Y., Rauch, J.N., Jinwal, U.K., Thompson, A.D., Srinivasan, S., Dickey, C.A., Gestwicki, J.E., 2012. Cysteine Reactivity Distinguishes Redox Sensing by the Heat-Inducible and Constitutive Forms of Heat Shock Protein 70. Chemistry & Biology 19, 1391–1399. doi:10.1016/j.chembiol.2012.07.026

Morin, A., Eisenbraun, B., Key, J., Sanschagrin, P.C., Timony, M.A., Ottaviano, M., Sliz, P., 2013. Collaboration gets the most out of software. eLife 2, e01456–6. doi: 10.7554/eLife.01456

O'Brien, M.C., Flaherty, K.M., McKay, D.B., 1996. Lysine 71 of the chaperone protein Hsc70 Is essential for ATP hydrolysis. J. Biol. Chem. 271, 15874–15878.

O'Brien, M.C., McKay, D.B., 1995. How potassium affects the activity of the molecular chaperone Hsc70. I. Potassium is required for optimal ATPase activity. J. Biol. Chem. 270, 2247–2250. doi:10.1074/jbc.270.5.2247

Qi, R., Sarbeng, E.B., Liu, Q., Le, K.Q., Xu, X., Xu, H., Yang, J., Wong, J.L., Vorvis, C., Hendrickson, W.A., Zhou, L., Liu, Q., 2013. Allosteric opening of the polypeptide-binding site when an Hsp70 binds ATP. Nature Structural & Molecular Biology 20, 900–907. doi:10.1038/nsmb.2583

Roelofs, K.G., Wang, J., Sintim, H.O., Lee, V.T., 2011. Differential radial capillary action of ligand assay for high-throughput detection of protein-metabolite interactions. Proc. Natl. Acad. Sci. U.S.A. 108, 15528–15533. doi:10.1073/pnas.1018949108

Sadis, S., Hightower, L.E., 1992. Unfolded proteins stimulate molecular chaperone Hsc70 ATPase by accelerating ADP/ATP exchange. Biochemistry 31, 9406–9412.

Schneider, C.A., Rasband, W.S., Eliceiri, K.W., 2012. NIH Image to ImageJ: 25 years of image analysis. Nat Meth 9, 671–675. doi:10.1038/nmeth.2089

Sevier, C.S., Qu, H., Heldman, N., Gross, E., Fass, D., Kaiser, C.A., 2007. Modulation of Cellular Disulfide-Bond Formation and the ER Redox Environment by Feedback Regulation of Ero1. Cell 129, 333–344. doi:10.1016/j.cell.2007.02.039

Sharma, S.K., De Los Rios, P., Christen, P., Lustig, A., Goloubinoff, P., 2010. The kinetic parameters and energy cost of the Hsp70 chaperone as a polypeptide unfoldase. Nat Meth 6, 1–7. doi:10.1038/nchembio.455

Sousa, M.C., McKay, D.B., 1998. The hydroxyl of threonine 13 of the bovine 70-kDa heat shock cognate protein is essential for transducing the ATP-induced conformational change. Biochemistry 37, 15392–15399. doi:10.1021/bi981510x

Sullivan, C.S., Gilbert, S.P., Pipas, J.M., 2001. ATP-Dependent Simian Virus 40 T-Antigen-Hsc70 Complex Formation. Journal of Virology 75, 1601–1610. doi:10.1128/JVI.75.4.1601-1610.2001

Tu, B.P., Weissman, J.S., 2004. Oxidative protein folding in eukaryotes: mechanisms and consequences. The Journal of Cell Biology 164, 341–346. doi:10.1083/jcb.200311055

Ung, P.M.-U., Thompson, A.D., Chang, L., Gestwicki, J.E., Carlson, H.A., 2013. Identification of Key Hinge Residues Important for Nucleotide-Dependent Allostery in E. coli Hsp70/DnaK. PLoS Comp Biol 9, e1003279–11. doi:10.1371/journal.pcbi.1003279

Vogel, M., Bukau, B., Mayer, M.P., 2006a. Allosteric Regulation of Hsp70 Chaperones by a Proline Switch. Molecular Cell 21, 359–367. doi:10.1016/j.molcel.2005.12.017

Vogel, M., Mayer, M.P., Bukau, B., 2006b. Allosteric regulation of Hsp70 chaperones involves a conserved interdomain linker. J. Biol. Chem. 281, 38705–38711. doi: 10.1074/jbc.M609020200

Wang, J., Pareja, K.A., Kaiser, C.A., Sevier, C.S., 2014. Redox signaling via the molecular chaperone BiP protects cells against endoplasmic reticulum-derived oxidative stress. eLife 3, 790–21. doi:10.7554/eLife.03496

Wang, J., Sevier, C.S., 2016. Formation and Reversibility of BiP Protein Cysteine Oxidation Facilitate Cell Survival during and post Oxidative Stress. J. Biol. Chem. 291, 7541–7557. doi:10.1074/jbc.M115.694810

Wei, J., Hendershot, L.M., 1995. Characterization of the nucleotide binding properties and ATPase activity of recombinant hamster BiP purified from bacteria. J. Biol. Chem. 270, 26670–26676.

Wilbanks, S.M., DeLuca-Flaherty, C., McKay, D.B., 1994. Structural basis of the 70-kilodalton heat shock cognate protein ATP hydrolytic activity. I. Kinetic analyses of active site mutants. J. Biol. Chem. 269, 12893–12898.

Wilbanks, S.M., McKay, D.B., 1998. Structural replacement of active site monovalent cations by the epsilon-amino group of lysine in the ATPase fragment of bovine Hsc70. Biochemistry 37, 7456–7462. doi:10.1021/bi973046m

Wilbanks, S.M., McKay, D.B., 1995. How potassium affects the activity of the molecular chaperone Hsc70. II. Potassium binds specifically in the ATPase active site. J. Biol. Chem. 270, 2251–2257.

Winn, M.D., Ballard, C.C., Cowtan, K.D., Dodson, E.J., Emsley, P., Evans, P.R., Keegan, R.M., Krissinel, E.B., Leslie, A.G.W., McCoy, A., McNicholas, S.J., Murshudov, G.N., Pannu, N.S., Potterton, E.A., Powell, H.R., Read, R.J., Vagin, A., Wilson, K.S., 2011. Overview of the CCP4 suite and current developments. Acta Crystallogr. D Biol. Crystallogr. 67, 235–242. doi:10.1107/S0907444910045749

Winter, J., Linke, K., Jatzek, A., Jakob, U., 2005. Severe Oxidative Stress Causes Inactivation of DnaK and Activation of the Redox-Regulated Chaperone Hsp33. Molecular Cell 17, 381–392. doi:10.1016/j.molcel.2004.12.027

Wisniewska, M., Karlberg, T., Lehtiö, L., Johansson, I., Kotenyova, T., Moche, M., Schüler, H., 2010. Crystal Structures of the ATPase Domains of Four Human Hsp70 Isoforms: HSPA1L/Hsp70-hom, HSPA2/Hsp70-2, HSPA6/Hsp70B', and HSPA5/BiP/GRP78. PLoS ONE 5, e8625. doi:10.1371/journal.pone.0008625

Xu, M., Marsh, H.M., Sevier, C.S., 2016. A Conserved Cysteine within the ATPase Domain of the Endoplasmic Reticulum Chaperone BiP is Necessary for a Complete Complement of BiP Activities. Journal of Molecular Biology 428, 4168–4184. doi:10.1016/j.jmb.2016.08.011

Yan, M., Li, J., Sha, B., 2011. Structural analysis of the Sil1-Bip complex reveals the mechanism for Sil1 to function as a nucleotide-exchange factor. Biochem. J. 438, 447–455. doi:10.1042/BJ20110500

Young, J.C., 2010. Mechanisms of the Hsp70 chaperone system. Biochem. Cell Biol. 88, 291–300. doi:10.1139/o09-175

Zhang, H., Yang, J., Wu, S., Gong, W., Chen, C., Perrett, S., 2016. Glutathionylation of the Bacterial Hsp70 Chaperone DnaK Provides a Link between Oxidative Stress and the Heat Shock Response. Journal of Biological Chemistry 291, 6967–6981. doi:10.1074/jbc.M115.673608

Zhang, Z., Cellitti, J., Teriete, P., Pellecchia, M., Stec, B., 2015. New crystal structures of HSC-70 ATP binding domain confirm the role of individual binding pockets and suggest a new method of inhibition. Biochimie 108, 186–192. doi:10.1016/j.biochi.2014.11.012